Uncertainty in predictions of large-scale sandy interventions

Kroon, J.

DOI
10.4233/uuid:6b572d9e-481a-4be6-815b-dc42647e6feb

Publication date
2024

Document Version
Final published version

Citation (APA)
Kroon, J. (2024). *Uncertainty in predictions of large-scale sandy interventions*. [Dissertation (TU Delft), Delft University of Technology]. https://doi.org/10.4233/uuid:6b572d9e-481a-4be6-815b-dc42647e6feb

Important note
To cite this publication, please use the final published version (if applicable).
Please check the document version above.

UNCERTAINTY IN PREDICTIONS OF LARGE-SCALE SANDY INTERVENTIONS

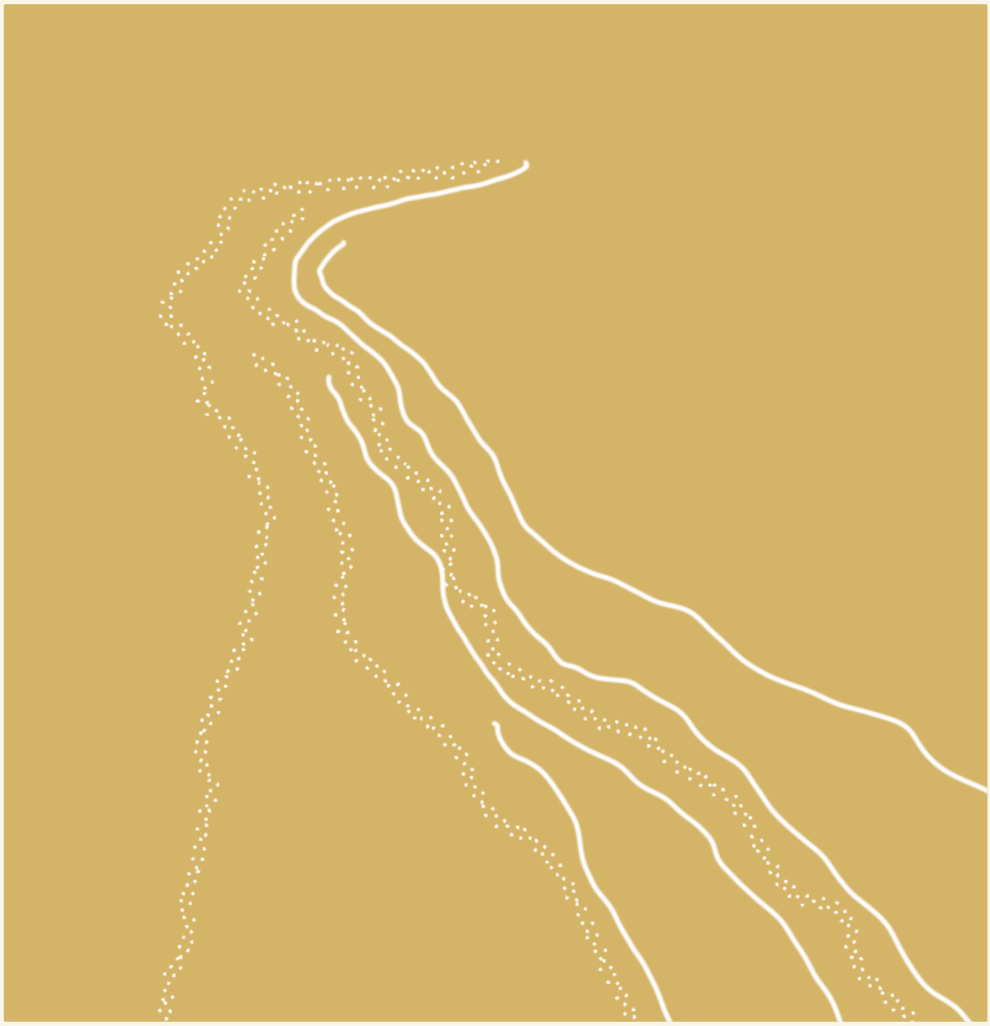

JOANNA KROON

Hondsbossche Duinen, view from the south. Photo credits: Jan Willem Keizer, Hoogheemraadschap Hollands Noorderkwartier

Uncertainty in predictions of large-scale sandy interventions

Proefschrift

ter verkrijging van de graad van doctor
aan de Technische Universiteit Delft,
op gezag van de Rector Magnificus Prof. dr. ir. T.H.J.J. van der Hagen,
voorzitter van het College voor Promoties,
in het openbaar te verdedigen op
maandag 17 juni 2024 om 10:00 uur

door

Joanna KROON

Civiel ingenieur,
Technische Universiteit Delft, Nederland.
Geboren te Utrecht, Nederland.

Dit proefschrift is goedgekeurd door de promotoren.

Samenstelling promotiecommissie bestaat uit:

Rector Magnificus,	voorzitter
Dr. ir. M.A. de Schipper	Technische Universiteit Delft, promotor
Prof. dr. ir. S.G.J. Aarninkhof	Technische Universiteit Delft, promotor
Prof. dr. ir. P.H.A.J.M. van Gelder	Technische Universiteit Delft, promotor

Onafhankelijke leden:

Prof. dr. ir. S.N. Jonkman	Technische Universiteit Delft
Prof. dr. B.G. Ruessink	Universiteit Utrecht
Prof. dr. K.M. Wijnberg	Universiteit Twente
Dr. K.D. Splinter	University of New South Wales, Australië
Prof. dr. ir. A.J.H.M. Reniers,	Technische Universiteit Delft, reservelid

This research is part of the PRO-COAST project of TKI Deltatechnology, with partners Rijkswaterstaat, Hoogheemraadschap Hollands Noorderkwartier, Van Oord Nederland B.V., Boskalis Nederland B.V., and Svašek Hydraulics.

Keywords: Coastal modeling, uncertainty, large-scale sandy interventions, Hondsbossche Dunes, Coastal state indicators

Printed by: www.ridderprint.nl

Front & Back: Cover design by Zaza Zuilhof.

ISBN 978-94-6366-877-4

An electronic version of this dissertation is available at http://repository.tudelft.nl/.

Contents

Summary

Because of the large uncertainties associated with rising sea levels, present coastal management is inclined towards utilizing soft, nature-inclusive, and adaptive measures over traditional hard protection structures. This shift towards more sustainable and multi-functional solutions is often called Building with Nature. In the coastal zone, these nature-based solutions typically use sand as a building material, have a larger scale than traditional sand nourishments, and serve multiple purposes. The definition of effectiveness of these nature-based solutions can vary for the different project aims. This means that models that predict future states of these interventions must be able to forecast various coastal state indicators (CSIs), such as dune volume, beach width, or habitat area. Using loose-placed sand in coastal protection is intrinsically associated with increased uncertainties of the coastal state compared to more traditional hard protection measures. Therefore, this dissertation examines uncertainty in predicting large-scale sandy interventions in the coastal zone and its effect on different CSIs.

First, observations of a recent large-scale intervention, the Hondsbosse Dunes, were analyzed to illustrate the evolution of various CSIs in the first years after placement. This 35 million m^3 nourishment included a shoreface, beach, and dune and was built in front of a sea dike to serve as flood protection while creating space for nature and recreation. The nourishment created a significant coastline curvature, leading to erosion in the central, most protruding part of the nourishment, bordered by zones with accretion. The artificial cross-shore profile rapidly mimics the surf zone slope and beach width of adjacent beaches. At the same time, the dune volume increased, and the dune foot migrated seaward along the entire nourished site, regardless of whether the subaqueous profile gained or lost sediment. These contrasting trends of different CSIs highlight the need to predict changes in CSIs individually to assess a project's effectiveness

Next, the balance between different sources of uncertainty in predicting the evolution of a large-scale sandy intervention was investigated for the Sand Engine mega-nourishment. The sources of uncertainty in such predictions can be either intrinsic or epistemic. Intrinsic sources are inherent in the system, whereas epistemic sources are related to limitations in knowledge (related to the model). The relative importance of intrinsic and epistemic uncertainty was investigated using a probabilistic framework in which sediment transport is considered a function of random wave forcing (intrinsic) and model (epistemic) uncertainty, calculating transport using a one-line model. The applied wave climate variability was obtained from long-term wave observations, whereas model uncertainty was quantified using Generalized Likelihood Uncertainty Estimation (GLUE) relying on monthly observations. A global sensitivity analysis showed that the con-

fidence intervals on predicted volume losses increase by at least 50% when both intrinsic and epistemic sources of uncertainty are included. This is even more in case of correlated sources of uncertainty, producing significant overconfidence in the results when neglecting epistemic uncertainty. These findings imply that model settings may be the principal source of uncertainty when forecasting large-scale sandy interventions with simplified models on a multi-year time scale.

Finally, to investigate how model parameter uncertainty develops over time and space when predicting various CSIs, the multi-dimensional parameter space of a state-of-the-art Delft3D coastal area model was explored. The over 50 model-free parameters were reduced to five key parameters using expert judgment and the Elementary-Effect method. An observation-based likelihood distribution of the model parameters and the CSIs using GLUE was derived. Uncertainty in these five input parameters leads to significant uncertainty in predicted CSI values. The parameter uncertainty creates the widest confidence intervals for the CSIs at locations and moments when the changes are most significant. Overall, this uncertainty is mainly caused by contributions of the suspended sediment transport scaling (f_{sus}), the breaker index (γ), and the grain size (d_{50}), but the importance of the five parameters varies per CSI. The model's sensitivity can vary significantly depending on the CSI used for calibration. As a result, the parameter values that yielded the best results may not be transportable, and there may be no single generic value for each parameter. Our results underline the importance of good model calibration. Herein, the calibration area and parameter(s) of choice should be consistent with the CSIs to predict, as they can significantly impact the outcome of the (manual) calibration procedure.

This study analyzes uncertainties in predicting large-scale sandy interventions in the coastal zone. The results imply that uncertainty analysis cannot be limited to the consequences of intrinsic factors only, because (epistemic) model uncertainty significantly contributes to uncertainties on relevant time scales (1-10 years). These interventions will probably show significant longshore and cross-shore equilibration after placement, with the subaqueous cross-shore equilibration occurring relatively quickly compared to the alongshore deformation. The difference in timescale suggests that evaluation of volume changes with a one-line model approach that focuses on the alongshore changes is possible. Still, it lacks the detail required to address the evolution of more complex CSIs (e.g., habitat area or dune volume). When used in the probabilistic framework, the one-line approach can lead to results similar to those of the much more complex coastal area analysis. The skill of an individual computation with a one-line model is lower, but the low computational effort allows for more computations. Depending on the CSI(s) of interest, using a one-line model can thus lead to a higher amount of information. Therefore, the model type needed for a probabilistic analysis will depend mainly on the design of the large-scale sandy intervention and how its success is defined (e.g., guaranteed beach width or volume). These findings help effective assessment of uncertainties in the predictions of large-scale sandy interventions, especially for the design of coastal adaptation under uncertain sea level rise.

Samenvatting

Vanwege de grote onzekerheid die gepaard gaat met zeespiegelstijging, geeft het huidige kustbeheer de voorkeur aan zachte, natuur-inclusieve, en adaptieve maatregelen boven traditionele harde beschermingsmaatregelen. Deze verschuiving naar duurzamere en multifunctionele oplossingen wordt vaak *Building with Nature* genoemd. Deze op natuur gebaseerde oplossingen in de kustzone maken doorgaans gebruik van zand als bouwmateriaal, hebben een grotere ruimtelijke schaal dan traditionele zandsuppleties, en dienen meerdere doelen. De definitie van effectiviteit van deze projecten kan variëren met het doel. Dit betekent dat modellen die de toekomstige staat van deze interventies voorspellen, verschillende kustindicatoren (KI's) zoals duinvolume, strandbreedte of de omvang van een habitat moeten kunnen voorspellen. Het gebruik van los geplaatst zand als bouwmateriaal is intrinsiek verbonden met verhoogde onzekerheid met betrekking tot de toestand van de kust in vergelijking met meer traditionele harde beschermingsmaatregelen. Daarom onderzoekt dit proefschrift onzekerheid in voorspellingen van grootschalige zandige interventies in de kustzone en het effect ervan op verschillende KI's.

Allereerst zijn observaties van een grootschalige zandige interventie, de Hondsbossche Duinen, geanalyseerd als voorbeeld van hoe verschillende KI's zich ontwikkelen in de eerste jaren na aanleg. Deze suppletie van 35 miljoen m^3 is een gecombineerde voeroever-, strand- en duinsuppletie. De suppletie is zeewaarts van een oude zeedijk aangebracht om de hoogwaterveiligheidsfunctie over te nemen en gelijktijdig ruimte te creëren voor natuur en recreatie. De suppletie creëerde een significante kustlijnkromming, met erosie in de centrale meest zeewaarts gelegen deel en aanliggende zones met sedimentatie. Het kunstmatige dwarsprofiel vertoonde al snel een vergelijkbare helling van de brandingszone en strandbreedte als de aangrenzende kust. In dezelfde periode nam het duinvolume toe en verplaatste de duinvoet zeewaarts over het gehele project gebied, ongeacht of het sedimentvolume van onderwaterprofiel toe- of afnam. Dit contrast in gedrag van verschillende KI's benadrukt de noodzaak om veranderingen per KI te voorspellen om de effectiviteit van een project te kunnen beoordelen.

Vervolgens is de balans tussen verschillende bronnen van onzekerheid bij het voorspellen van de ontwikkeling van een grootschalige zandige interventie onderzocht voor de Zandmotor mega-suppletie. De bronnen van onzekerheid in dergelijke voorspellingen kunnen intrinsiek of epistemisch zijn. Intrinsieke bronnen zijn inherent aan het systeem, terwijl epistemische bronnen verband houden met beperkingen in kennis (gerelateerd aan het model). Het relatieve belang van intrinsieke en epistemische onzekerheid is onderzocht met behulp van een probabilistisch kader waarin sedimenttransport wordt beschouwd als een

functie van willekeurige golfforcering (intrinsiek) en model (epistemisch) onzekerheid, waarbij kustlangstransport wordt berekend met behulp van een één-lijnsmodel. De toegepaste golfklimaatvariabiliteit is verkregen uit langetermijn golfwaarnemingen, terwijl modelonzekerheid werd gekwantificeerd met behulp van *Generalized Likelihood Uncertainty Estimation* (GLUE) op basis van maandelijkse waarnemingen. De betrouwbaarheidsintervallen op voorspelde volumeverliezen nemen aanzienlijk toe wanneer zowel intrinsieke als epistemische bronnen van onzekerheid worden meegenomen. Een globale gevoeligheidsanalyse toont aan dat de variantie met minstens 50% wordt vergroot als zowel intrinsieke en epistemische onzekerheid wordt meegenomen. Die variantie wordt zelfs nog groter als verschillende bronnen van onzekerheid gecorreleerd zijn, wat resulteert in aanzienlijke overschatting van het vertrouwen in de resultaten als er geen epistemische onzekerheid wordt ingeschat. Deze bevindingen impliceren dat modelinstellingen de belangrijkste bron van onzekerheid zijn bij het voorspellen van grootschalige zandige ingrepen met vereenvoudigde modellen op een tijdschaal van jaren.

Tot slot, om te onderzoeken hoe modelparameteronzekerheid zich ontwikkelt in de tijd en ruimte bij het voorspellen van verschillende kustindicatoren, is de meerdimensionale parameterruimte van een state-of-the-art Delft3D kustgebiedsmodel verkend voor voorspellingen. De meer dan 50 modelvrije parameters zijn teruggebracht tot vijf kernparameters met behulp van expert inschatting en de Elementary-Effect-methode. Een op observaties gebaseerde kansverdeling van de modelparameters en de KI's is afgeleid met behulp van GLUE. Onzekerheid in deze vijf invoerparameters leidt tot aanzienlijke onzekerheid in voorspelde KI-waarden. De parameteronzekerheid creëert de breedste betrouwbaarheidsintervallen voor de KI's op locaties en momenten waar de veranderingen het meest significant zijn. Over het algemeen wordt deze onzekerheid voornamelijk veroorzaakt door bijdragen van de schaling van gesuspendeerd sedimenttransport (f_{sus}), de brekerindex (γ) en de korrelgrootte (d_{50}), maar de belangrijkheid van de vijf parameters varieert per KI. De gevoeligheid van het model kan aanzienlijk variëren, afhankelijk van de KI gebruikt voor kalibratie. Als gevolg hiervan zijn de parameterwaarden die de beste resultaten opleverden mogelijk niet overdraagbaar, en bestaat er geen generieke beste waarde voor iedere parameter. Onze resultaten benadrukken het belang van goede modelkalibratie. Hierbij moet het kalibratiegebied en de te kiezen parameter(s) consistent zijn met de te voorspellen KI's, aangezien deze factoren aanzienlijke invloed kunnen hebben op de uitkomst van de (handmatige) kalibratieprocedure.

Dit proefschrift analyseert onzekerheid bij het voorspellen van grootschalige zandige interventies in de kustzone. De resultaten laten zien dat onzekerheidsanalyse niet beperkt kan worden tot de gevolgen van intrinsieke factoren alleen, omdat (epistemische) modelonzekerheid aanzienlijk bijdraagt aan onzekerheden op relevante tijdschalen (1-10 jaar). Deze interventies zullen waarschijnlijk aanzienlijke langs- en dwars-equilibratie laten zien na plaatsing, waarbij de subaquatische dwars-equilibratie relatief snel optreedt in vergelijking met de langsvervorming. Als gevolg daarvan is evaluatie van volumeverandering met een éé-

nlijnsmodel gefocust op langstransport mogelijk. Het ontbreekt daarbij wel aan het detail dat nodig is om de evolutie van meer complexe KI's (bijv. habitatoppervlak of duinvolume) te voorspellen. Het éénlijnsmodel kan gebruikt binnen het probabilistische kader tot vergelijkbare resultaten leiden als de veel complexere 2D kustgebiedsbenadering. De kwaliteit van een individuele éénlijnsberekening is lager maar de lage rekeninspanning staat een veel groter aantal berekeningen toe. Mogelijk kan daardoor met een éénlijnsmodel een grotere hoeveelheid informatie worden verkregen, afhankelijk van de KI('s) van belang. Daarom zal het type model dat nodig is voor een probabilistische analyse voornamelijk afhangen van het ontwerp van de grootschalige zandige interventie en hoe het succes ervan wordt gedefinieerd (bijv. een minimale strandbreedte of volume). Deze bevindingen helpen bij een effectieve beoordeling van onzekerheden in de voorspellingen van grootschalige zandige interventies, met name voor kustaanpassing onder een onzekere zeespiegelstijging.

1

Introduction

1.1. Sandy coastal systems under pressure

The coastal zone is of great ecological, economic, and social importance (Martínez *et al.*, 2007). More than a third of the world's population lives less than 100 km from the coast, more than a tenth lives less than 10 m above sea level, and these numbers are expected to increase (Reimann *et al.*, 2023). In addition to human habitation, the coast provides important ecosystems such as mangroves, coral reefs, and beaches (Cooley *et al.*, 2022). Of the latter, 31% are estimated to consist of sand (Luijendijk *et al.*, 2018).

Sea level rise will continue to accelerate, posing a threat to people, ecosystems, and infrastructure in low-lying areas (Oppenheimer *et al.*, 2019). At sandy beaches, rising sea levels can lead to erosion and consequent loss of ecosystems, recreational area, and reduced safety against flooding. Adaptation to these adverse changes will require an increasing capacity (Hinkel *et al.*, 2018; Nicholls & Cazenave, 2010).

Because of the significant uncertainties associated with sea level rise, adaptation favors flexible responses (i.e., those that can be adapted over time) and periodically adjustable decisions (Oppenheimer *et al.*, 2019). As a result, present coastal management views often favor more soft, nature-inclusive, and adaptive measures over traditional hard protection structures. This shift towards more sustainable and multi-functional solutions is often referred to as Building with Nature, Engineering with Nature, or Living Shorelines (Bridges *et al.*, 2018; de Vriend *et al.*, 2015; Sutton-Grier *et al.*, 2015).

Following these new management views, in many examples, sandy interventions have been preferred over hard structures in the past decade. For instance, the Hondsbossche Dunes project is a combined shoreface, beach, and dune nourishment of 35 million m^3 sand. The nourishment was built to replace the flood protection function of an old sea-dike while creating additional space for nature and recreation (Fig. 1.1a). In Lekki, Nigeria, a sandbar breakwater (van der Spek *et al.*, 2020) instead of a traditional rubble mound breakwater was constructed to protect a port expansion (Fig. 1.1b). At the Prins Hendrik Sand dike

(Perk *et al.*, 2019), a dune and a peninsula were constructed to take over the safety function of the dike while increasing the intertidal habitat (Fig. 1.1c), instead of reinforcing the existing dike. Approximately half of the perimeter of Maasvlakte 2 (Fig. 1.1d), the most recent port expansion of the port of Rotterdam (The Netherlands), is protected by a sandy sea defense instead of a rock and stone sea defense (Kroon *et al.*, 2016). The Sandscaping coastal management scheme between Bacton and Walcott (Cotton *et al.*, 2022), U.K., placed 1.8 million m^3 of sediment on the beach to increase coastal safety while providing recreational space (Fig. 1.1e). The Sand Engine intends to feed the adjacent coastline over 20 years. The shape of the peninsula was inspired by the potential for natural and recreational development (Stive *et al.*, 2013) and a sheltered tidal lagoon was included to create a new habitat (Fig. 1.1f). In general, these nature-based solutions in the coastal zone use sand as a building material and have a much larger scale than regular beach nourishments (de Schipper *et al.*, 2021). Therefore, such projects will be referred to as large-scale sandy interventions from this point forward.

Table 1.1.: Examples of large-scale sandy interventions in the coastal zone and their purpose and scale. Image courtesies from top to bottom of Aannemerscombinatie Zwakke Schakel–Van Oord-Boskalis, CDR International B.V., Hoogheemraadschap Hollands Noorderkwartier, Haven Bedrijf Rotterdam, Google Earth and, http://www.dezandmotor.nl.

Name	Location	Image	Purpose	Scale
a) Hondsbossche Dunes	North-Holland, the Netherlands		Safety, Recreation, Nature	0,5x9km 35 Mm^3
b) Lekki breakwater	Lekki, Nigeria		Economy, Nature	0,1x3km
c) Prins Hendrik zanddijk	Texel, the Netherlands		Safety, Nature	0,5x3km
d) Maasvlakte 2	Rotterdam, the Netherlands		Economy, Recreation	1,5x5km
e) Sand scaping	Bacton, United Kingdom		Safety, recreation	0,2x1,5km 1.8 Mm^3
f) Sand Engine	Ter Heijde, the Netherlands		Safety, recreation, nature	1,5x4km 21 Mm^3

Large-scale sandy interventions may serve multiple purposes (Fig. 1.1), includ-

ing increasing safety against flooding, ecology, commercial activities, and recreation (e.g., Bridges *et al.*, 2018; Palinkas *et al.*, 2022; Stive *et al.*, 2013). These different purposes place different and occasionally conflicting demands on a project's initial and future state (de Schipper *et al.*, 2021). As a result, the definition of effectiveness can vary depending on the project's objective(s) (G. Liu *et al.*, 2019). Coastal state indicators (CSIs) are "A reduced set of issue-related parameters that can simply, adequately and quantitatively describe the dynamic-state and evolutionary trends of a coastal system" (Davidson *et al.*, 2007; van Koningsveld *et al.*, 2005). CSIs can help reduce the complexity of the coastal system to facilitate 1) quantification of coastal trends, 2) benchmarking of desired states, 3) intervention in case of undesired states, and 4) evaluation and communication of the projects' success (van Koningsveld, 2003).

Predictive models that describe the current and future states of these interventions must be able to forecast a variety of indicators that are governed by a range of processes. For example, metrics based on the volume of sand may be used to assess safety against flooding. Similarly, ecology may require a specific habitat area (e.g., dune area) and recreation a minimum beach width (Sánchez-Arcilla *et al.*, 2011). In many cases, changes in volume are influenced by wave-driven alongshore transport, while aeolian transport and storm erosion primarily affect the dune area. All three of these processes are likely to have an impact on beach width. As such, the design of an intervention, the definition of success, and the corresponding CSIs (e.g., dune area, volume, beach width) may pose varying requirements on the model used to predict the evolution of a large-scale sandy intervention.

1.2. Predictions of large-scale sandy interventions

1.2.1. State of the art coastal modeling

In the last decades, significant advances have been made to model and predict the morphological processes governing the changes of the coastal zone (e.g., Ashton & Murray, 2006; Hanson, 1988; Lesser, 2009; Warner *et al.*, 2010). There are less complex models, schematized to one dimension and focused on a single process, such as coastline models, that model coastline change due to gradients in wave-driven alongshore transport (e.g., Dabees & Kamphuis, 1999; Hanson, 1988; Hurst *et al.*, 2015; Pelnard-Considère, 1957). There are more complex coastline models that involve various processes, including alongshore transport, cross-shore transport, and sea level rise (e.g., Roelvink *et al.*, 2020; Vitousek *et al.*, 2017).

Coastal area models are state-of-the-art in the modeling of large-scale sandy interventions. These models resolve morphological processes such as wave- and (tidal) current-driven sediment transport in two horizontal dimensions (e.g., Lesser, 2009). Most recent developments enable predictions of a combination of processes that govern morphological changes on different time-scales, such as aeolian and wave-driven alongshore transport. To this end, several coastal area models are coupled to describe the various processes at their individual time-scales (van

Westen *et al.*, 2024).

Ongoing model developments have significantly contributed to the accuracy and skill of morphodynamic predictions. However, as focus has been on improvements and strengths of the model, less detail is presented on the residual uncertainty after model calibration and validation.

1.2.2. Uncertainties

Using loose-placed sand in coastal protection is intrinsically associated with increased uncertainties of the coastal state compared to more traditional hard protection measures. In addition to this uncertain future state of an intervention, many model related uncertainties are introduced in predicting the future state. In general, the sources of uncertainty in such predictions can be either intrinsic or epistemic. Intrinsic sources are inherent in the system, whereas epistemic sources are related to limitations in knowledge (related to the model) (W. E. Walker *et al.*, 2003). The first is related to the random occurrence of processes in time and space and is irreducible. The second relates to the present state of our process knowledge, models, and methods and is reducible in theory, given appropriate resources. In Fig. 1.1 the types of uncertainty in the context of predictions of large-scale sandy interventions are summarized, adapted from the schematic subdivision of types of uncertainty in the design of civil structures by van Gelder (2000).

Intrinsic uncertainty can manifest in space and time in morphological response on a yearly to decadal time-scale. For instance, the spatial variability in the cross-shore bed levels can significantly influence the alongshore transport (Mil-Homens, 2016), resulting in variations in the morphological response. Likewise, coastal morphology is sensitive to temporal variability, such as the chronology and year-to-year variability in wave forcing (Southgate, 1995). As a result, the exact future state of the coast is difficult to predict beforehand.

Epistemic uncertainty arises from the uncertainties that exist in both observations and models. Model uncertainty can be attributed to model inadequacy, parameter uncertainty (e.g., Ruessink, 2005; Simmons *et al.*, 2017), and numerical limitations (e.g., de Vriend, 1987). Model inadequacy can be caused by missing processes (e.g., beach recovery, long waves, sediment sorting; Huisman *et al.*, 2016) or reduced complexity of processes, such as 1D or 2D models and sediment transport formulae. Ruessink and Kuriyama (2008) show that unpredictability of cross-shore sandbar migration during major wave events originates largely from model inadequacy. Parameter uncertainties arise from limited knowledge of actual values of model parameters (e.g., grain size, bed roughness, or wind shear). These parameters often lack a physical basis, making it difficult to estimate their values (Ruessink, 2005). Parameters representing physical quantities (e.g., grain size, bed friction) are often site-specific, space and time-varying, and therefore challenging to measure, resulting in uncertain estimations of representative values. The spatiotemporal model resolution, the order of the numerical schematization, and the acceleration technique (Luijendijk *et al.*, 2019)

can introduce numerical uncertainties. Finally, observation uncertainty results from the instruments' accuracy and data processing. For instance, sampling limitations and measurement errors can significantly contaminate variability at resolved scales and may lead to errors in representing the scales of interest (Kasprak *et al.*, 2019; Plant *et al.*, 2002).

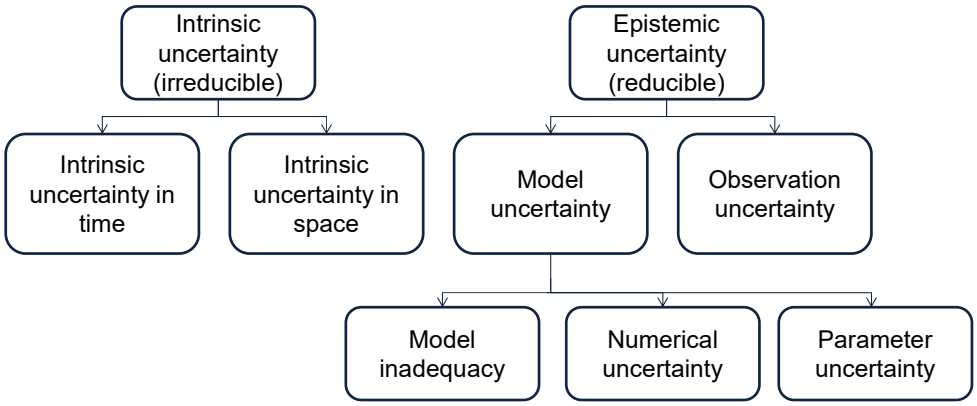

Figure 1.1.: Types of uncertainty in predictions of large-scale sandy interventions. Adapted from: van Gelder (2000)

Uncertainties thus reflect the models' imperfections and unknowns. As a result, more than one outcome can be consistent with expectations (Dessai *et al.*, 2009). However large predicted uncertainties might be, they still provide unique information to help inform risk management (Mankin *et al.*, 2020). Although both these statements are true, coastal uncertainty analysis mostly involves climate change response or natural variations in boundary conditions (e.g., Baart, 2013; Baquerizo & Losada, 2008; Callaghan *et al.*, 2013; D'Anna *et al.*, 2021; Le Cozannet *et al.*, 2019; Ranasinghe *et al.*, 2012; Ruggiero *et al.*, 2010) or rely upon assumed (uncorrelated) normal distributions of input parameters (e.g., Vrijling & Meijer, 1992). Explicit quantification of model (parameter) uncertainty (epistemic uncertainty) in morphological computations is possible (e.g., Kroon *et al.*, 2019; Ruessink, 2005; Simmons *et al.*, 2017). However, such approaches have not yet been applied to examine the uncertainty in predictions of various coastal state indicators after large-scale sandy interventions.

1.3. Research objectives

This dissertation examines uncertainty in predictions of large-scale sandy interventions in the coastal zone and its manifestation in different coastal state indicators. Therefore, we apply and validate a stochastic method for evaluating large-scale sandy interventions. We do this by looking at two large Dutch interventions: the Sand Engine and the Hondsbossche Dunes mega-nourishments.

Several research questions are identified to achieve this objective. The first question aims to identify the requirements of the model used in the stochastic approach:

RQ1: How do various coastal state indicators evolve in the first years after the implementation of a large-scale sandy intervention?

To answer RQ1, the observed evolution of a large-scale sandy intervention is studied (i.e., the Hondsbossche Dunes nourishment). The next question aims to direct the scope of the research by identifying the important uncertainties:

RQ2: What is the relative importance of epistemic uncertainty versus intrinsic uncertainty?

This is done using a one-line model in a Monte Carlo approach, in which sediment transport and volume change are considered to be functions of both intrinsic and epistemic uncertainty. The distribution of the model calibration settings (epistemic uncertainty) is quantified using observations of the Sand Engine nourishment.

Next, the last research question aims to address the effect of uncertainty on different coastal state indicators:

RQ3: How is the uncertainty in predicting coastal state indicators developing over time and space?

To answer RQ3, the model parameter uncertainty for the Sand Engine nourishment is quantified using the same observation-based method as used for RQ2. However, instead of a one-line model, a coastal area model is used to predict various coastal state indicators of the Sand Engine. , Together the findings related to these three uestions, illustrate the evolution of CSIs after large-scale sandy interventions, the associated sources of uncertainty, and the impact of these uncertainties on CSI pr, helping to effectively assessssment of uncertainties in the predictions of large-scale sandy interventions in the coastal zone.

1.4. Research outline

Each of the research questions is answered in a separate chapter. First, Chapter 2 answers RQ1 using observations of a large -scale sandy intervention. Next, Chapter 3 and 4 focus on uncertainties in predictions of the future state of large-scale sandy interventions. Chapter 3 answers RQ2 and looks at uncertainties from a broader perspective as outlined in Fig. 1.1. Afterward, in Chapter 4 RQ3 is answered while zooming in on parameter uncertainty specifically. Finally, Chapter 5 brings the overarching lesson of Chapters 2 to 4 together before conclusions are summarized in Chapter 6. The content of the chapters of this thesis and their interdependence are visualized in Fig. 1.2.

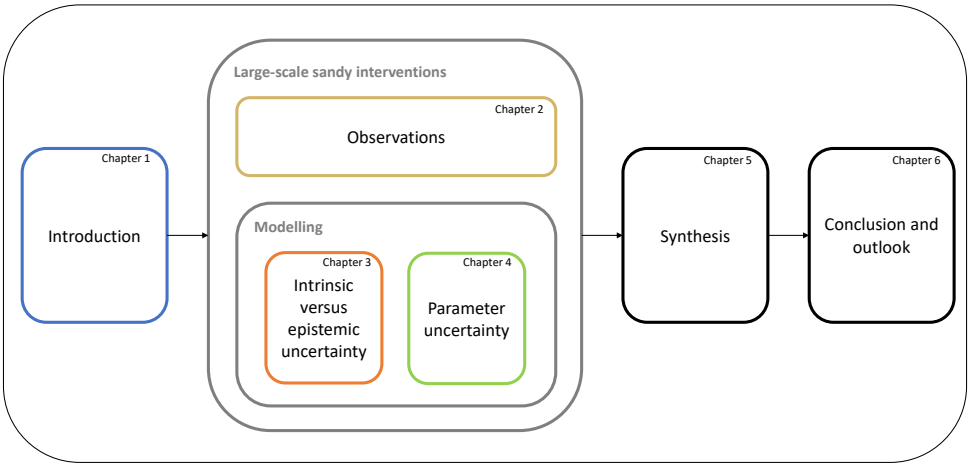

Figure 1.2.: Visualization of the outline of this thesis.

1

Hondbossche Dunes in April 2024. Photo credits: Jan Willem Keizer, Hoogheemraadschap Hollands Noorderkwartier

2

Evolution of Coastal State Indicators after Implementation of a Large-Scale Nourishment

Abstract

Sandy nourishments can provide additional sediment to the coastal system to maintain its recreational or safety function under rising sea levels. These nourishments can be implemented at sandy beach systems, but can also be used to reinforce gray coastal infrastructure (e.g., dams, dikes, seawalls). The Hondsbossche Dunes project is a combined shoreface, beach, and dune nourishment of 35 million m^3 sand. The nourishment was built to replace the flood protection function of an old sea-dike while creating additional space for nature and recreation. This chapter presents the evolution of this newly created sandy beach system in the first 5 years after implementation based on bathymetric and topographic surveys, acquired every three to six months.

A significant coastline curvature is created by the nourishment leading to erosion in the central 7 km bordered by zones with accretion. However, over the five-year period, net volume losses from the project area were less than 5% of the initial nourished sand volume. The artificial cross-shore beach profile rapidly mimics the characteristics of adjacent beaches. The slope of the surfzone is adjusted within two winters to a similar slope. The initially wide beaches (i.e., up to 225 m) are reduced to about 100 m-wide. Simultaneously, the dune volume has increased and the dune foot migrated seaward at the entire nourished site,

This chapter has been published as: **Kroon, A.**, de Schipper, M.A., de Vries, S. and Aarninkhof, S.G.J., (2022) *Subaqueous and Subaerial Beach Changes after Implementation of a Mega Nourishment in Front of a Sea Dike*, Journal of Marine Science and Engineering **10**, 8 (1152).

regardless of whether the subaqueous profile gained or lost sediment. Our results show that the Hondsbossche Dunes nourishment, built with a natural slope and wide beach, created a positive sediment balance in the dune for a prolonged period after placement. As such, natural forces in the years after implementation provided a significant contribution to the growth in dune volume and related safety against flooding.

2.1. Introduction

Acceleration of sea level rise will require an increasing capacity to adapt to adverse changes (e.g., Hinkel *et al.*, 2018; Nicholls & Cazenave, 2010) due to coastal erosion or reduced safety against flooding. At eroding coastlines, sandy (beach) nourishments have been used to mitigate the loss of sediment (Dean, 2002; de Schipper *et al.*, 2021) to preserve recreational or safety functions. Nourishments can be implemented at beach systems, but can also be used to adapt gray coastal infrastructure (e.g., dams, dikes, seawalls) to new coastal management views (e.g., Perk *et al.*, 2019; Ton *et al.*, 2023; Vuik *et al.*, 2016). Coastal management views in which soft, nature-inclusive, and adaptive measures are preferred over more traditional hard protection measures (Bridges *et al.*, 2018; de Vriend *et al.*, 2015), often referred to as Building with Nature, Engineering with Nature, or Living Shorelines.

In the Netherlands, nourishments are a key part of the coastal zone management. Nourishment strategy has become more large-scale and proactive in the last decades, including the use of mega-nourishments (Brand *et al.*, 2022; Stive *et al.*, 2013). These mega-nourishments are sandy interventions in the coastal zone where large amounts of sediment (i.e., >500 m^3/m alongshore for beach nourishment or >1000 m^3/m alongshore for shoreface nourishment) are implemented. When mega nourishments are added to a beach, both cross-shore profile and alongshore shoreline curvature are strongly altered. This brings the coastal system out of equilibrium compared with its long-term average topography (de Schipper *et al.*, 2016).

The Hondsbossche Dunes mega-nourishment project is a man-made sandy beach system constructed of 35 million m^3 sand. It is placed in front of a sea dike that was considered a weak link in the Dutch sea defense (Fig. 2.1). The new sandy coastal defense consists of a shoreface, beach, and dune, aimed to increase safety against flooding while creating space for nature and recreation. As such, this project transferred (part of) the safety function from gray infrastructure to a soft sandy defense. The nourishment project significantly altered the coastal system in both along- and cross-shore directions. After placement, the newly created beach was on average 1.5–2 times wider, the subaqueous slope 1.5–2.5 times steeper, and the coastline curvature about 4 times larger than the adjacent coastal sections. The addition of large sediment volumes and the new cross-shore profile in a region that was protected by a dike for decades are bound to invoke a strong coastline response.

The planform adaptation of nourishments on the timescales of years is gen-

Figure 2.1.: a) Hondsbossche sea dike before placement of the nourishment (courtesy of Rijkswaterstaat, https://beeldbank.rws.nl/, accessed on 6 September 2021) and b) the Hondsbossche Dunes Nourishment just after placement in April 2015 (courtesy of Aannemerscombinatie Zwakke Schakel–Van Oord-Boskalis). The orange line marks the crest of the original sea dike.

erally assumed to be governed by wave-driven alongshore sediment transport gradients (Dean, 2002; Pelnard-Considère, 1957). Planform adaptation herein is symmetric in the alongshore, resulting in sediment accumulation in both adjacent beaches. Ludka *et al.* (2018) show that this spreading can also be asymmetric, with wave direction correlating to the displacement of the center of mass of the nourishment.

Cross-shore profile equilibration after nourishment implementation occurs typically in the order of weeks to years (Dean, 2002). Steep post-nourishment profiles adapt initially fast with sediment from the subaerial beach moving down slope (Dean, 2002; de Schipper *et al.*, 2016; G. Liu *et al.*, 2019). This first adaptation in the cross-shore can be strongly impacted by high-energy events (Elko & Wang, 2007). Over time, the profile equilibration slows down as the profile approaches a new dynamic equilibrium shape and steepness.

The beach width of the nourished beach is an important profile indicator from an economic and recreational perspective (e.g., Chang & Yoon, 2016; Gopalakrishnan *et al.*, 2011; Z. Liu *et al.*, 2016). After implementation of a beach nourishment, the beach is often at its widest and the reduction in beach width thereafter can be attributed to either horizontal movement of the waterline position, changes in dune foot position, or both. The variations in dune foot position originate from

dune erosion during storms and deposition of aeolian sand transport. Aeolian transport can bring sediment from the intertidal zone and beach to the dunes at different timescales (de Vries *et al.*, 2014b; I. J. Walker *et al.*, 2017), with many processes influencing the magnitude of wind-driven sediment transport (Bauer *et al.*, 2009). The resulting beach width is closely related to the shape of the dynamic equilibrium profile, as described by Bruun (1954) and Dean (1991). As such, the remaining dry beach width after nourishment can depend significantly on the size of nourished grains compared with native (Dean, 1991; Dean, 2002).

Large beach widths at mega-nourishments could lead to an increased dune volume over time (Galiforni Silva *et al.*, 2019) and create accommodation space for embryo-dune development (van Puijenbroek *et al.*, 2017). Yet, Hoonhout and de Vries (2017) report that at least half of the subaerial sediment deposits at a dune landward of a mega-nourishment may originate from the intertidal zone. Intertidal beach geomorphology may therefore be as important as the total beach width. Moreover, complex subaerial beach configurations (e.g., variability in dune front orientation) can cause (locally) increased or decreased deposition (Smyth & Hesp, 2015). Spatial differences in wave energy have also been related to differences in dune volume increase (Moulton *et al.*, 2021; Thornton *et al.*, 2007). High-energy events with wave run-up and storm surge can furthermore result in sediment deposition near the dune foot (Cohn *et al.*, 2018).

Expectations on the evolution of coastal state indicators, such as beach width (as proxy for recreation) and subaerial sediment volume (as proxy for coastal safety), are important in engineering practice and creating stakeholder support of mega-nourishments. Our aim is to document the subaqueous and subaerial beach changes at the Hondsbossche Dunes nourishment as a nature-based solution for integrated coastal development. Therefore, we investigate how beach width and profile volumes coevolve in the first five years after implementation of the Hondsbossche Dunes mega nourishment. We analyze the change in profile volume, beach width, and profile steepness at 250 m spaced transects measured on a quarterly to yearly basis and compare this evolution with that of the adjacent coast.

The next section will describe the Hondsbossche Dunes nourishment in more detail. In Section 2.3, the data and method are elaborated on, followed by the results of the data analysis in Section 2.4. In Section 2.5, the results are discussed and, in Section 2.6, the conclusions can be found.

2.2. Case Study

2.2.1. Coastal Setting

The Hondsbossche Dunes nourishment is situated at the Northern North-Holland (NNH) coast in the Netherlands. The NNH coast is a sandy, wave-dominated coast bounded by the Marsdiep tidal inlet in the north and the breakwaters of IJmuiden harbour in the south (Fig. 2.2b).

Prior to 2015, the NNH the sandy coastline was interrupted in the middle by the Hondsbossche and Pettemer sea defense. The sea dike had protected the

low-lying hinterland since 1887. This location protruded seaward with respect to the surrounding coastline, making it an erosional hotspot and a location where human interventions date back several centuries (Wijnberg & Terwindt, 1995). Both this sea dike and the adjacent sandy coastal sections contained regular-spaced shore perpendicular beach groins (Fig. 2.1). The nearshore bathymetry south of the sea dike (km 24–55, Fig. 2.2c) is characterized as a cyclic multiple (2–3) bar system, with offshore migration in a cyclic period of approximately 15 years (Wijnberg, 2002). The section north of the original sea dike (km 8-23, Fig. 2.2c) is characterized by a single nearshore bar without cyclic behavior. In this northern section, a shoreface shoal (the Pettemer Polder, km 20 Fig. 2.2c) is also present at a depth of about 10 m.

The native sand has a gradation between 250 and 300 μm around the waterline (Wijnberg, 2002). The material found in the dune ranges between 220 and 280 μm (Technische Adviescommissie voor de Waterkeringen, 1984). At deeper water (i.e., -5 to -10 m+NAP), the material is, in general, finer (van Alphen, 1987), ranging between 170 and 200 μm.

The NNH coast is exposed to a semidiurnal tide with a range of about 1.6 m. Mean low and mean high water are at ± 0.8 m+NAP (Rijkswaterstaat, 2013) (NAP is the Dutch reference level, roughly equal to mean sea level). Wind waves are mainly approaching from a southwesterly and northwesterly direction with longer period waves arriving mostly from the north (Wijnberg, 2002). The annual mean wave height H_s is 1.0 m, coinciding with wave periods typically of 4.3 s, at a depth of -10 m+NAP in the central part of the project site (location indicated with blue star in Fig. 2.2c). More extreme wave heights with a 1/20 y recurrence, at the same location, have a height H_s = 4.7 m and period of $T_{m-1,0}$ = 8 s. The full wave rose based on a 20-year time-series of hindcast waves (Kroon *et al.*, 2016) is presented in Fig. 2.2b. The spatial variation in the offshore wave climate along the Holland coast is small.

The net alongshore sand transport is estimated to increase over the NNH coast from 250,000 south to 550,000 m^3/m/y north (van Rijn, 1997). According to this estimate, the gradient over the project area is about 100,000–250,000 m^3/y. Since the 1980s, almost 70 nourishments have been placed along the NNH coast within the framework of the Dutch coastal maintenance program (Brand *et al.*, 2022). Before 2015, the nourishment volume was, on average, 1.55 million m^3/y at the NNH coast and 250,000 m^3/y at the project area, Table 2.1. In the post-construction period of the Hondsbossche dunes project evaluated here, five nourishments have been implemented along the NNH coast: a combined beach and shoreface nourishment was placed between 12.13 and 14.21 km in 2017 with a combined volume of 720 m^3/m; this was repeated in 2019 for the shoreface with a volume of 530 m^3/m, which makes an average of 550.000 m^3/y north of the project area for the period 2015 to 2020. A shoreface nourishment with a volume of 280 m^3/m was placed between km 31 and 40 in 2015 and repeated in 2019. Two beach nourishments with a volume of 220 m^3/m were placed between km 32 and 34 and between km 37 and 39 in 2015 and a beach nourishment with a volume of 200 m^3/m was placed between km 45 and 50 (Rijkswaterstaat, 2018,

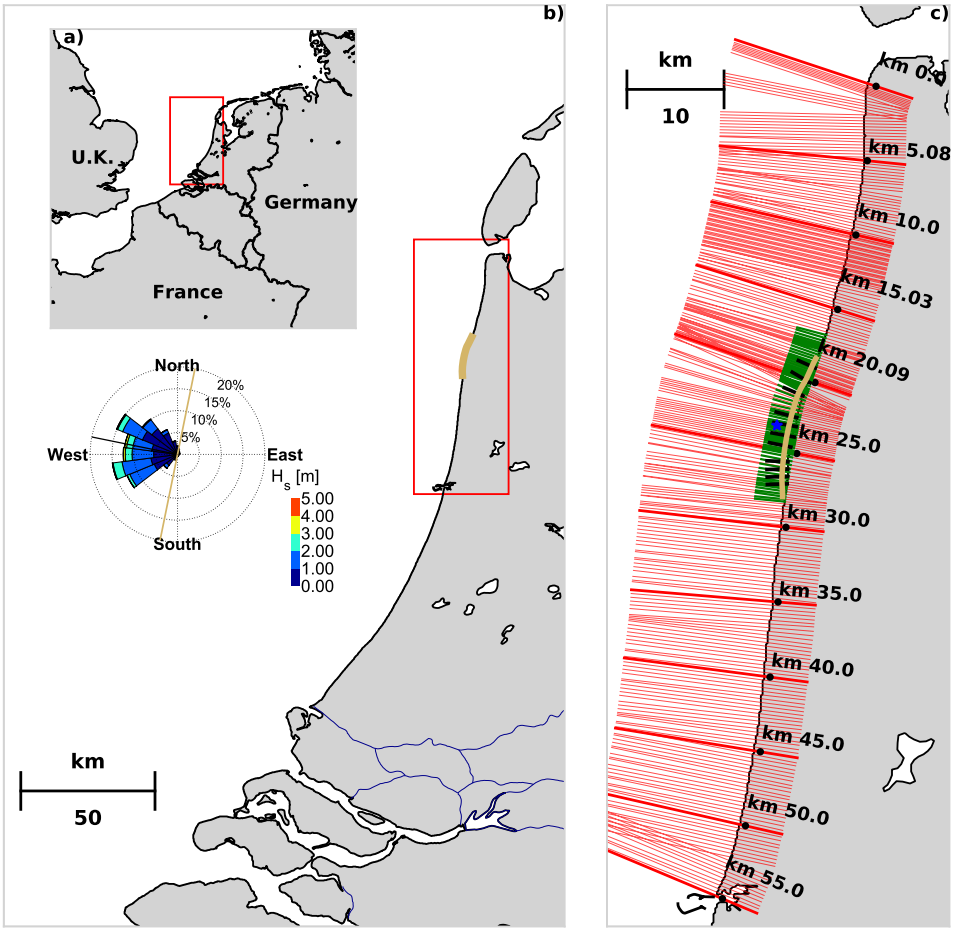

Figure 2.2.: Location of case study site and an overview of the survey transects from available datasets. a) Location of Dutch coastline within Europe. b) Location of Hondsbossche Dunes nourishment (yellow line) at the Dutch coast including local nearshore wave climate at HD at -10 m+NAP depth based on a 20-year hindcast time-series derived by Kroon *et al.* (2016). c) Location of transects from Jarkus (red), contractor survey transects (green), and 11 constructor high-temporal-resolution transects (black); the blue star indicates the location of the nearshore wave climate.

2020b), which makes an average of 1.400.000 m^3/y south of the project area for the period 2015 to 2020.

Table 2.1.: Total nourishment volumes [$\times 10^6 m^3/y$] at the NNH coast (Rijkswaterstaat, 2020c).

Period\KM	North 5–18.8	HD 18.8–28	South 28–50	Total 5–50
1986–2015	0.65	0.25	0.65	1.55
2015–2020	0.55	7	1.4	8.95

2.2.2. Hondsbossche Dunes Nourishment

The Hondsbossche and Pettemer sea dike was marked as a weak link in the Dutch sea defense with safety against flooding being below the desired level. Instead of dike reinforcement (e.g., heightening, widening), it was decided to increase safety against flooding by placing a sandy beach and (multirow) dune system in front of the dike. To achieve this purpose, a nourishment was designed that could meet the desired safety standard. This resulted in a nourishment of 35 million m^3 sand, with an average nourished volume of over 4000 m^3/m that exceeds locally 5000 m^3/m. The Hondsbossche Dunes nourishment is placed over a length of approximately 9 km coastline and covers almost 800 ha of subaqueous and 350 ha of subaerial domain.

The subaqueous profile was designed as a Dean (1991) profile fitted to observed profiles of the adjacent coast. Although in practice placed steeper, the placed subaqueous volume was sufficient to accommodate adjustment to a profile slope close to this expected dynamic equilibrium slope. This design philosophy was adopted to prevent large subaerial readjustments, albeit with uncertainty regarding the applicability of a Dean (1991) profile for a nourishment of this magnitude. The subaqueous profile is supplemented with a spatially varying buffer layer to compensate for expected alongshore losses, resulting in a design with wide beaches. The subaerial design is primarily based on a safety assessment with Duros+ (van Gent *et al.*, 2008) and an additional surcharge to account for the curved coastline (den Heijer *et al.*, 2012). Furthermore, the design included a dune valley, lagoon, and lookout dune to meet ecological and recreational demands (Fig. 2.1b).

Placement of the nourishment took almost a year, and finished in April 2015. The construction works were phased from south to north and from shoreface to dune. The nourished sand was dredged 10–15 km offshore of the project site. The nourishment is constructed with a sediment grain size varying between 225 and 350 μm to match the native sediment size as best as possible. After placement of the sand, the dune was immediately planted with marram grass and dune foot fences were installed to prevent nuisance of sand transport over to the landward side of the dike. In February 2018, an additional nourishment was placed in the south of the Hondsbossche Dunes project area between km 25 and 26.5 to increase the local beach width for recreation. This extra nourishment had a volume of approximately 1 million m^3 and was placed on the beach.

2.3. Methodology

2.3.1. Morphological Datasets

Beach width and profile volume response are examined using monthly to quarterly surveys acquired in the first five years after construction. The available data originate from three different sources (Fig. 2.3).

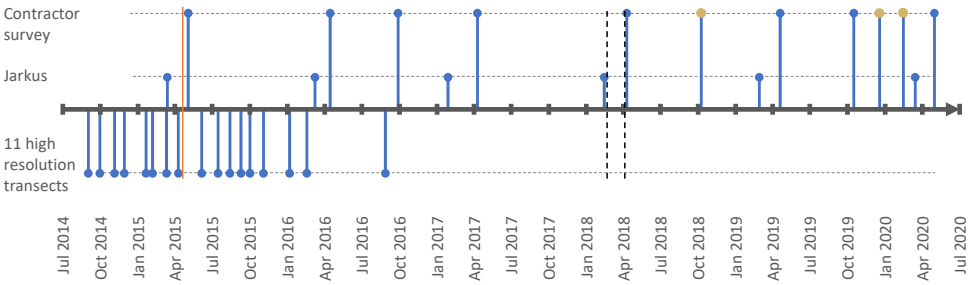

Figure 2.3.: Timeline of the survey data. Three datasets are used: 1. JARKUS surveys covering the full coastal cell; 2. Contractor surveys covering the 9 km project site; 3. Contractor transect surveys of 11 profiles with high temporal resolution shortly after the construction period. Red vertical line indicates the formal end of construction; black vertical lines bound the additional 2018 beach nourishment period. Yellow dots indicate subaerial surveys; blue dots indicate surveys that include both subaerial and subaqueous data.

The first is the JARKUS dataset from Rijkswaterstaat covering the entire Dutch coast with transects spaced approximately 250 m-apart (red lines, Fig. 2.2c) and acquired on a yearly basis (Rijkswaterstaat, 2020a). These surveys display the response of the entire coastal cell, ranging from the port of IJmuiden to the Marsdiep tidal inlet. The second dataset is acquired more frequently (approximately four subaerial and two subaqueous surveys per year) by the contractor and maps the response of the 9-km project site. These surveys consist of cross-shore transects spaced 250 m-apart. Originally, these were surveyed perpendicular to the newly created coastline and, therefore, deviated slightly in position and orientation from the JARKUS transects. To enable better comparisons, the transect locations were revised in summer 2017 to match the JARKUS lines (green lines in Fig. 2.2c). The third dataset contains 11 transects approximately 1 km-apart on which monthly to two-monthly measurements were taken by the contractor for a period of 1.5 years since the end of construction of each transect (black lines in Fig. 2.2c). For several southern transects, data are already available from the end of 2014 while construction at the northern transects was only finished in April 2015. These 11 transects follow the orientation of the postconstruction coastline. The surveys obtained by the contractor (dataset 2 and 3) use single beam echosounder for the subaqueous data and the subaerial data are gathered

mostly with LIDAR scans with occasionally walking GPS-RTK measurements.

The surveys that cover the entire nourished site in both the subaerial and subaqueous domain are gridded with a resolution of 2 m to examine the temporal evolution of the total volume change.

2.3.2. Data Reduction

To analyze the subaqueous and subaerial changes, the complex bathymetrical datasets are reduced to indicators that can be tracked in space and time and correlated to each other. First, these indicators are derived in the transect system of each dataset. Next, for overlapping or close positioned transects, these indicators are combined.

Sediment Volumes at Different Elevations in the Profile

The sediment budget of the nourishment and the adjacent coast are analyzed for various vertical slices representing the different subsections of the profile (dunes, beach, shoreface). The total profile-integrated volume is defined as the volume above -10 m+NAP, the level beyond which no significant bed level change is visible ($\sigma_{\Delta z} < 20$ cm) and seaward of the landward boundary. The lower shoreface volume is the lowest subsection analyzed, defined as the volume slice between -10 m+NAP and -4.8 m+NAP. The -4.8 m+NAP level represents the level above which 90% of the waves in the local long-term wave climate break, and is used to delineate between shoreface and surfzone subsections. The morphologically most active cross-shore section, the beach and surfzone, is bounded by -4.8 m+NAP and 3 m+NAP. Finally, the dune volume subsection is analyzed from the bed levels above 3 m+NAP and seaward of the landward boundary, Fig. 2.4. The landward boundary is chosen sufficiently far into the dune such that there is no significant sediment transport over it and its position does not affect the computed volume changes. Not all measurements extend until the landward boundary at each time step, for each transect. If not, these measurements are discarded for the total and dune volume change.

Beach Width, Shoreline Position, and Dune Foot

The beach width is defined as the distance between the waterline position and the dune foot position, Fig. 2.4. The waterline position is taken from the average of the cross-shore positions of the bed at the MHW and MLW levels, similar to the definition used by de Vries *et al.* (2012). The dune foot elevation is taken constantly at a level of 3 m+NAP, and dune foot position follows from the intersect with the cross-shore profile with the 3 m+NAP. There are many alternative definitions of dune foot, e.g., using a maximum slope change criterion (Smith *et al.*, 2020). The volume change analysis in this chapter is only marginally affected by this definition and, for simplicity, a fixed vertical level is assumed. Similarly, beach width changes on the time scales considered are hardly affected by the definition; however, absolute values of beach width can be more sensitive.

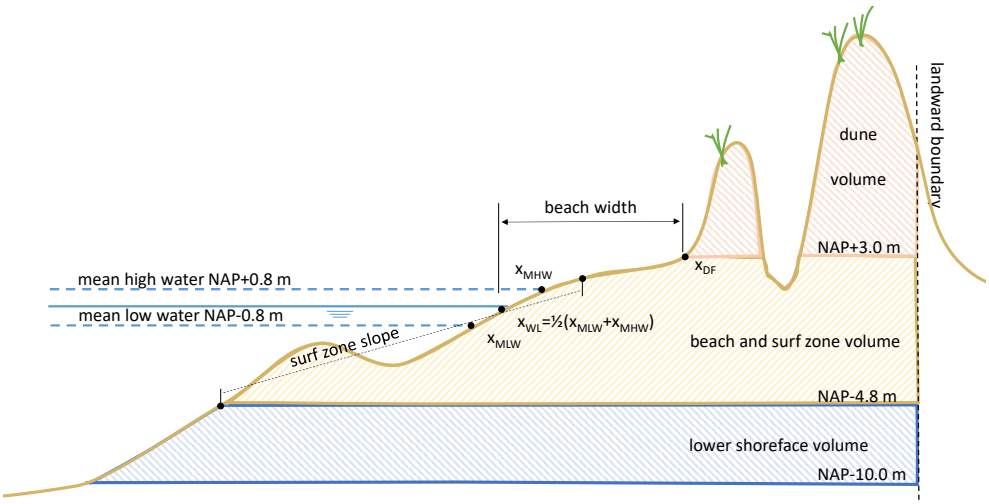

Figure 2.4.: Schematic cross-shore profile to illustrate the various profile parameters extracted from the survey data. NAP is the Dutch reference level, roughly equal to mean sea level.

Surfzone Slope

The surfzone slope is determined to examine cross-shore adaptation in the period directly following the construction. The slope is obtained from a least squares linear fit through the vertical elevations of the beach and surfzone bounded by the closest crossings with -4.8 and 1.5 m+NAP levels (Fig. 2.4), similar to the approach of de Vries *et al.* (2012). The upper level of +1.5 m NAP is chosen well-above the high water level to increase the robustness of the determined slope to inaccuracies around the interface of the subaqueous and subaerial measurements. Nevertheless, cross-shore slope values are sensitive to sandbars moving in and out of the evaluated elevation points. For the temporal evolution of the surfzone slope, the surveys before the formal end of construction are also included to map the response rapidly after the nourishment works.

Coastline Curvature

Coastline curvature is defined as the gradient in the orientation of the shoreline curve. This shoreline curve is obtained by connecting the cross-shore shoreline positions (as defined in Section 2.3.2) in the different transects. Before determination of the gradient, the shoreline curve is filtered with a uniform filter with an alongshore length of 1 km and averaged over the five-year evaluation period to remove small fluctuations. Finally, the gradient is computed using a second-order accurate central difference scheme.

2.4. Results

This section presents the data analysis of the Hondsbossche Dunes nourishment project. First, an overview of the morphological development in the five years after implementation of the nourishment is given. Second, the volumetric evolution over time is discussed with focus on different vertical zones (dunes, beach, surfzone, shoreface) and in the context of the larger coastal cell. Next, profile adjustment is presented and the subaerial evolution of the nourishment is assessed in more detail. Finally, the relationship between sediment budgets and concurrent changes in beach width and planform coastline curvature are examined.

2.4.1. General Morphodynamic Response of the Nourished Beach in Five Years

The bathymetric change in the five years after the nourishment works is illustrated using gridded plan view topographies (Fig. 2.5a,b) and profiles of selected transects (Fig. 2.6). The placement of the nourishment in front of the sea dike created a curved coastal section, protruding seaward with respect to adjacent beaches (Fig. 2.5a). The central part of this new beach system eroded (7 km out of the 9 km) in the first years after implementation of the project. This erosion is focused around the waterline and in the surfzone (Fig. 2.5c). During these years, both adjacent coastline sections experienced accretion. This accretion is present in the lower shoreface at the coastline sections where erosion transitions to accretion (km 20 and km 26) and extends in the cross-shore to the surfzone in sections further north and south. The coastline section with, predominantly, accretion in the north is larger in magnitude and intensity compared to the accretive section in the south.

The cross-shore profiles at the nourished site show the development of a double barred system with an outer bar approximately 500 m from the waterline with a crest height around -4 m+NAP and a more dynamic inner bar around 200 m from the waterline with a crest around -2 m+NAP (Fig. 2.6), similar to what is observed south of the HD. Bed level variations extend until a depth of approximately -10 m+NAP (Fig. 2.5c). Dune growth can be observed along the entire nourished site, either in the form of embryo dune establishment on the nourished beach, or dune face progradation and heightening of the first dune row (Fig.s 2.5c and 2.6).

2.4.2. Volumetric Changes

Although large volumes of sediment are displaced, the majority of the added sediment in the project area can be retraced over the five-year period. A volumetric budget of the entire 9 km placement area shows a loss of 1.6×10^6 m^3 by 2018 (Fig. 2.7, black symbols), which is less than 5% of the 35×10^6 m^3 initially added to the region. The 2018 nourishment of 1×10^6 m^3 resulted in a positive jump in volumes, but a small negative trend remained and, by 2020, (after 5 years) a

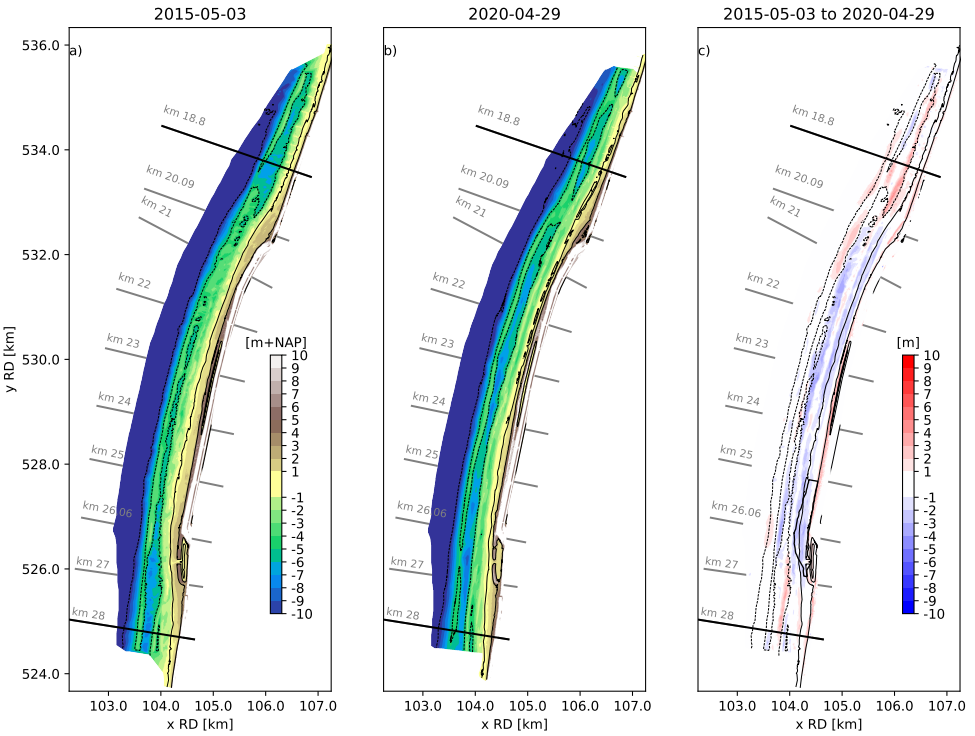

Figure 2.5.: Bed elevation data a) shortly after construction in May 2015 and b) after five years in April 2020. Colors show the bed elevation in meters with respect to the NAP datum (approximately MSL). c) Erosion (blue colors) and sedimentation (red colors) between the two surveys five years apart. The black dotted contour lines are based on the bed elevation of May 2015 (in panel a/c) or 2020 (in panel b) and indicate the -10, -4.8, 0, and 3 m+NAP isobaths. The black solid lines delineate the nourishment boundaries (km 18.8–28). The location of the additional 2018 beach nourishment is indicated with the black polygon.

loss of 1.4×10^6 m^3 is observed. Small fluctuations in volumes can be observed, which are likely due to survey inaccuracies and gridding of the transect data.

The 9 km-long sediment budget area is subdivided in the alongshore into a central section and two lateral sections to examine lateral diffusion of the nourishment. The central part of the nourishment shows a negative trend (Fig. 2.7, yellow symbols) with exception of the moment of placement of the 2018 nourishment. After five years, the 7 km-long central area has lost a volume of $\sim 3 \times 10^6$ m^3. The erosion from the center of the nourishment in the first year is $\sim 1.3 \times 10^6$ m^3, about twice as high as the following second and third years (Fig. 2.7, yellow symbols). After the third year, the volume in the central section increases

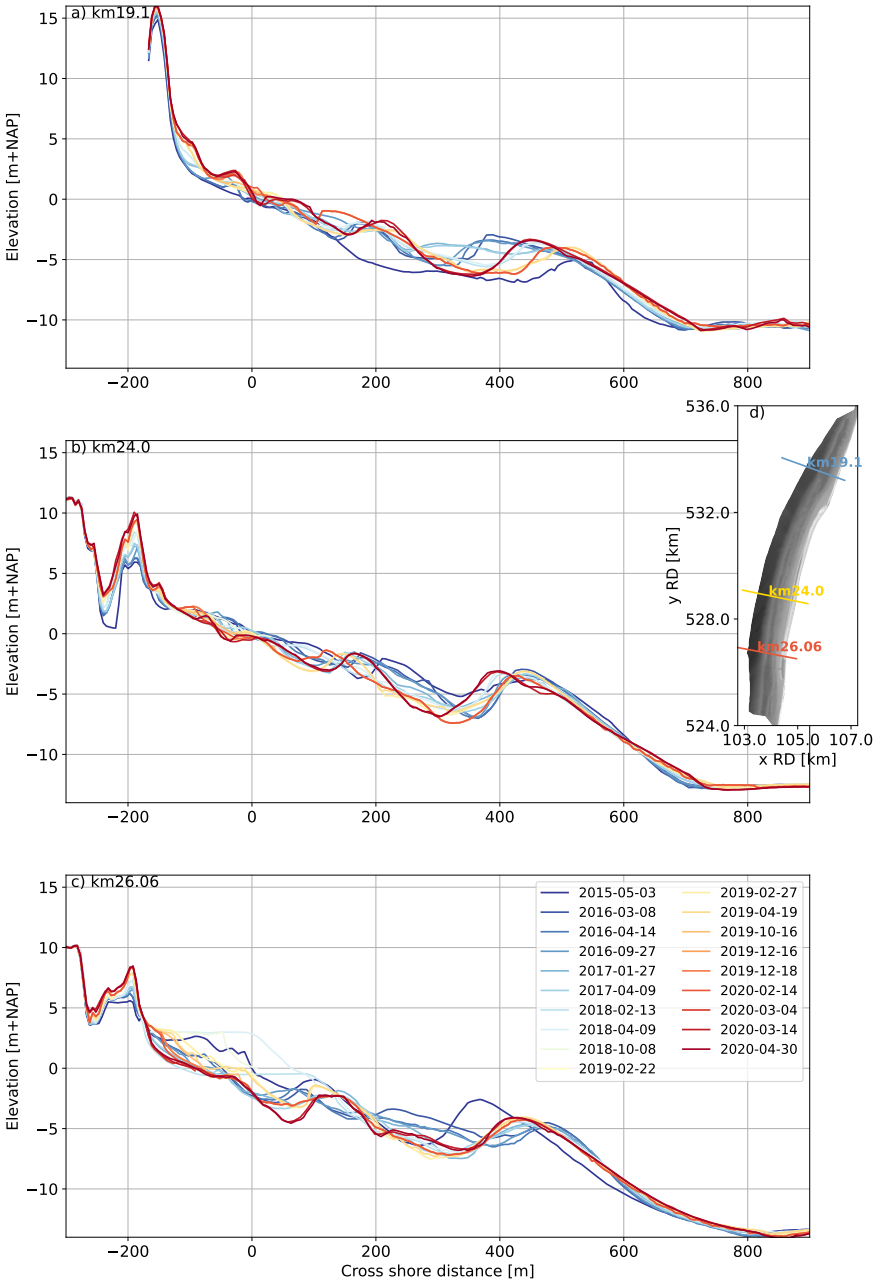

Figure 2.6.: Bed levels on three cross-shore transects. a) Northern transect at km 19.1. b) Central transect at km 24.0. c) Southern transect at km 26.06. Colors show the different surveys in time. d) The location of the transects in plan view. 0 m+NAP is approximately MSL.

with the additional 2018 nourishment. After this intervention, the central volume decreases further in the fourth and fifth years.

Opposed to the erosive central part, both lateral sides show a gradual accumulation of sediment with small fluctuations. The gained volume in the northern (Fig. 2.7, blue symbols) sediment budget section is about three times larger than in the south (Fig. 2.7, green symbols), while the coastal section is 1.5 times longer in the alongshore direction. This asymmetry is in agreement with the northward direction of the alongshore transport in this region (van Rijn, 1997).

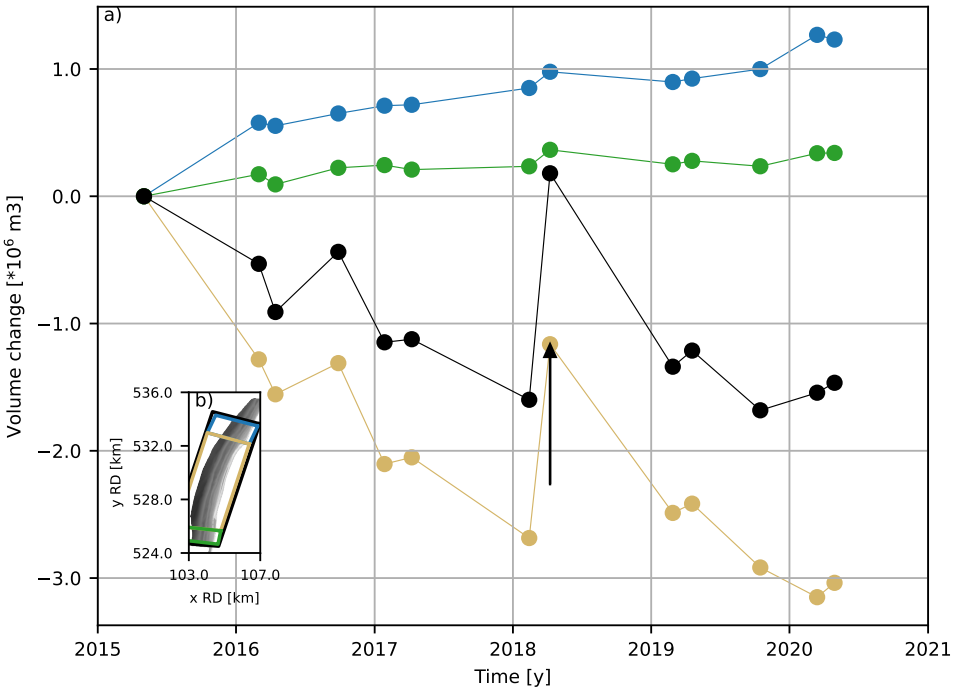

Figure 2.7.: Volume change above -10 m+NAP since April 2015 in three alongshore sections. a) The center of the project (km 20.23 to 27) (yellow), the adjacent beach north (km 18.8 to 20.23) (blue), the adjacent beach south (km 27 to 28) (green), and the total volume change for all sections combined (black). The black arrow indicates the moment and size of the additional 2018 nourishment of $\pm 1 \cdot 10^6$ m^3. b) Top view of the nourishment and locations of the volume polygons.

To obtain insight in the alongshore and cross-shore variations in time, the volumetric changes are further examined using seven transects. The profile-integrated volume changes of the transects located near the edges of the project area show accretion up to 1000 m^3/m alongshore (Fig. 2.8b, red and blue sym-

bols), where transects in the center of the project area show a loss in volume varying between 300 and 700 m^3/m after 5 years (60 to 140 $m^3/m/y$). Especially, the first two surveys after construction show large changes, followed by several surveys with more moderate adaptation (Fig. 2.8b).

Regardless of whether profiles are eroding or accreting (based on the profile-integrated volume), dune volumes mostly increase from survey to survey (Fig. 2.8c). The dune volume growth shows a significant variation among transects, between 40 to 300 m^3/m after 5 years (i.e., 8 to 60 $m^3/m/y$). The dune volume growth is largest for a profile at the center of the nourishment (km 24, yellow symbols in Fig. 2.8c). Here, volume gain in the dune is a significant part of the cross-shore sediment balance and of the same order of magnitude as volume losses below 3 m+NAP. At transects with a more moderate dune volume increase (e.g., km 21.23, 22.63, and 26.06) the dune volume increase is about five times smaller than the profile-integrated volume decrease.

Likewise, the volume change in the lower shoreface (-10 to -4.8 m+NAP) can locally be a significant contribution to the profile-integrated volume change (Fig. 2.8d). Especially for the central transects (km 22.63 to 26.06), the magnitude of the lower shoreface losses is ~50% of the profile-integrated sediment loss.

2.4.3. Changes in Perspective of the Morphodynamics of the Coastal Cell

The coastline curvature at the nourishment is stronger than that of the coastal cell (Fig. 2.9a). The original coastline slowly rotates 10° from 285 to 275 ° N over approximately 20 km (~0.5°/km) to the south of the nourishment project, and 20° from 295 to 275 ° N over 15 km to the north of the nourished site (~1.3°/km), while at the center of the nourishment, the coastline orientation changes 25 ° from 275 to 300 ° N in less then 7 km (~4°/km) (Fig. 2.9b).

Expansion of the sediment budget analysis to a larger 45 km-long coastal stretch shows that average annual volume changes per cross-shore profile vary in the alongshore direction between +250 and -250 $m^3/m/y$ over the period of 2015–2020 (Fig. 2.9c, blue line), with large fluctuations between years (Fig. 2.9c, blue shading), particularly for locations where nourishments have been implemented. The central beach of the Hondsbossche Dunes stands out as an erosional zone, with large volume losses of 100 $m^3/m/y$ (Fig. 2.9c,d). This erosional zone is consistent with the area where the coastline is strongly curved (Fig. 2.9b, km 20 to 27). Volume variations at adjacent coastal sections are, in general, of a smaller order of magnitude. Repeated nourishments (km 12.13–14.21 and 31–40, gray blocks in Fig. 2.9c,d,f) at the adjacent coast are visible as sections with a positive volume balance averaged over the 5 years. Sections with a positive volume balance are also visible next to the Hondsbossche Dunes nourishment and are related to spreading of the earlier-placed nourishment, feeding the adjacent coast (Fig. 2.9c, km 17–20 and 27–28).

Subdivision in the different elevations shows that, at the nourished site, profile-integrated volumetric changes (Fig. 2.9c) are dominated by variations in the

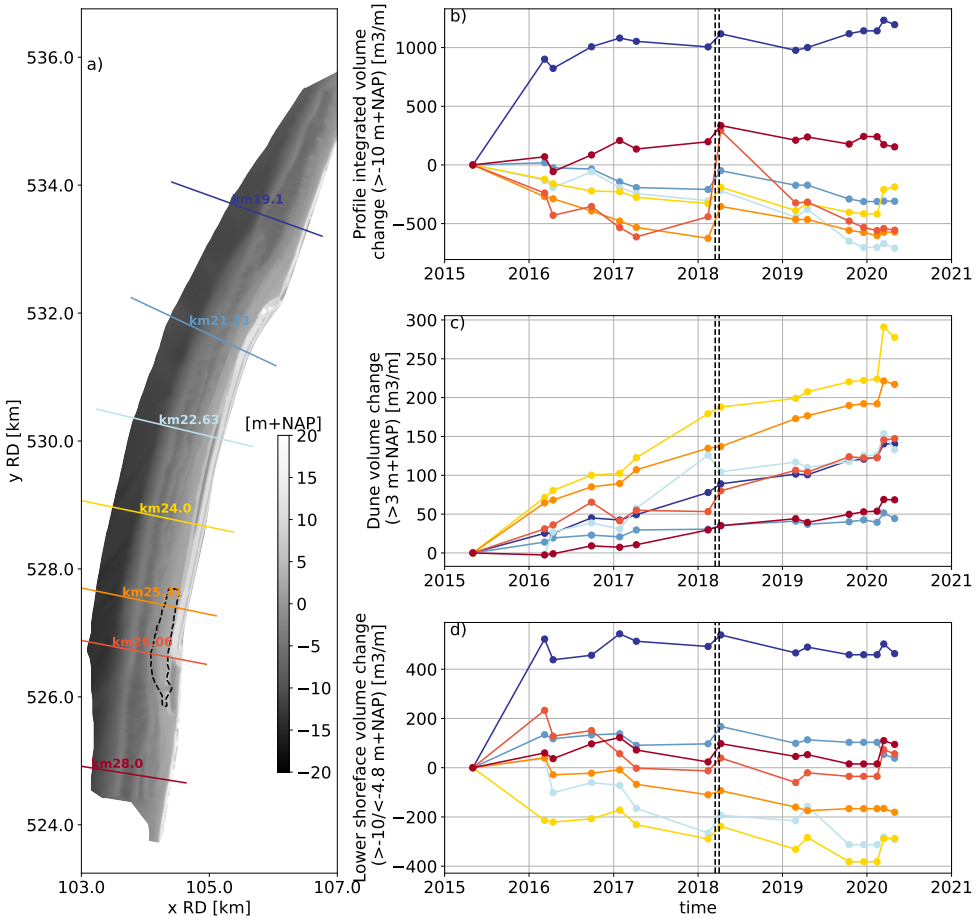

Figure 2.8.: Volume change over time for transects at km 19.1, 21.23, 22.63, 24, 25.31, 26.06, and 28. a) Location of transects (colored lines) and 2018 nourishment (dashed contour), b) profile-integrated volume change (>-10 m+NAP), c) dune volume change (>3 m+NAP), and d) lower shoreface volume change (between −10 and -4.8 m+NAP). The black dotted vertical lines indicate the period of the additional 2018 beach nourishment between km 25 and 27.

beach and surfzone elevations (Fig. 2.9d). Beach and surfzone changes are, respectively, 5 and 3 times larger than the average volume changes in the dunes or lower shoreface (Fig. 2.9e,f), but this ratio varies strongly alongshore. For instance, at the center of the nourishment (between km 24 and 25), a peak in deposition in the dune is observed, in combination with a reduction in beach and surfzone volumes resulting in a ratio of almost 1.

2.4.4. Cross-Shore Adaptation

The steepness of the cross-shore profile over time is examined and compared with values of the surrounding coast. The datasets contain several transects that are initially steeper than the adjacent coast. These steeper slopes adapt to a similar magnitude as the adjacent coast in the first two winters, Fig. 2.10b. This is not observed for all transects, as for some transects, monitoring started several months after construction had finished. Moreover, not all transects were constructed with the same initial steepness. For transects where the first surveys indicated a profile steepness similar or lower than the adjacent coast, no large change in slope is observed, Fig. 2.10c. The southern transects are initially very steep, two to four times steeper as the adjacent coast, but readjust and flatten over the first winter period (2014/2015) to a steepness about the maximum of that of the adjacent coast. In the next year, the profiles remain quite constant to become even flatter in the second winter. Placement of the 2018 nourishment steepens the local transect in the south, yet, also this is temporary and the profile steepness returns to its previous range. Construction at the more northern transects was still ongoing in the winter of 2014/2015. Nevertheless, these transects show a similar pattern with steepness values outside the range of the adjacent coast that decrease after the winter of 2015/2016.

2.4.5. Subaerial Evolution

Subaerial volume changes are relatively small compared with subaqueous zones but can be important for the assessment of safety against flooding or recreation potential. In this section, we examine the evolution of the subaerial beach through the spatial and temporal patterns in dune foot position and volume, and beach width.

The average dune volume increase over 5 years at the nourished beach is about 30 m^3/m/y (Fig. 2.11c) and peaks at almost 60 m^3/m/y at the center of the nourished section (km 24.0), showing there is a significant alongshore variation of deposition in the dune. In comparison, during the same period, dune growth at the adjacent coast is 15 m^3/m/y. Dune growth can occur through lateral expansion of the dune (i.e., seaward change in dune foot position), heightening of the dune, or both. At the Hondsbossche Dunes, both elements are visible. Dune growth in volume is, however, not always connected to lateral expansion (Fig. 2.11c,d). In the nourished section, the dune foot position changes on average 4 m/y seaward (Fig. 2.11d), twice as high as at the adjacent coast, at which the

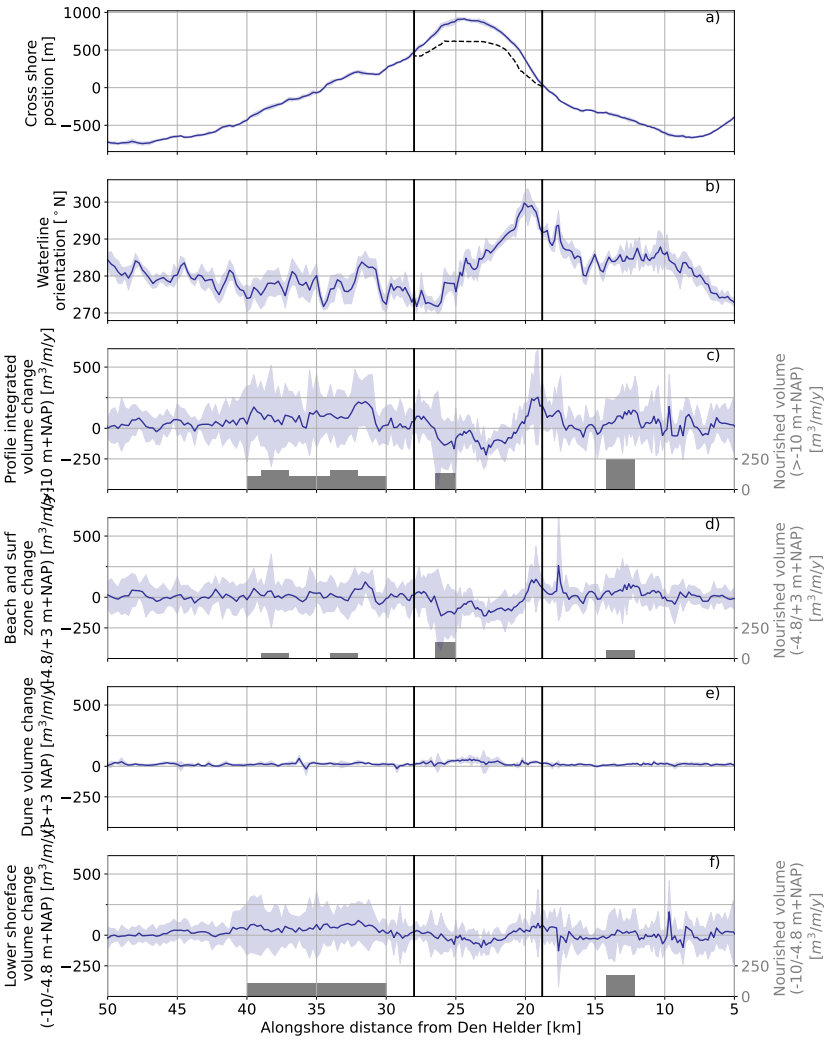

Figure 2.9.: Volumetric evolution of North-Holland coast with the nourished section in between the black vertical lines (JARKUS dataset only). a) cross-shore position of the waterline (relative to the waterline position at km 0.2), the position the prenourishment waterline in black stripes. b) Orientation of the waterline. c) Yearly profile-integrated volume change (>-10 m+NAP). d) Yearly volume change in the beach and surfzone (-4.8 m+NAP and 3 m+NAP). e) Yearly dune volume change (above 3 m+NAP). f) Yearly volume change on the shoreface (-10 m+NAP to -4.8 m+NAP). Blue shadings gives the $\pm\sigma$ interval and solid blue lines the average over the period April 2015–April 2020. The gray blocks indicate the nourishment volumes placed within the coastal cell in the period April 2015–April 2020.

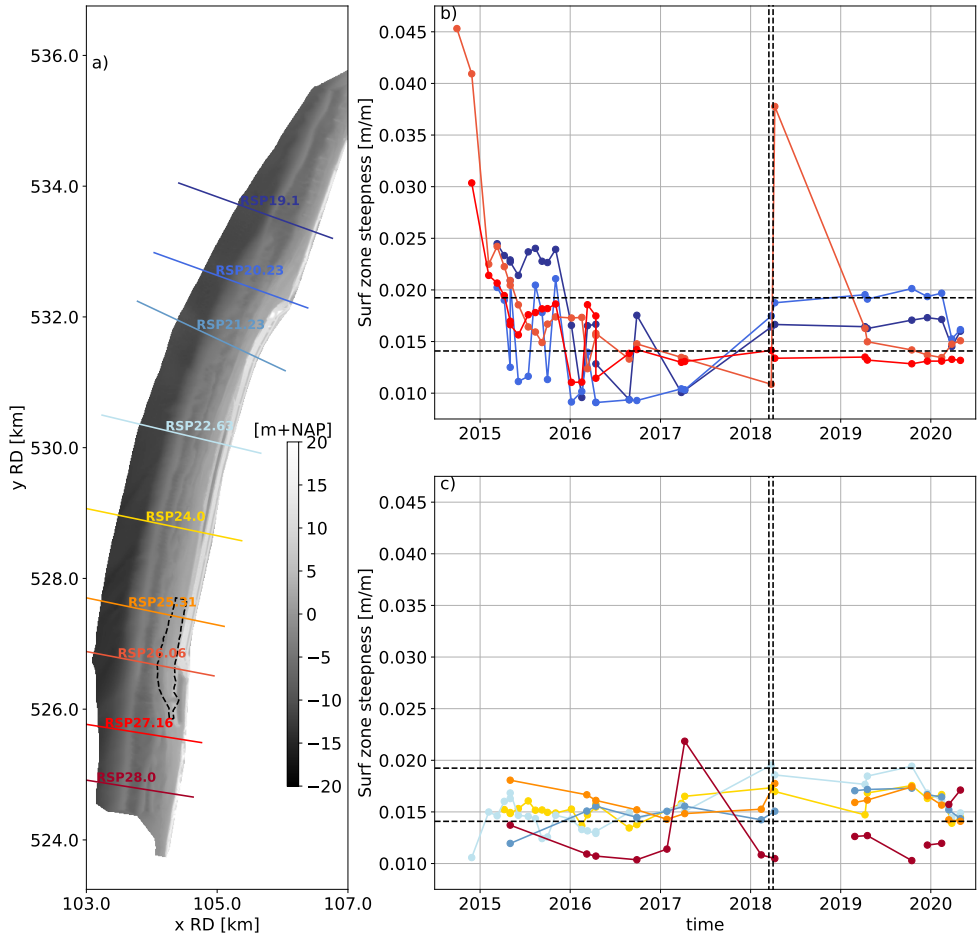

Figure 2.10.: Surf and intertidal zone slope (-4.8/1 m+NAP) adaptation in time. a) Location of transects and 2018 nourishment; b) slope at initially steeper profiles at km 19.1, 20.23, 26.06, and 27.16; c) slope at initially smoother profiles at km 21.23, 22.63, 24.0, 25.31, and 28.0. The black dotted horizontal lines indicate the $\mu \pm \sigma$ profile steepness of the adjacent coast. The black dotted vertical lines indicate the period of additional beach nourishment between km 25 and 27.

dune foot position changes 2 m/y seaward. Two nourished sections in the larger coastal section (km 12.13–14.21 and 31–40) stand out as zones with a large seaward movement of the dune foot. An exceptionally large dune foot change is found at the northern transition zone of the nourishment (±km 20), where the local dune foot has progressed with over 50 m. This is the result of the local infill of a discontinuity in the first dune row. This discontinuity resulted from a step-back in the constructed dune at the transition to the adjacent coast. Although the dune foot migrates forward by 50 m at this location, this is not reflected in larger dune volume changes (Fig. 2.11c, ±km 20).

The nourished beach at the Hondsbossche Dunes is on average 180 m-wide directly after construction. This is about twice the width of the surrounding beaches where the average beach to the south is 83 m and to the north is 101 m-wide (Fig. 2.11e). The beach width adapts rapidly over the years as a consequence of both fluctuations in the land–water interface, and seaward migration of the dune foot (Fig. 2.12c,d). The contribution of dune foot migration to the changes in the beach width is substantial at the nourished site: on average, 20% of the total beach width change and, locally, more than 35%.

At the eroding part of the nourished site, between km 20.23 and 27, the beach width decreases by about 80 m (Fig. 2.12b, round markers). The majority of the reduction occurs in the first two years, after which the beach width adaptation slows down and converges to beach width values similar to the adjacent coastal sections. Transects 25.31 and 26.06 are an exception as the beach width is disturbed by the placement of the additional nourishment in 2018. The beach width reduction at the eroding transects is primarily caused by a landward change in waterline position (60 m of the 80 m reduction in beach width). This change in waterline position is initially fast but slows down over time (Fig. 2.12c). From the landward end, beach width is reduced by a more constantly prograding dune foot of, on average, 20 m seaward.

The beach width in the accretive lateral sections of the nourishment displays no clear trend (Fig. 2.12b, triangular markers). At these transects, the seaward migration of the waterline (20–50 m) is similar to the seaward migration of the dune foot (30–40 m) (Fig. 2.12c,d).

2.4.6. Profile Volumes and Beach Width Changes as Function of Coastline Curvature

The observations of volume change and beach width change at the Hondsbossche Dunes are correlated to evaluate their dependence. This is performed using the JARKUS dataset only, because it is the most consistent dataset to cover both the subaqueous and subaerial domains for the entire evaluation period. For the nourished section, the beach width change ΔW_b and total profile-integrated volume changes ΔV are well-correlated ($r^2 = 0.75$, Fig. 2.13a). Changes in waterline position Δx_{sl} correlate even better with the volume change ($r^2 = 0.84$) as noise introduced by dune foot position changes is excluded from the relation (Fig. 2.13c). The coastline curvature is an important driver of nourishment

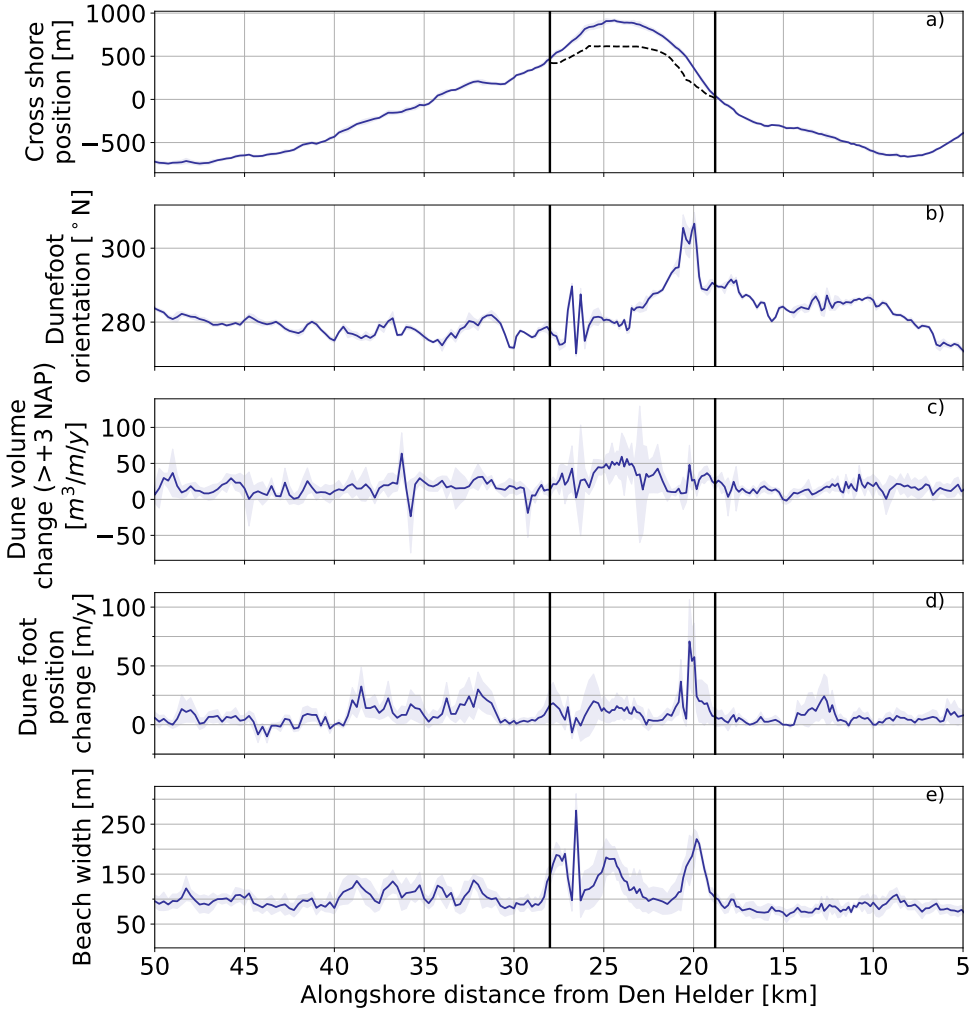

Figure 2.11.: Dune evolution of North-Holland coast with the nourished section in between black lines (JARKUS dataset only). a) Cross-shore position of the waterline (relative to the waterline position at km 0.2); the position of the prenourishment waterline is in black stripes. b) Orientation of the dune foot. c) Dune volume change, above 3 m+NAP. d) Dune foot position change. e) Beach width.

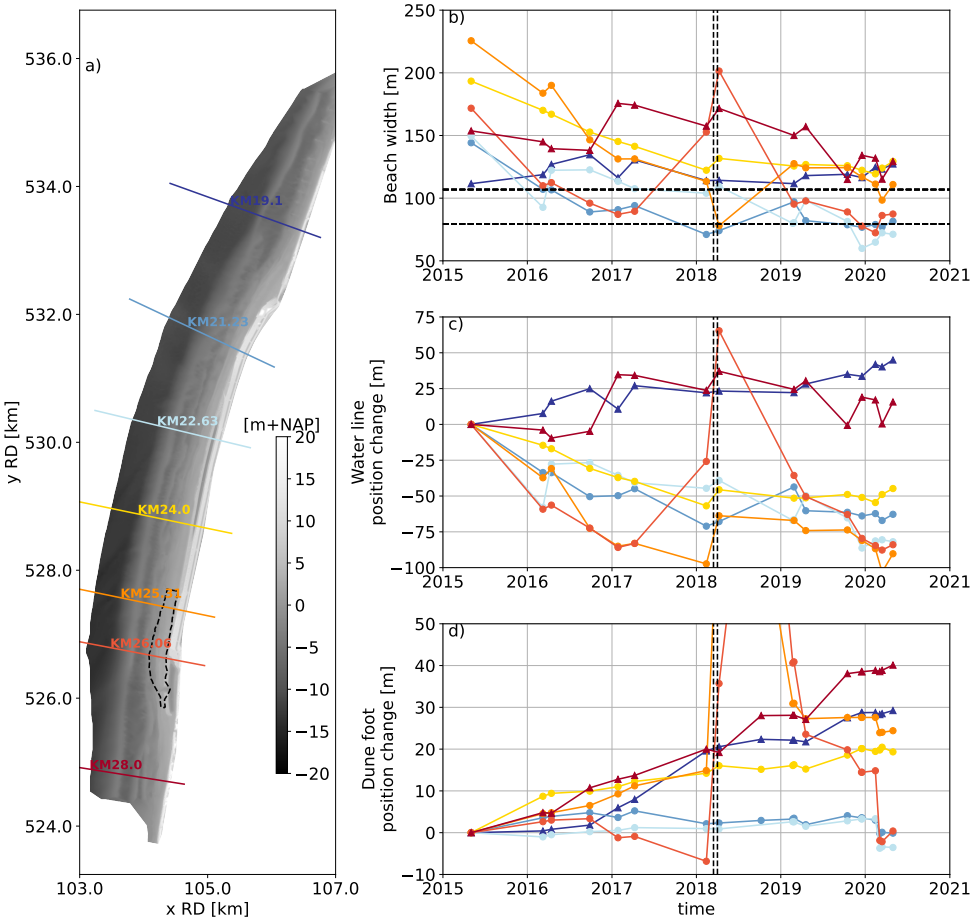

Figure 2.12.: Beach width in time for transects 19.1, 21.23, 22.63, 24, 25.31, 26.06, and 28. a) Location of transects. b) Beach width. c) Waterline position change. d) Dune foot position change. The black dotted horizontal lines indicate the $\mu \pm \sigma$ beach width at the adjacent coast. The black dotted vertical lines indicate the period of the additional 2018 beach nourishment. Eroding and accretive transects are marked with circle and triangle symbols, respectively.

adjustment (e.g., Dean, 2002; Pelnard-Considère, 1957). For the Hondsbossche Dunes, both volume change and beach width change indeed correlate well with curvature ($r^2 = 0.47$ and $r^2 = 0.54$, respectively, Fig. 2.13b,d), confirming the importance of alongshore wave-driven sediment transport for both indicators.

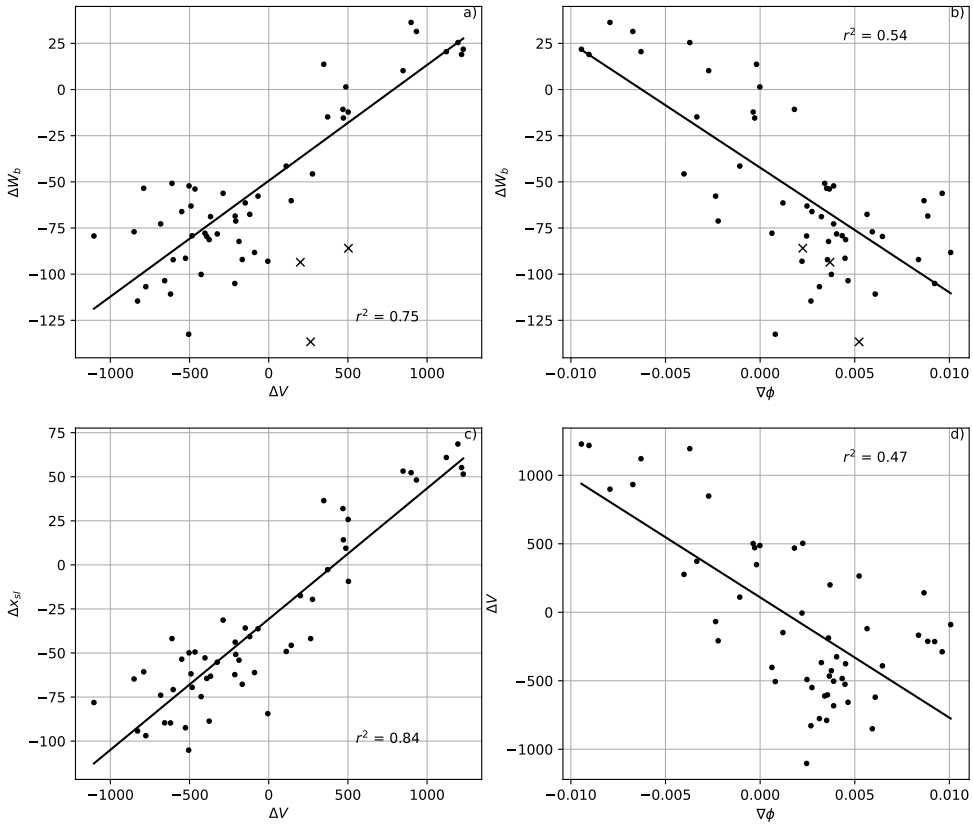

Figure 2.13.: Correlations of profile volume change, beach width, coastline position, and coastline gradient. a) Correlation of profile volume change and beach width change, b) coastline gradient and beach width change, c) coastline position change and volume change, and d) coastline gradient and volume change. Data points are for the project area only and based on JARKUS dataset, for the period between April 2015 and 2020. Observations marked with a cross are treated as outliers in the determination of the correlation coefficients. Beach width changes at these locations are dominated by alongshore infilling of a local stepback in the dunefront at the edge of the original sea dike (see Fig. 2.11a,d km 20–20.5).

The least squared linear regression line relating beach width and volume change

intersects the $\Delta V = 0$ m^3 line at negative values, estimating around 50 m reduction in beach width for profiles with no net volume change (Fig. 2.13a). Similarly, the regression line relating volume change and waterline position crosses $\Delta x_{sl} =$ -30 m at $\Delta V = 0$ m^3 (Fig. 2.13b). These offsets are considerable compared to the range of beach width changes observed ($\pm$100 m). Suggesting that, next to profile volume changes, cross-shore redistribution of volume is an important contribution to beach width change in the first five years.

2.5. Discussion

2.5.1. Beach Width and Dune Growth

The initially wide beach at the Hondsbossche Dunes project significantly reduced over the five years investigated. The landward trend in waterline position is found to be the main contribution to the beach width changes (in the order of several meters per year) and about two to four times the magnitude of the seaward shift in the horizontal dune foot position (Fig. 2.8). This dominance of waterline position changes over fluctuations in dune foot are similar to observations at a nearby natural beach (Quartel *et al.*, 2008). In general, fluctuations and trends in waterline position occur on a range of scales (i.e., seasonal and storm scales to interannual scales (e.g., Griggs & Patsch, 2018; Ludka *et al.*, 2016; Quartel *et al.*, 2008; Yates *et al.*, 2009)).

The observed net landward migration of the waterline after implementation of a nourishment may be caused by alongshore gradients in sediment transport as well as redistribution of the (nourished) sand downslope in the cross-shore direction. The cross-shore adaptation at smaller nourishments is reported to occur primarily in the first months or year after implementation (Larson *et al.*, 1999; Marinho *et al.*, 2018; Park *et al.*, 2009), with high-energy wave events playing an important role (Browder & Dean, 2000; Elko & Wang, 2007). Volume and beach width changes at the Hondsbossche Dunes in the last years are also smaller than the first year (Fig. 2.12b), which is in line with results of these earlier studies where cross-shore redistribution is initially strongest. Further, the rapid adjustment of the cross shore slope in the first two winters (Fig. 2.10) is in line with reported reductions in slope adjustment at other nourished sites (Elko & Wang, 2007; Roest *et al.*, 2021). For the large nourishment investigated here, the cross-shore equilibration of the profile is not limited to the subaqueous profile and sediment moving downslope, as sketched by Dean (2002) and Elko and Wang (2007). Dune growth is a substantial part of the sediment budget and post-nourishment equilibration (Fig. 2.14).

Alongshore sediment transport gradients impact waterline position through both the planform adaptation of the nourishment and the pre-existing background erosion rate (Dean & Yoo, 1992; Verhagen, 1996). We observe a total shoreline retreat of up to 100 m for transects with large net volume losses (Fig. 2.13c), about 70 m more than locations with minimal volume losses (Fig. 2.13c,

Figure 2.14.: Schematic view of observed cross-shore behavior at the Hondsbossche Dunes nourishment including an increase in dune volume and equilibration of beach width, modified from Elko and Wang (2007).

points near $\Delta V = 0$). This underlines that alongshore effects are critical to understand changes in terms of beach width at this nourishment.

Furthermore, the analysis reveals contrasting trends of the waterline migration (driven by marine processes) and dunefoot migration (dominated by aeolian processes), resulting in a reduction in the beach width from both land and seaward sides over the past years. This is indicative of nourished beaches during the first period with no or minimal dune erosion, and similar to findings of Bezzi *et al.* (2009). At these wide, nourished beaches, the dune foot may move seaward (Fig. 2.15b) due to aeolian transport, but as the beach erodes in the following years the dunes become more prone to erosion (Cohn *et al.*, 2019; de Vries *et al.*, 2012; Itzkin *et al.*, 2021). More severe and frequent dune erosion events will likely shift the dune foot landward and can bring the waterline seaward. Several transects have reached beach widths similar to the adjacent coast (within the $\mu \pm \sigma$ range of 89 to 107 m) after five years (Fig. 2.12a). At these locations, some initial retreat in dune foot position (Fig. 2.12c) and an increase in beach width suggests stabilization after the last winter (Fig. 2.12a). These observations are early signs that future beach widths at the nourished site may fluctuate within a similar range as the adjacent coast.

In the cross-shore direction, an increase in dune volume is observed regardless of the net trend in the profile volume below ($r^2 = 0.06$, Fig. 2.15a). While dune volume gains are up to five times smaller than total volume change (50 m^3/y compared to 250 m^3/y, Fig. 2.9), sediment accumulation in the dune can locally be a significant component in the cross-shore sediment balance and contribute to the safety against flooding. The observed average dune volume increase over the nourished site is 30 m^3/m/y (Fig. 2.11), which is similar to the upper limit of measured dune growth at the Dutch coast (de Vries *et al.*, 2012). In contrast

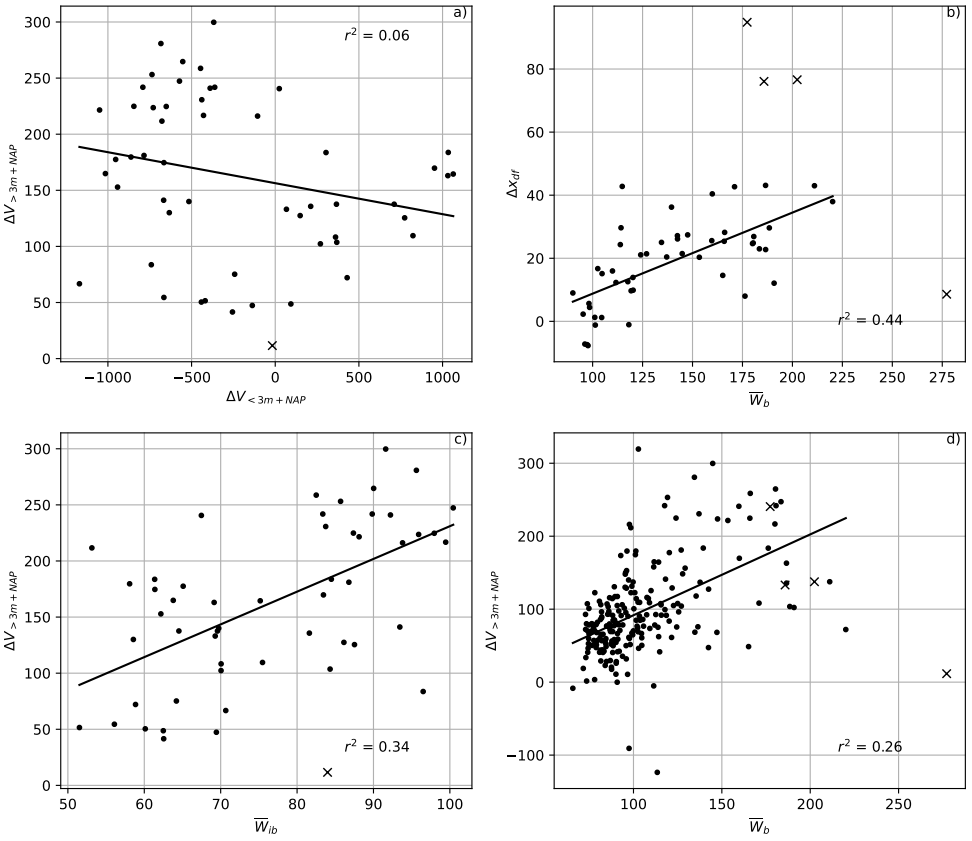

Figure 2.15.: Correlations of beach width and volume changes. a) Correlation of volume change below 3 m+NAP and volume change above 3 m+NAP; b) average beach width and dune foot position change; c) average intertidal beach width and volume change above 3 m+NAP at the Hondsbossche Dunes; and d) average beach width and volume change above 3 m+NAP at the NNH coast for the period between April 2015 and 2020. All values are based on the JARKUS dataset only. Observations marked with a cross are treated as outliers in the determination of the correlation coefficient. At these locations, dune foot changes are dominated by an alongshore infilling of a local stepback in the dune front at the edge of the original sea dike (Fig. 2.11a,d km 20–20.5) or beach width and dune volume cannot be determined appropriately according to our definition due to a local opening in the dune in front of the lagoon (Fig. 2.11e km 26.5).

to earlier observations of larger dune growth in the first year after implementation of a nourishment (e.g., Hoonhout & de Vries, 2017; van der Wal, 2004), we observe no significant difference in dune volume gains between the subsequent years. From an engineering perspective, the observed average growth of 150 m^3/m in the post-nourishment period is significant and an important contribution to safety against flooding. To put the observed dune growth in perspective of the Dutch coast, the average dune erosion is estimated to be around 20–100 m^3/m during a 1/30 year event (Athanasiou *et al.*, 2021) and 100–800 m^3/m (100–250 m^3/m at the NNH coast) in case of an extreme event (1/10,000 y) (den Heijer, 2013).

The dune volume increase shows significant variability in the alongshore direction and peaks in the center of the nourishment around km 24 (Fig. 2.11). Dune development can be sensitive to beach width, beach sediment budget, shoreline orientation, vegetation and sediment, or surface properties amongst others (e.g., de Vries *et al.*, 2014a; Moulton *et al.*, 2021; Silva *et al.*, 2017; Wijnberg *et al.*, 2021). For the Hondsbossche Dunes, we observe that dune foot migration is correlated to beach width ($r^2 = 0.44$, Fig. 2.15b), where larger beach widths result in more seaward migration of the dunefoot. A similar correlation between beach width and changes in dune volume cannot be found at the nourishment. However, Fig. 2.15d shows that the behavior of the nourishment compared to the adjacent coast by including the entire coastal cell into the evaluation does result in a correlation. Although small, the larger dune growth at the Hondsbossche Dunes does show a positive correlation with the locally large beach width ($r^2 = 0.26$, Fig. 2.15d). The variation in dune growth at the nourishment itself is correlated with the width (W_{ib}) of the intertidal beach instead ($r^2 = 0.34$, Fig. 2.15c). This is in line with previous observations that large parts of aeolian sediment deposits originate from the low-lying beach that is regularly reworked by waves (Hoonhout & de Vries, 2017).

2.5.2. Predicting Beach Width and Volume Change

Predictions of coastal dynamics are complex due to the large range of phenomena involved (e.g., Thieler *et al.*, 2000) and remain a challenge despite the advances made in the last decade (Ranasinghe, 2020). Simple curve-fitting methods can provide good results to describe aggregated parameters of nourished beaches, such as remaining volume in the project area (Weathers & Voulgaris, 2013).

For a detailed view of the shoreline behavior, one-line type coastline models (e.g., Dabees & Kamphuis, 1999; Hanson, 1988; Hurst *et al.*, 2015; Pelnard-Considère, 1957; Roelvink *et al.*, 2020) can provide information on post-nourishment development of the beach in a computationally efficient manner (de Schipper *et al.*, 2021). These models simulate the redistribution of sediment alongshore based on alongshore gradients in wave action, coastline gradient, or sediment availability. At the Hondsbossche Dunes, volume changes are indeed correlated with shoreline curvature ($r^2 = 0.47$, Fig. 2.13d), confirming one of the key

underlying assumptions of one-line models. One of the important parameters in these one-line models is selecting an active profile height, which is often estimated from an upper limit on the beach (e.g., the dunefoot or berm height at 3 m above MSL) and a depth of closure. At the Hondsbossche Dunes, the inner and outer closure depth are approximately 8 to 12 m below MSL using Hallermeier's formulas (Hallermeier, 1981, 1983). This roughly coincides with the observations of the lowest point of observed bed level changes at ± -10 m+NAP (Fig. 2.6). The Hondsbossche Dunes analysis also gives an additional option to estimate the active profile height based on the the linear regression line between profile volume change and shoreline position (Fig. 2.13c). The reciprocal of the slope of the regression line can be interpreted as a representative active profile height of 14 m (i.e., 1/0.07). The similarity in values indicates that Hallermeier's formulas could have been used to estimate the closure depth in the nourishment's design phase.

The obtained correlations between volume change, coastline curvature, and beach width indicate that one-line models can be used to predict the response of nourishments on the scale of the Hondsbossche Dunes. Nevertheless, several limitations of one-line models can be illustrated with the data of the Hondbossche Dunes. First, the correlation between volume change and coastline curvature for several subsections of the nourishment is significantly higher ($r^2 > 0.6$) than the averaged value ($r^2 = 0.47$) for the project site, suggesting that the relative importance of coastline gradient as a driver of volume changes varies alongshore. Alongshore variations in offshore wave conditions, grain size d_{50}, or lower shoreface slope may potentially explain part of the remaining variance. Not all these parameters are or can be captured by a one-line model. Secondly, one-line models typically do not include cross-shore redistribution of sediment. Considering the significance of the cross-shore equilibration on initial waterline position changes, it is important to calibrate a one-line model on net volume changes rather than waterline position changes for nourished beaches. Calibrating on waterline positions may result in an overestimation of shoreline retreat since the initial cross-shore adjustment could falsely be extrapolated to a longer time-scale. Furthermore, the subaerial response and dune foot migration is often not resolved separately by one-line models, while this is essential to estimate the beach width development and dune growth.

For the aforementioned nourishment aspects, planform process-based modeling techniques may potentially be used, such as in previous mega-nourishment design studies (e.g., Bodde *et al.*, 2017; Kroon *et al.*, 2016; Mulder & Tonnon, 2011). To predict the beach width response including alongshore variability and dunefoot migration, as observed at the Hondsbossche Dunes site, an explicit representation of the subaerial beach may be necessary. The recently developed coupled hydrodynamic and aeolian processed-based models (Cohn *et al.*, 2019; Itzkin *et al.*, 2022; Luijendijk *et al.*, 2017b; van Westen *et al.*, 2024) show potential to predict this behavior in the near future.

2.5.3. Implications for Design

In the Hondsbossche Dunes project, a beach dune system was created in front of an old sea dike. The man-made sandy system was aimed to increase safety against flooding while adding additional value. The design was inspired by Building with Nature principles, amongst others aiming to use natural forces to support our human objectives (de Vriend *et al.*, 2015).

Our analysis suggests that after an initial adjustment period, the artificial beach system obtains comparable characteristics to the adjacent coast in terms of beach width and surfzone slope, despite the large quantities of added sand. Its exposed location in front of the sea dike and inherent coastal curvature will likely result in continued redistribution of sediment to the adjacent coast. The adjacent coast will benefit from the spreading of this sediment similar to the feeding effect of the Sand Engine (de Schipper *et al.*, 2016; Roest *et al.*, 2021). The sediment supply to the adjacent coast could be considered an amenity of reinforcement of gray infrastructure with a seaward sandy extension.

For creating and maintaining safety against flooding with a coastal nourishment, sediment volume above storm surge level is critical. Adding sediment at higher elevations in the profile during construction is often costly due to the machinery shaping the profile. Rapid downslope transport of this sand during erosion events is undesired and inefficient. Our results show that the design of the Hondsbossche Dunes nourishment, with a natural slope and wide beach, proved to be successful in creating a positive sediment balance in the dune for a prolonged period after placement. With a dune volume increase at the nourished site three times higher than the surrounding beach sections, natural forces are indeed partaking in the building of strong flood defenses.

2.6. Conclusions

Sandy nourishments have been applied as coastal engineering interventions for decades. Lately, projects using millions of m^3 of added sand to replace gray coastal infrastructure (e.g., dams, dikes, seawalls) have been initiated. This thesis presents the morphological development of the Hondsbossche Dunes (the Netherlands), a nourishment of 35 million m^3 in front of an old sea-dike. The Hondsbossche Dunes is a unique area of newly created beach and dunes, aimed to increase safety against flooding while creating space for nature and recreation. Nearly twenty topographic surveys in the first 5 years after placement are used to examine the redistribution of sediment volume in both the along- and cross-shore directions and the adaptation of the post-nourishment profiles with initially wide beaches.

In the first years after implementation, large local volume changes up to 1000 m^3 per meter alongshore were observed. Yet, net volume losses in the 9 km coastal section were less than 5%, indicating that reworking was mostly local. The central part of the nourished site stands out as an erosive zone, with large (60 to 140 $m^3/m/y$) erosion. This erosion is predominantly in the subaqueous part of the profile and coincides with a shoreline retreat of about 80 m. Lateral coastal

sections on the other hand show large accretion and a waterline migration of around 30 m-seaward. The man-made cross-shore beach profile rapidly mimics the adjacent beaches, as the surfzone slope is adjusted within two winters to a similar slope.

The seaward sandy extension of the sea dike creates a significant coastline curvature. The observed net profile volume change is, at several sections of the nourishment, strongly correlated ($r^2 > 0.6$) with this planform curvature. In our observations, the local change in waterline position, ΔX_s, correlates well with the volume change in the full profile ΔV_p ($r^2 = 0.84$). Finding this strong correlation suggests that the use of one-line models is appropriate when predicting the volume and coastline change of mega-nourishments.

An important observation is that the subaerial and subaqueous parts of profiles display contrasting behavior in the first years after placement. The dune volume increases in the first years after implementation with 30 m^3/m/y; for many profiles, this net gain in volume is found regardless of the erosive trend in the lower part of the profile. The magnitude of the dune volume increase at the nourished site is three times higher than at the adjacent coast. This implies that the nourishment is bringing additional sediment volume above surge level, which is key to coastal safety.

As the dune foot migrates in the seaward direction and the shoreline moves landward, the beach width is reduced from two sides. The initially wide beaches (i.e., up to 225 m) are transformed in five years to about 100 m-wide, similar to adjacent beaches. The similarity in beach widths near the end of the five years investigated suggests that upcoming storm events may be able to erode sediment from the dunes, potentially reducing the excessive net growth of dune volume in the near future. Our results demonstrate that several years may be needed for the sandy cross-shore profile to reach characteristics similar to the nearby coast, after reinforcement of gray infrastucture. Natural forces can provide a significant additional contribution to the building of dunes during these years, further increasing the safety against flooding.

3

Wave climate variability versus model uncertainty in predicting the evolution of a large-scale intervention

Abstract

Sand nourishments are increasingly applied as adaptive coastal protection measures. Predictions of the evolution of these nourishments and their impact on the surrounding coastline contain many uncertainties. The sources that add to this uncertainty can be delineated between intrinsic and epistemic uncertainty, i.e. inevitably in the system or related to knowledge limitations. Effects of intrinsic uncertainty (e.g., due to wave climate variability) on coastal evolution can be significant. In studying these effects, it has often been assumed that intrinsic uncertainty is dominant over epistemic uncertainty (e.g., introduced by the model), yet the magnitude of both contributions have not been explicitly quantified to assess the validity of this assumption. This Chapter examines the relative importance of intrinsic and epistemic uncertainty in coastline modeling of a large-scale nourishment. It uses a probabilistic framework in which sediment transport is considered to be a function of random wave forcing (intrinsic) and model (epistemic) uncertainty, calculating transport using a one-line model. The test case for this analysis is the mega-nourishment, the Sand Engine, located in the Netherlands. The applied wave climate variability is obtained from long term wave observa-

This chapter has been published as: **Kroon, A.**, de Schipper, M.A., van Gelder, P.H.A.J.M. and Aarninkhof, (2020) S.G.J., *Ranking uncertainty: Wave climate variability versus model uncertainty in probabilistic assessment of coastline change*, Coastal Engineering **158**, 6 (103673).

tions, whereas model uncertainty is quantified using the Generalized Likelihood Uncertainty Estimation (GLUE) method relying on monthly observations. We find that the confidence intervals on predicted volume losses increase substantially when including both intrinsic and epistemic sources of uncertainty. A global sensitivity analysis shows that ignoring model uncertainty would underestimate the variance by at least 50% after a 2.5-year simulation period for the Sand Engine, hence producing significant overconfidence in the results. These findings imply that for coastal modelling purposes a dual approach should be considered, evaluating both epistemic and intrinsic uncertainties.

3.1. Introduction

Coastal sections around the world are increasingly protected with sand nourishments. Yet, using natural dynamics and materials in coastal protection is intrinsically associated with increased uncertainties of the coastal state with respect to more traditional hard protection measures. Recent nourishments along the Dutch coast such as the Sand Engine (de Schipper *et al.*, 2016) and the Hondsbossche Dunes (Kroon *et al.*, 2017) show a significant increase of nourishment volume compared to the more regular beach and foreshore nourishments (Stive *et al.*, 2013). As intervention scales grow and natural variabilities are increasingly incorporated in these designs, the demand for predictions increases, while predictability of the state of the coast at any given time has decreased. In addition to this uncertain response to variable natural forces, many model related uncertainties are present, which are not always included in predicting these coastline changes.

In general, distinction is made between two types of uncertainty, intrinsic and epistemic uncertainty (e.g., van Gelder, 2000; van Vuren, 2005). The first is related to the random occurrence of processes in time and space and is irreducible. The second is related to the present state of our process knowledge, models and methods and is in theory reducible given appropriate resources. In Fig. 1.1 the types of uncertainty in morphological coastline predictions are schematized, adapted from the schematic subdivision of types of uncertainty in design of civil structures by van Gelder (2000).

In morphological coastline response on a yearly to decadal time-scale intrinsic uncertainty can manifest in both space and time. For instance, the spatial variability in the cross-shore bed levels can have significant influence on the alongshore transport (Mil-Homens, 2016). Likewise, coastal morphology is very sensitive to temporal variability such as the chronology and year to year variability in wave forcing (Southgate, 1995).

Epistemic uncertainty is typically introduced by uncertainties in observations and models. Model uncertainty can be attributed to model inadequacy, parameter uncertainty (e.g., Ruessink, 2005; Simmons *et al.*, 2017) and numerical limitations (e.g., de Vriend, 1987). Model inadequacy can be caused by missing processes (e.g., beach recovery, long waves, sediment sorting; Huisman *et al.*, 2016) or reduced complexity of processes, such as 1D or 2D models and sediment

transport formulae. Ruessink and Kuriyama (2008) show that unpredictability of cross-shore sandbar migration during major wave events originates largely from model inadequacy. Parameter uncertainties arise from limited knowledge on actual values of model parameters (e.g., grainsize, bed roughness or wind shear). For instance, Villaret *et al.* (2016) show that model results are most sensitive to settling velocity and grain size, which are often only locally known. Numerical uncertainties can be introduced by the spatiotemporal model resolution, the order of the numerical schematization and the acceleration technique (Luijendijk *et al.*, 2019). Finally, observation uncertainty is a result of accuracy of the instruments and data processing used. For instance, sampling limitations and measurement errors can significantly contaminate variability at resolved scales, and may lead to errors in the representation of the scales of interest (Kasprak *et al.*, 2019; Plant *et al.*, 2002).

In the last decades, large advances have been made to model and predict the morphological processes governing the changes of the coastal zone (Ashton & Murray, 2006; Hanson, 1988; Lesser, 2009; Warner *et al.*, 2010). Thereby making a significant contribution to the accuracy and skill of morphodynamic models, and thus reduction of model uncertainty. However, as focus has been on improvements and strengths of the model, less detail is presented on the residual uncertainty. Recently, several of these tools have successfully been applied to the modeling of large-scale nourishment evolution (Arriaga *et al.*, 2017; Luijendijk *et al.*, 2017a; Tonnon *et al.*, 2018). Although, Arriaga *et al.* (2017) do acknowledge the sensitivity of the results to different wave climate scenario's, in general, only limited attention is paid to the uncertainties within the predictions of these models.

On a track adjacent to model development and improvement, several of these deterministic models have been applied within probabilistic frameworks to allow for the effects of intrinsic uncertainty (Baart, 2013; Baquerizo & Losada, 2008; Callaghan *et al.*, 2013; Ranasinghe *et al.*, 2012; Ruggiero *et al.*, 2010). The implicit assumptions underlying the focus on intrinsic uncertainty are that climate variability is the most important source of uncertainty and that model forcing and reliability are independent. That the validity of these assumptions is debatable, is indicated by the results of Callaghan *et al.* (2013), who show that model uncertainties have a significant influence on probabilistic estimates of storm erosion: the predicted mean erosion and 95% confidence interval vary greatly for each of the models presented and all models overestimate erosion for higher return periods. For the long, climate change time scale, Le Cozannet *et al.* (2019) show that model uncertainty can indeed be a significant contribution to variance in coastal recession predictions under a rising sea level.

Explicit quantification of model (parameter) uncertainty (epistemic uncertainty) in morphological computations is possible, albeit at a large computational cost (e.g., Kroon *et al.*, 2019; Ruessink, 2005; Simmons *et al.*, 2017). Similarly, it is possible to quantify intrinsic uncertainty in morphological model applications in the coastal zone on a time scale of years (Baquerizo & Losada, 2008; Payo *et al.*, 2008). Yet, combining these to assess the relative importance of epistemic

versus intrinsic uncertainty has not been investigated so far.

In coastal engineering the deterministic approach might dominate and probabilistic approaches focus on intrinsic uncertainty, uncertainty analysis in climate change predictions is common practice. In general, three main sources of uncertainty in climate projections are identified: due to future emissions (scenario uncertainty), due to internal climate variability, and due to inter-model differences (Hawkins & Sutton, 2009, 2011; IPCC Working Group I, 2013). Hawkins and Sutton (2011) show clearly that for climate projections the dominant source of uncertainty depends on lead time, climate indicator and spatial scale. Extending these results to coastal morphology, it seems unlikely that intrinsic uncertainty or wave climate variability can be beforehand considered to be the primary source of uncertainty for both short and long time scales. Therefore, this Chapter includes both intrinsic and epistemic uncertainty in a probabilistic framework to examine the relative importance of these uncertainties in coastline modeling of a large-scale nourishment over time.

For this purpose, sediment transport and volume change are considered to be a function of both intrinsic and epistemic uncertainty. As the principal source of intrinsic uncertainty we choose the variability in wave climate and as the principal source of epistemic uncertainty we assume model uncertainty. The random wave forcing is based on the observed wave climate variability whereas the distribution of the calibration settings for a simple one-line model are quantified using observations of the Sand Engine nourishment. With a comparison of the observed volume changes and several probabilistic forecasts that include wave climate variability and/or model uncertainty, we show that model uncertainty becomes dominant over wave climate variability for medium-term time scales (years).

3.2. Sand Engine nourishment

The Sand Engine is a well measured nourishment project, and its large scale results in a distinct and unique coastline response with a high signal to noise ratio. The Sand Engine nourishment was placed between April and June 2011, along the Dutch South Holland coast, as a hook shaped peninsula of 17 million m^3 sand (Stive *et al.*, 2013). The nourishment is exposed to a wind wave climate with a predominant South-West and North-West direction. The spring-neap tidal range varies approximately between 1.5 and 2 m and the local tidal velocities around the peninsula can range up to 1 m/s (Radermacher *et al.*, 2017), but the main driver of the morphological evolution is the alongshore sediment transport by oblique wave incidence (Luijendijk *et al.*, 2017a). The bathymetric evolution has been monitored with a 1 to 3 month interval until the end of 2016 and with a 3 to 6 month interval after that (Roest *et al.*, 2017). The grain size (d_{50}) of the Sand Engine varies over the cross-shore profile and in time between approximately 200 and 400 μm (Huisman *et al.*, 2016), and morphological changes can be observed between -8 and 3 m+MSL (de Schipper *et al.*, 2016).

Our analysis starts with the bathymetrical survey of December 2012 because

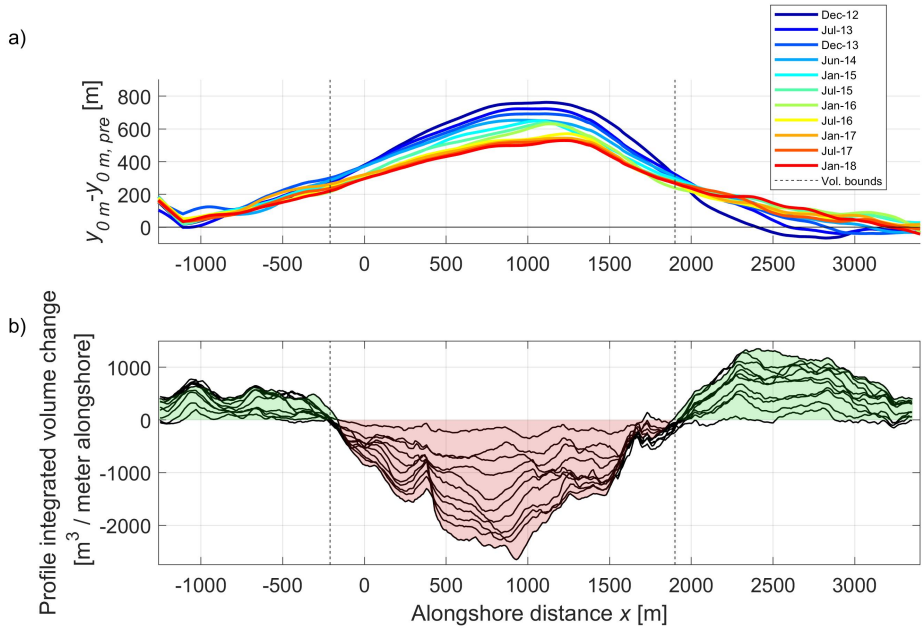

Figure 3.1.: Morphological evolution of the Sand Engine since December 2012. a) Coastline position, y_{0m}, with respect to a reference coastline, $y_{0m,pre}$, prior to construction of the nourishment and b) profile integrated volume change since December 2012. The green shaded areas denote net sedimentation and the red shaded area denotes net erosion.

the coastline curvature is too sharp for a one-line model to be stable prior to this date. The remaining 5 year period between December 2012 and January 2018 is split in two 2.5-year periods: a calibration period and a validation period. The coastline is defined as the position of the most seaward 0 m+MSL depth contour, ignoring the lagoon. The resulting coastline positions since December 2012 are depicted in Fig. 3.1a. For each of the surveys the profile integrated volume change with respect to the bathymetry of December 2012 is calculated (Fig. 3.1b). The total volume change (ΔV_{tot}) of the nourishment since December 2012 is calculated as the sum of the net eroding center part of the nourishment (shaded red in Fig. 3.1b) and shows a negative trend of approximately 500,000 m^3/y (Fig. 3.2a). The volume changes between consecutive surveys (ΔV) vary between 100,000 $\pm$ 160,000 m^3 (Fig. 3.2b). A large volume gain of 8,000 m$^3/d$, influenced by an observational error, is reported in August 2013. This volume gain is not excluded, exemplifying the effect of measurement errors in the analysis.

To derive model boundary conditions, offshore waves at nearby wave stations

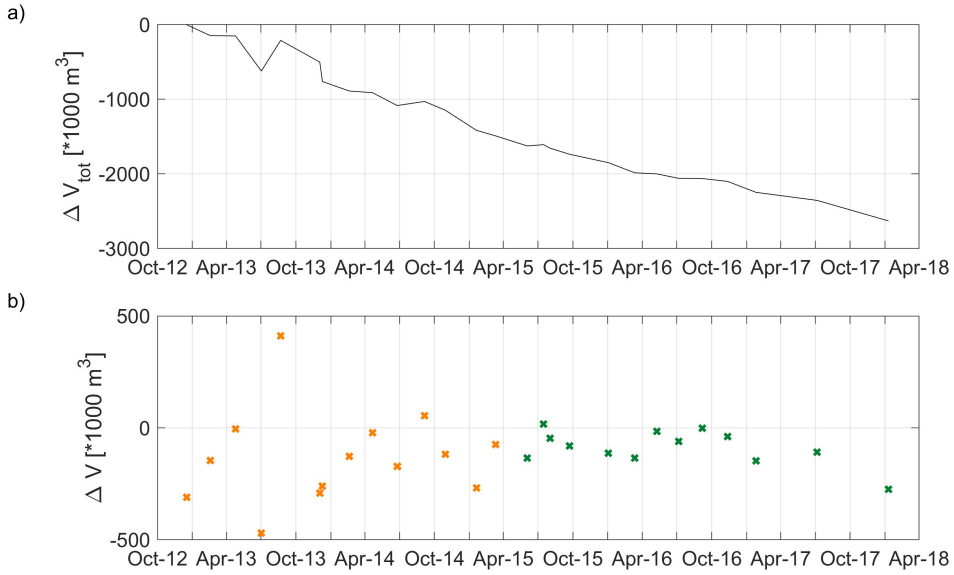

Figure 3.2.: a) Total volume change (ΔV_{tot}) since December 2012 and b) volume change (ΔV) between consecutive surveys of the central, net eroding area of the Sand Engine. Orange crosses are used for model calibration and green crosses are used for validation. The positive volume change in August 2013 is influence by measurement errors.

are transformed to the -10 m+MSL depth contour with a SWAN model using a transformation matrix derived for the Sand Engine by Deltares (2011) in a similar way to Ly and Hoan (2018). A description of the mesh and a validation for a nearby measurement station can be found in Huisman *et al.* (2019). The resulting wave height time series (Fig. 3.3) are separated into three periods: a full 25-year period to quantify the wave climate variability, (January 1986 - January 2011), a 2.5-year calibration period (December 2012- June 2015) and finally a 2.5-year forecasting period (June 2015-January 2018).

3.3. Methodology

3.3.1. Probabilistic approach

To examine the relative importance of model uncertainty versus the effects of wave climate variability in predicting coastline change a probabilistic simulation procedure is followed (Fig. 3.4). For the morphological computations a one-line model is chosen, to facilitate the large number of computations required to achieve a high statistical accuracy.

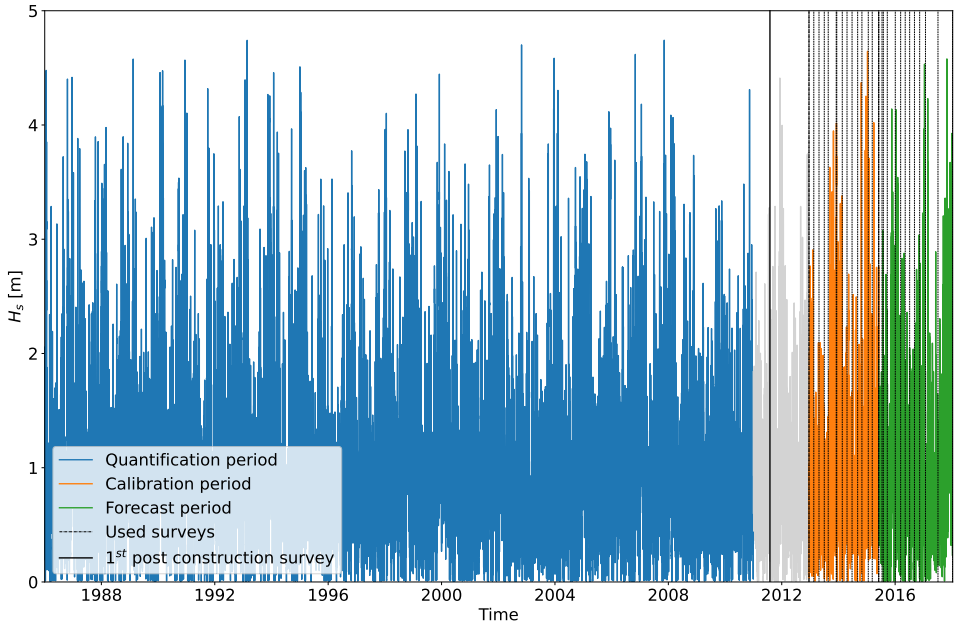

Figure 3.3.: Wave height at the -10 m+MSL depth contour at the Sand Engine for the quantification period (1986-2011), the calibration period (December 2012-June 2015) and the forecast period (June 2015-January 2018). Gray dotted lines depict the survey dates. The wave data from January 2011 to December 2012 are not used in the analysis (shown in gray).

The first step in the procedure is to quantify uncertainty. The variation in wave climate is quantified using the statistics of 25 years of wave observations (Fig. 3.4, left side of blue dotted box). Model uncertainty is quantified using Generalized Likelihood Uncertainty Estimation (GLUE) (Beven & Binley, 1992) that seeks a distribution of appropriate model settings for the 2.5-year calibration period, given a set of observations (Fig. 3.4, right side of blue dotted box). The next step is to sample from the established distributions of wave climate variability and model uncertainty. So, with a bootstrapping procedure N model time series are generated that meet the observed wave statistics (Fig. 3.4 left orange box). Whereas N model settings are derived by Monte Carlo sampling (Fig. 3.4 right orange box) from the derived distribution of model settings. After the deduction of N wave time series and N model calibration factors the uncertainty is propagated through the one-line model by running it N times for the 2.5-year forecast period (Fig. 3.4, green box). For each of these runs the volume change in the eroding part of the nourishment is determined, and combining these results provides a probability density function of volume change. We choose $N = 12,000$ samples,

this means that we can be 95% sure that the 50% fractile is located between the estimates of the 49% and 51% fractile (Morgan *et al.*, 1990).

In the next part of this section the details of the one-line model and the uncertainty quantification steps are further elaborated upon. Finally, the relative importance of wave climate variability and model uncertainty in this probability density function of volume change is assessed with a global sensitivity analysis (see paragraph 3.3.5).

3.3.2. One-line model

Many one-line models can be found in literature with a varying range of complexity (e.g., Arriaga *et al.*, 2017; Hanson, 1988; Payo *et al.*, 2002; WL|Delft Hydraulics, 1994). In this study a one-line model is used which updates the cross-shore coastline position based on the alongshore sediment transport gradient and neglects any sources or sinks:

$$\frac{\delta y_s}{\delta t} + \frac{1}{D}\frac{\delta Q}{\delta x} = 0 \tag{3.1}$$

in which x is the alongshore coastline position, y_s is the cross-shore coastline position, Q is the alongshore sediment transport, and D is the active profile height between closure depth and top of the berm. In this approach the alongshore sediment transport rate is calculated with the Kamphuis formula (Kamphuis, 1991):

$$Q = K \tan(\beta)^{0.75} d_{50}^{-0.25} \underbrace{H_{br}^2 T_p^{1.5} \sin^{0.6}(2\theta_{br})}_{\text{wave climate component } (w_{br})}, \tag{3.2}$$

where Q is expressed as kg immersed mass per second, K is the model calibration factor, $H_{s,br}$, T_p and θ_{br} are the significant wave height, peak period, and angle of wave incidence at the point of breaking relative to shore normal, $\tan(\beta)$ is the beach slope and d_{50} is the median particle size in the surf zone. For the purpose of this study we denote the term that is affected by varying wave forcing as the wave climate component, w_{br}.

To obtain volume change, ΔV_{tot} the coastline change is integrated over the active profile height, D, and the alongshore grid size, Δx, and then summed over the alongshore central section of the nourishment (Fig. 3.1, dashed lines).

We discretize the coastline of the Sand Engine in non-uniform spaced sections in the x-direction that vary between 200 and 225 m width. H_{br} and θ_{br} are calculated using linear wave theory from waves at a location beyond the closure depth, the -10 m+MSL depth contour. The wave conditions at the -10 m+MSL depth contour are assumed to be constant over the model domain. In addition, we assume d_{50}=300 μm, a beach slope of 1/50 and an active profile height D=11 m. Note that, assuming these specific values may introduce uncertainty in time and space which will be accounted for via calibration of the model calibration factor K as a probability density distribution.

The model calibration factor K as originally proposed by Kamphuis (1991) has a value of 2.33, assuming a sea water density of $\rho = 1029$ kg/m^3. Later, Schoonees and Theron (1996) use an extensive data set to find a value of $K = 3.6$ for

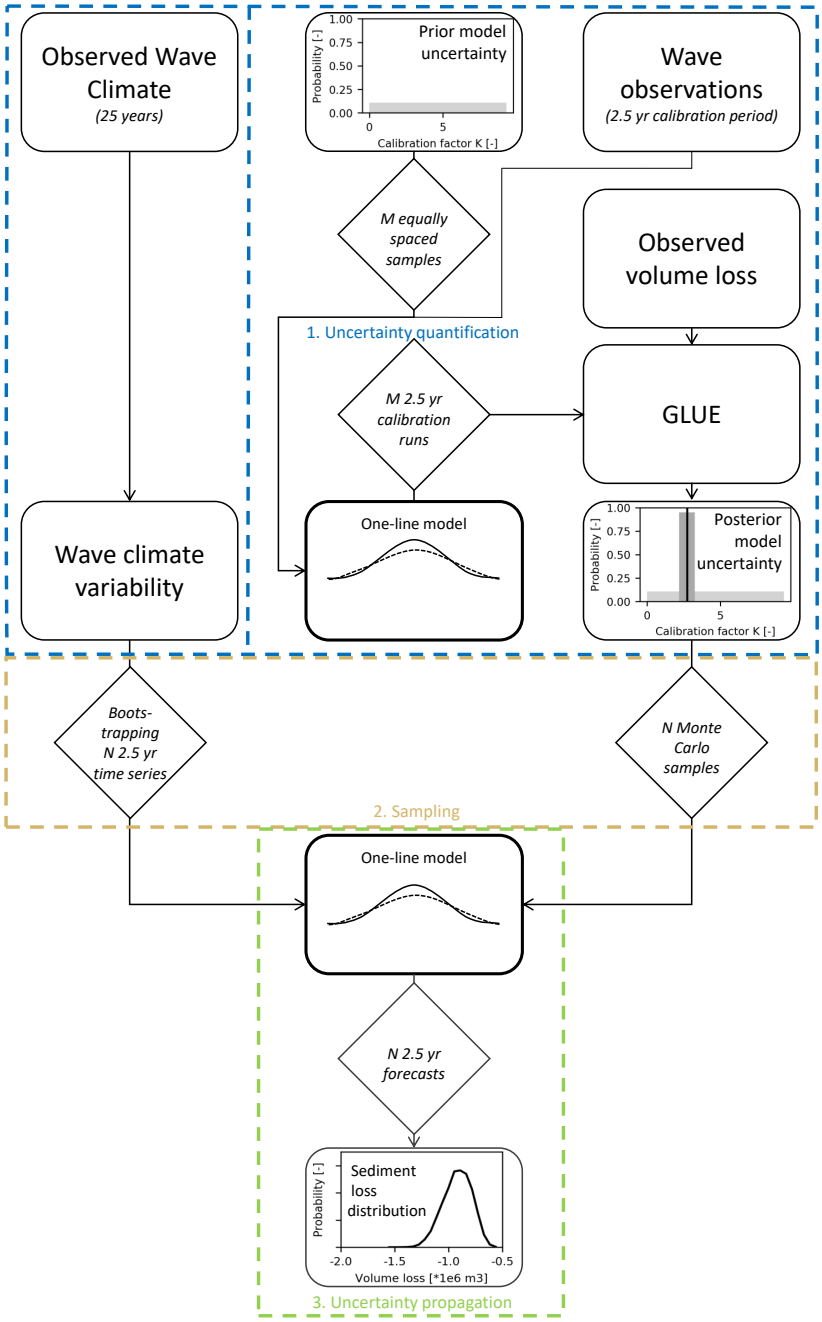

Figure 3.4.: Schematic overview of probabilistic simulation steps: 1) uncertainty quantification, 2) sampling, and 3) uncertainty propagation in a 2.5 y forecast of volume loss.

exposed sites. In addition, Schoonees and Theron (1996) also reveal significant uncertainty in the exact value of K. The re-calibrated formula still shows deviations from observed transports up to a factor 5 and K values 50% higher or lower only have a marginally higher standard error. Exemplifying that K can be regarded a stochastic variable rather than a deterministic one.

3.3.3. Quantification of wave climate variability

To force the one-line model with varying wave time-series that follow local wave statistics, the wave climate variability is quantified using available historical wave time series for a 25 year period. This period precedes both the model calibration period and the forecast period (Fig. 3.3). To maintain seasonal fluctuations and the observed joint probability between H_s, T_p and θ, the time series is separated into monthly sections, providing 25 observations of each month of the year. A bootstrapping procedure (Efron, 1979) is followed to generate a 30-month time series (2.5 years). The forecast time series is built as a sequence of a randomly selected January, followed by a randomly selected February, etc., similar to the method used by Davidson *et al.* (2017). Using this approach, 25^{30} possible sequences can be constructed. Climate fluctuations such as El Nino and the North Atlantic Oscillation are neglected, meaning that observed extreme months can occur in any year and after any other month. In literature several more elegant, sophisticated but also more complex methods are available to generate synthetic wave time series (e.g., Antolínez *et al.*, 2016; Callaghan *et al.*, 2008; Jäger & Nápoles, 2017). Our forecast period is relatively short and the average wave climate component for both the calibration and the forecast period are comparable to the long term average. Indicating that the wave climate behaves ergodic for the period of our interest, supporting the approach followed.

3.3.4. Quantification of model uncertainty

The calibration uncertainty is estimated with GLUE (Beven & Binley, 1992; Ruessink, 2005; Simmons *et al.*, 2017) for the 2.5-year calibration period. GLUE was developed as a calibration method which, in contrast to traditional statistical inference, recognizes that the same result can be obtained with different model settings and calls this 'equifinality'. Equifinality is introduced because the model description of the real world is limited and thus contains errors of some extent. Therefore, a parameter set found by calibration can only be assumed to be a likely estimator. GLUE exploits this reasoning by searching within a large parameter space and appointing a non-zero likelihood to all parameter sets that have a prediction skill higher than a certain threshold.

The first step in GLUE is to decide on a likelihood measure and rejection criterion (Beven & Binley, 1992). In this study the Nash-Sutcliffe skill score (Nash & Sutcliffe, 1970) is used which divides the residual variance between model and

observation by the variance in the observations as:

$$NS = 1 - \frac{\sum_{i=1}^{n} (dV_i - dV_i')^2}{\sum_{i=1}^{n} (dV_i - \bar{dV})^2} \tag{3.3}$$

in which dV and dV′ are the observed and model predicted volume changes in between surveys, respectively, and n is the number of observations. *NS* is the skill score, a score of one represents a perfect model, whereas a negative score means that the mean square error (MSE) is larger than the observed variance.

In this Chapter all calibration parameters that result in a prediction with a score higher than zero are included, accepting predictions with a MSE equal or lower than the observed variance. Demanding a positive skill criterion guarantees that our model is behavioral, capturing the overall trend in the observations.

The second step is to decide which model parameters and input variables are considered uncertain. Here, we illustrate model uncertainty with the calibration parameter K.

The third step of the GLUE method is to decide on a prior distribution for the uncertain parameter(s). In this case we choose a uniform distribution with a wide range, $U(0 - 9.32)$, to minimize subjectivity of the procedure.

Finally, $M = 200$ equally spaced samples of K are drawn from the uniform distribution and used to run the one-line model M times for the 2.5-year calibration period (Fig. 3.4, right side of blue dotted box), varying the K value for each run while forcing the model with the observed waves of this period (orange line in Fig. 3.3). The resulting posterior distribution of K will be a uniform distributed PDF but with a reduced range. From this posterior distribution, $N = 12,000$ samples are drawn with a Monte Carlo procedure, and combined with the N synthetic wave time series of 2.5 years to make a probabilistic forecast with the one-line model.

Note that, by assuming K as the only stochastic variable and calibrating to (uncorrected) field observations we do not limit ourselves to parameter uncertainty only, but we include model inadequacies, numerical uncertainties and observation errors in the posterior distribution of K.

3.3.5. Ranking Uncertainty Sources

The probabilistic procedure results in a distribution of predicted volume change which varies in time. As a first step to achieve the objective of ranking the relative contribution of both uncertainty sources, we perform a local sensitivity analysis in which we compare the magnitude of the variance of the volume change for the wave climate contribution or model uncertainty individually. That means that we pick two locations in the entire range of variables K and w_{br}, the parameter space, at which we compare the variance of ΔV and ΔV_{tot}. We do this for the points with maximum model skill ($Var(Y|K = 2.73)$) and with an average wave climate contribution, $Var(Y|w_{br} = \bar{w}_{br})$ in which $Y = (\Delta V, \Delta V_{tot})$.

The location with maximum model skill and average wave conditions is a point of high interest in the parameter space, but conclusions based on this local comparison are not necessarily true for the entire parameter space. With a global sensitivity analysis (Saltelli *et al.*, 2008) we quantify the fraction of the variance that can be attributed to a certain input variable for each value in the parameter space. This is described by Sobols' indices which rank the contribution of model uncertainty and wave climate variability to the variance of total volume change. In contrast with a local sensitivity analysis, the global sensitivity analysis takes into account the complete range of the inputs, and attempts to apportion the output uncertainty to the uncertainty in the input factors (Jacques *et al.*, 2006), and this can be done for every output time step. As a result the relative importance can be monitored over time.

The first order Sobol' indices describe the importance of each input variable ($X_i = (w_{br}, K)$) as the contribution of this variable to the total variance of output ΔV_{tot}, and can be calculated with:

$$S_i = \frac{Var(E(\Delta V_{tot}|X_i))}{Var(\Delta V_{tot})} \tag{3.4}$$

$S_i = 1$ means that all the variance of output variable ΔV_{tot} can be attributed to input variable X_i, contrarily a $S_i = 0$ means that variability in input variable X_i does not translate to variance of ΔV_{tot}. Because our model (Eq. 3.2) is non-additive, i.e. is a product of two uncertain terms, both uncertainty sources also interact with each other. The interaction term, in case of two uncertain inputs, is given by:

$$S_{12} = \frac{Var(E(\Delta V_{tot}|X_1, X_2))}{\Delta V_{tot}} - S_1 - S_2 \tag{3.5}$$

3.3.6. Probabilistic forecasts

Five sets of computations are examined, one calibration set and four different forecasts (Table 3.1). The calibration set is required to quantify the model uncertainty. The first forecast set includes the quantified distributions of both K and w_{br}. The second forecast includes only the distribution of w_{br} with fixed K as part of the local sensitivity analysis. Similarly, the third forecast includes only the distribution of K with fixed w_{br}. Finally, to examine the effect of a potential dependence between model uncertainty and wave climate variability on the total variance of our prediction, a set of computations is run in which K and w_{br} are correlated with $\rho = 0.5$, according to the findings and procedure of Kroon *et al.* (2019). The marginal distributions of both variables remain equal to the uncorrelated procedure, the only difference is that they are now partially correlated. This means that in case the wave climate component is larger than average in a sample, the probability of a K value larger than average increases.

Description	Calibration	Probabilistic Forecast	Wave climate component only	Model uncertainty only	Correlated Probabilistic Forecast
Run name		$w_{br} + K$	w_{br}	K	$w_{br}\&K$
# of runs	400	12,000[1]	12,000	12,000	12,000
Period	2012/12 - 2015/06	2015/06 - 2018/01	2015/06 - 2018/01	2015/06 - 2018/01	2015/06 - 2018/01
Wave conditions	Observed 2012/12 - 2015/06	Generated time series	Generated time series	$w_{br} = \bar{w}_{br}$	Generated time series
K	$U(0, 9.32)$	$U(2.18, 3.26)^2$	$K = 2.73^2$	$U(2.18, 3.26)^2$	$U(2.18, 3.26)^2$
Corr. coeff. ρ	0	0	0	0	0.5

Table 3.1.: Model settings of different model runs.

3.4. Results

3.4.1. Uncertainty Quantification

As a first step of the probabilistic assessment, the uncertainty in the wave climate component and the model uncertainty were quantified. The empirical distribution of the wave climate component has a mean of 10 $m^2s^{1.5}$ and a standard deviation of 19 $m^2s^{1.5}$ and is highly asymmetrical with a large probability of lower than average wave climate components. The distribution of the wave climate component (w_{br}) of the generated wave time series perfectly resembles the empirical distribution of $w_{br,obs}$ of the 25 years of observed waves (Fig. 3.5). The PDF of all generated years (red dashed line) has no bias and deviates only locally (max. 4%) from the long term average observed distribution of w_{br} (black line). Not only the average generated series compare well to the observed series but also more energetic realizations of the wave climate. To exemplify this we compare observed and generated $w_{br,10}$ (green lines). In which $w_{br,10}$ is defined as the generated series or the (consecutive) 2.5-year observation period of which the average has 10% exceedence probability. Compared to the average values (black line), the generated time series with $w_{br,10}$ (green dashed line) has a lower probability of low values ($w_{br}/\overline{w}_{br} < 0.5$) and a higher probability of w_{br} values above average ($w_{br}/\overline{w}_{br} > 1$). This change in distribution is similar to the observed 2.5-year period (green line) with 10% exceedence. This realization of the wave climate with $w_{br,10}$ is also unbiased and deviations are local and limited to 20%. This means that our approach does not only represent the long-term average wave climate component well but also gives a realistic distribution of w_{br} for energetic realizations of the wave climate.

The model uncertainty has been quantified assessing the skill of the 400 cal-

[1]For the global sensitivity analysis this number of runs is extended to 84,000.
[2]This distribution is the result of the uncertainty quantification procedure, presented in paragraph 3.4.1.

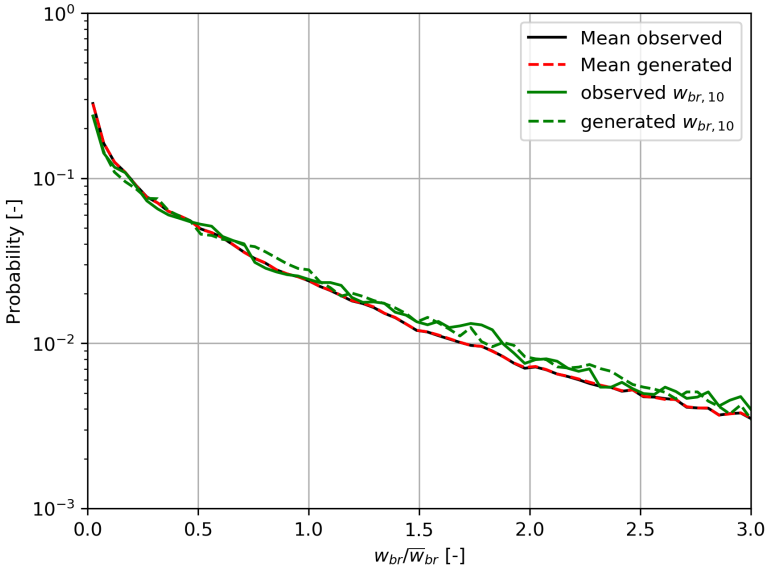

Figure 3.5.: Probability density distribution of normalized wave climate component in Kamphuis formula. Observed (continuous lines) and generated (dashed lines) 2.5-year average (black/red) and 10% exceedence (green).

ibration computations with random $K \sim U(0 - 9.32)$. A comparison of the predicted and observed volume change between consecutive surveys (ΔV) for the calibration period indicates that the one-line model is able to predict the global observed trend, except for some outliers, Fig. 3.6. Next, based on the $NS > 0$ criterion, many of the prior calibration values are rejected, resulting in a significantly reduced posterior range of K to $U(2.18, 3.26)$, Fig. 3.7, while the maximum NS skill is found at $K = 2.73$. The range of K is reduced on both sides of the prior distribution, indicating that the range of the prior was chosen properly.

3.4.2. Uncertainty propagation

This subsection presents the results of the probabilistic forecasts in which the distributions of K and w_{br}, as derived in the previous section, are propagated through the one-line model to come to a distribution of volume change. Four different forecasts are examined (Table 3.1). Following the calibration of the model, the adopted model settings are $K \sim U(2.18-2.36)$ and w_{br} similar to the empirical distribution of $w_{br,obs}$.

The probabilistic forecast ($w_{br}+K$), predicts a loss of almost 1.000.000 m^3 in 2.5 years with a standard deviation of 15% (Fig. 3.8b). The observed volume change between consecutive surveys shows a clear summer/winter pattern that is reproduced by the probabilistic forecast (Fig. 3.8a). The width of the confidence inter-

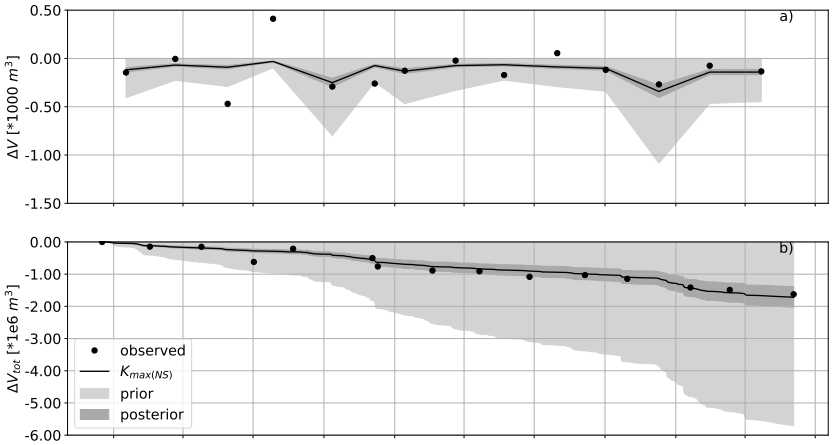

Figure 3.6.: Predicted and observed volume change for GLUE calibration procedure, a) between consecutive surveys and b) total volume change since June 2015. The prior distribution (light grey area), the posterior distribution of all runs with $NS > 0$ (dark grey area), and the run with the highest skill score (black line) compared to observed volume change.

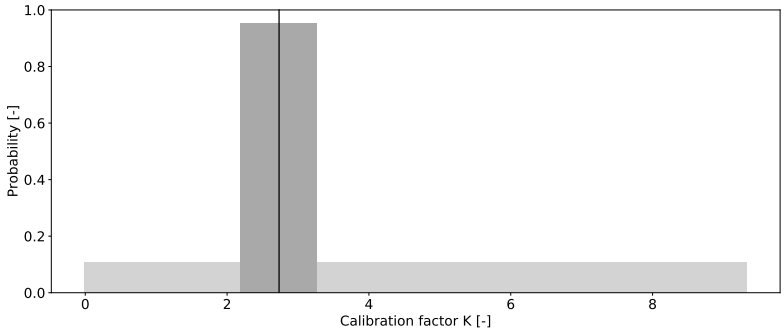

Figure 3.7.: Probability density distribution of model calibration factor K, prior to the GLUE calibration procedure (light grey) and posterior (dark grey). The black line indicates $K = 2.73$, the value with the highest *NS* skill score.

vals, e.g., the distance between the 5% and the 95% percentile level (Fig. 3.8a, light grey shade), is a measure for the variance of the distribution. This forecasted variance is higher in winter than in summer. This is an effect of the monthly bootstrapping procedure, which forces the model to have a smaller variance in summer and a larger variance in winter, similar to the observed wave climate. The model bias is negligible, but the variance is much lower than observed. Only

50% of observations fall within the 90% confidence interval, whereas this should be approximately 90%. Similarly only 8% of observed volume changes fall within the 50% confidence interval and no observations fall within the 10% confidence interval (Table 3.2).

On the other hand, the total volume change is predicted very well by the model (Fig. 3.8b). The model shows no bias in predicting the total volume change, and the variance of the total volume change is more accurately represented. Hence, 85% of the observations fall within the 90% confidence interval which is very close to the expected 90%. Similarly, 70% and 15% of the observed volume changes fall within the 50 and 10% confidence intervals, respectively (Table 3.2). The total volume change and the corresponding confidence intervals are predicted remarkably well considering the small number of observations.

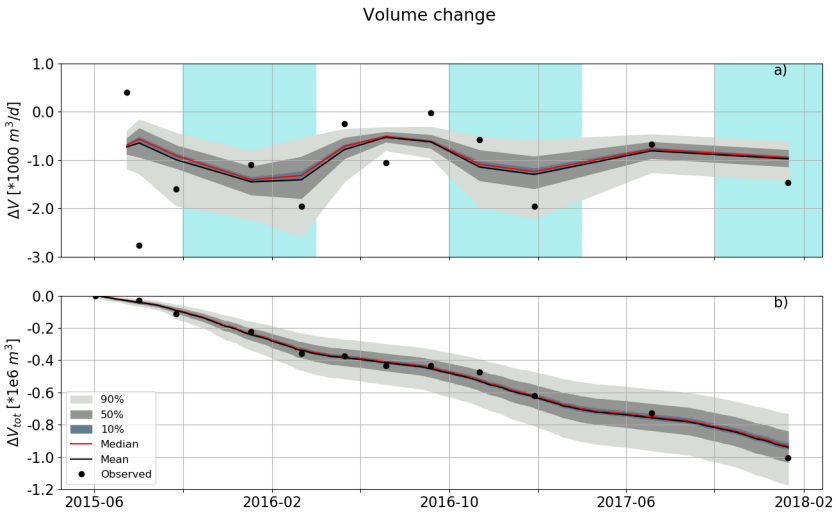

Figure 3.8.: Predicted and observed volume change a) between consecutive surveys and b) since June 2015. The mean (red line), median (black line), and the 90, 50 and 10% confidence interval (light gray, dark gray and blue shaded areas) of the probabilistic forecasts are presented together with the observed volume change (black dots). Winter months October to April are indicated with the yellow background.

Looking at the effects of K and w_{br} individually, we see that the conditional variance of the volume change between consecutive surveys is significantly lower when conditioned on the average wave climate component ($Var(\Delta V|w_{br} = \bar{w}_{br})$), than conditioned on the model calibration parameter with the highest skill ($Var(\Delta V|K = 2.73)$) (Fig. 3.9b and f). However, the variance of the total volume change conditioned on average wave climate component, $V(\Delta V_{tot}|w_{br} = \bar{w}_{br})$, is increasing over time, whereas $V(\Delta V_{tot}|K = 2.73)$ increases initially but becomes

stable over time (Fig. 3.9d and h). As a result, the variance of total volume change conditioned on $K = 2.73$ is ,after 2.5 years (Fig. 10d), approximately equal to the variance of the total volume change conditioned on the average wave climate component (Fig. 10h), meaning that the variance of total volume change is equally sensitive to both inputs at these two locations in the parameter space.

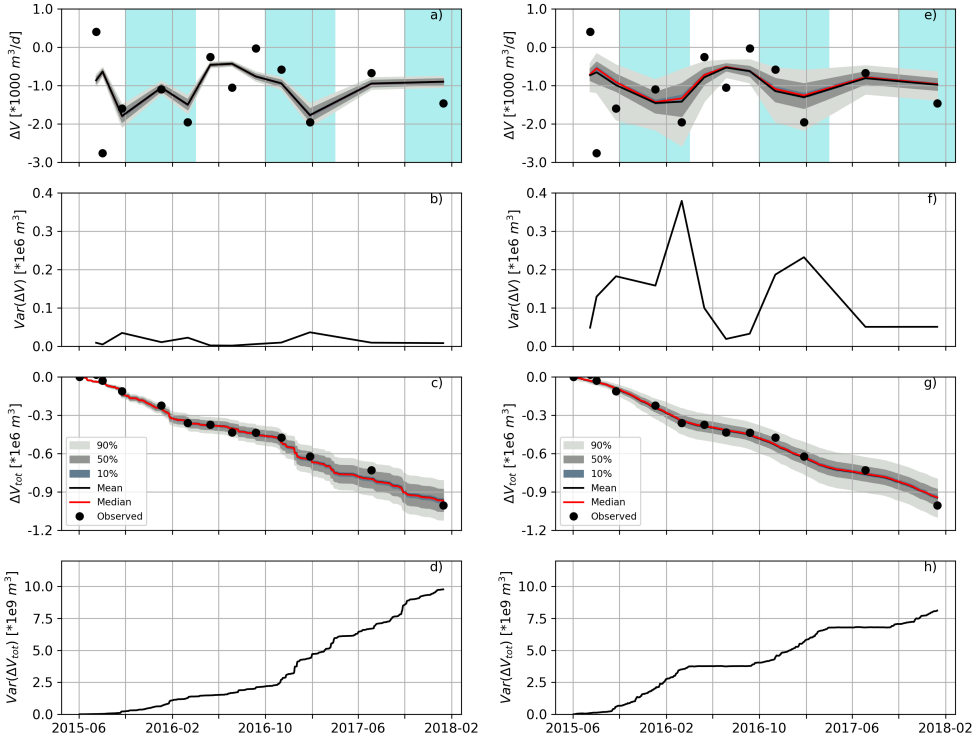

Figure 3.9.: Comparison of predictions with model uncertainty (a-d) and wave climate variability (e-h) only. Predicted and observed volume change between consecutive surveys (a/e), variance of volume change between consecutive surveys (b/f), total volume change since June 2015 (c/g) and variance of total volume change (d/h) . The mean (red line), median (black line), and the 90, 50 and 10% confidence interval (light gray, dark gray and blue shaded areas) of the probabilistic forecasts are presented together with the observed volume change (black dots). Winter months October to April are indicated with the yellow background.

Using Sobol's sensitivity index to quantify this change of relative importance over time globally (Fig. 3.10), we see that the contribution of K to the total variance of ΔV_{tot} is indeed only 20% at the start of the simulation. However, by the

end of the simulation this has increased significantly and amounts over 50% of the total variance. w_{br} on the other hand constitutes 60% of the total variance at the start of the simulation but less than 40% after 2.5 years, due to the increasing contribution of model uncertainty to the total variance. In addition, both terms interact explaining another 15-20% of the variance. So, in the case of the sand engine, assessing the effect of wave climate variability only would give a significantly overconfident estimate which neglects more than half the variance.

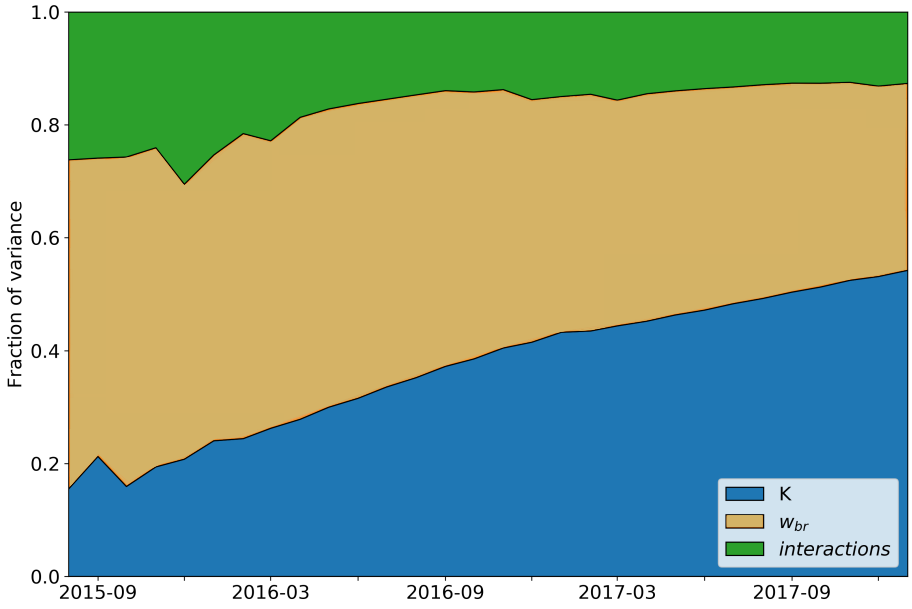

Figure 3.10.: Fraction of the total variance of ΔV_{tot}, of model uncertainty K (blue), wave climate component w_{br} (orange) and interactions between both uncertainty sources (green).

Sobol's indices cannot be determined for correlated uncertainty sources. Therefore, the effect of a potential correlation between K and w_{br} is assessed by comparing the total variance of the uncorrelated runs (w_{br} and $w_{br} + K$) with the total variance as predicted by the correlated runs ($w_{br}\&K$). Positively correlated uncertainty sources increase the variance of both ΔV and ΔV_{tot}, Fig. 3.11. Neglecting this correlation results in an additional underestimation of the variance by 40% after 2.5 years. So, not attributing for model uncertainty would at least underestimate the variance by 50% in a 2.5-year forecast, but in case of a positive correlation this will be significantly more.

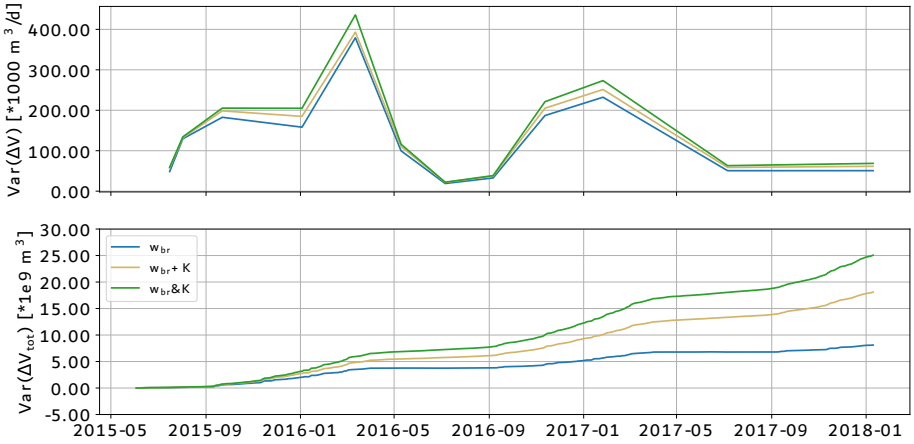

Figure 3.11.: Variance of predicted volume change against time for ΔV_{tot}.

Confidence interval	ΔV	ΔV_{tot}
90 %	0.50	0.85
50 %	0.08	0.69
10 %	0.0	0.15

Table 3.2.: Fraction of points within confidence interval.

3.5. Discussion

The probabilistic predictions show that the uncertainty in the volume change at the sand engine nourishment is considerable. We expect a loss of almost 1.000.000 m^3 in 2.5 years with a standard deviation of 15% when including both wave climate variability and model uncertainty. Model uncertainty explains over 50% of the total variance after 2.5 years. These results stress that, for the assessment of large scale nourishments it is not only important to look at variations in wave forcing but also to account for uncertainty in the model(s) used. This conclusion is based on an assessment of a large scale nourishment, yet it is likely that these results are applicable to any sandy solution in the coastal zone.

Evidently, not in all cases the contribution of model uncertainty will be over 50%. For instance, using a more sophisticated model or applying a sandy solution in an environment with a very high variation in wave conditions could reduce the relative importance of model uncertainty. Likewise, predicting a more event driven parameter or process, such as depth of closure, storm retreat or spit breaching, could increase the relative importance of wave climate variability. Also, after the design has been made and a sandy solution has been implemented, the relative importance of model uncertainty in the prediction can in theory be reduced by updating the model uncertainty with new observations once they come available (Vitousek *et al.*, 2017).

Contrarily, the relative importance of model uncertainty will likely increase for smaller nourishments with a less pronounced signal, or in environments with a very narrow distribution in wave forcing (e.g., swell dominated environment). Thus, it is unlikely that in any case model uncertainty (beyond a monthly time scale) can be considered negligible beforehand, without further analysis.

Looking at a slightly longer time scale, the decreasing relative importance of wave climate variability justifies the established use of wave climate reduction in morphological modeling (e.g., Benedet *et al.*, 2016). This is also in line with the findings of Luijendijk *et al.* (2019), who show that simulations with a reduced wave climate and with brute force time series give a similar prediction of bulk morphometrics such as total volume change after 5 years at the Sand Engine.

If we extend the time horizon further, other factors, such as sea level rise, can become important contributors to uncertainty. Le Cozannet *et al.* (2019) use a global sensitivity analysis to show that coastline recession is initially dominated by seasonal, inter-annual and decadal variations, but that the relative importance of model uncertainty increases quickly. Variations in sea level rise scenarios only start to gain importance after half a decade. Although assessing morphological effects of sea level rise, their conclusion is alike: model uncertainty cannot be neglected.

Callaghan *et al.* (2013) predict beach erosion, a more event driven process, with three different models. The envelope of their multi-model ensemble, is 70-150 % wider than the 95% confidence interval of each model individually. Therewith indicating that in their case, model uncertainties contribute significantly to the prediction uncertainty. For comparison, the 95% confidence interval width of our prediction increases by 70% if we include model uncertainty in the analysis.

The underestimation of the observed variance of monthly volume changes (e.g., Fig. 3.8a) indicates that residual uncertainty remains. Our application of the GLUE method with one free variable, focused on deriving a realistic estimate of model uncertainty, but one can possibly give an improved representation of the observed variance and exploit the full strength of GLUE by assuming more variables to be stochastic. This could be done within the model (e.g., the powers in the Kamphuis formula or the median grain size) but also by including observation uncertainty or adding more processes in the model. So, a straightforward next step is to differentiate between observation and model uncertainty and applying a more advanced model.

In this chapter, we concentrated on determining the importance of intrinsic versus epistemic uncertainty by distinguishing between wave climate variability and model uncertainty. We found that assessing wave climate uncertainty only, can result in significantly overconfident predictions. Still, in our analysis residual intrinsic and epistemic uncertainty remains, meaning that we might still present an overconfident prediction. Nevertheless, these results clearly show how important it is to be aware of the uncertainties in our models and to be cautious with presenting (un)confidence intervals.

3.6. Conclusion

This Chapter includes both intrinsic and epistemic uncertainty in a probabilistic framework, to investigate the relative importance of these uncertainties in the evolution of a sandy solution. To this end, we assess a large scale nourishment case with a one-line model in a probabilistic framework. In this framework, transport and volume loss are considered to be a function of random wave forcing (intrinsic uncertainty) and calibration settings (epistemic uncertainty). The variance of both stochastic variables are based on observations using the Sand Engine nourishment.

We show that confidence interval width and variance of predicted volume loss increase when allowing for model uncertainty. The confidence interval width and variance increase further (40%) if we not only recognize uncertainty in our model but also include a correlation (of $\rho = 0.5$) between model parameter settings and wave forcing. For the Sand Engine nourishment examined here, the contribution of model uncertainty to the variance of total volume loss is of the same order of magnitude as the contribution of wave climate variability after a 2.5-year simulation period, indicating that accounting for wave climate variability only will produce significant overconfidence in the results. Nevertheless, on a monthly time scale the fraction of variance attributed to wave climate variability is three times larger than that of model uncertainty, thus reducing the importance of model uncertainty in predicting initial nourishment development.

For multi-year time scales, model uncertainty will become the dominant contribution: more wave energy in one year is compensated by less wave energy in another, whereas model uncertainty is a cumulative effect that grows with each time step. Naturally, the relative importance of model uncertainty over wave climate variability depends on the complexity and skill of the model. In general, probabilistic frameworks rely on less complex models to reduce computation time, thereby possibly increasing the relevance of model uncertainty assessment within the framework.

These findings imply that for coastal modelling a dual approach should be considered, evaluating both epistemic and intrinsic uncertainties. Especially when forecasting large scale projects, with simplified models on a multi-year time scale, the uncertainty in model settings may be the principal source of uncertainty.

4

Uncertainty in predicting coastal state indicators with a coastal area model

Abstract

Coastal engineering projects following Building with Nature principles often serve multiple purposes, including increasing safety against flooding, ecology, commercial activities, and recreation. As a result, predictive models that describe these interventions' current and future states must be able to forecast various indicators. Coastal area models that compute bed level changes on a grid in two horizontal dimensions are suited to predict changes in such indicators. However, coastal area modeling comes at the cost of high computational times and includes many free model parameters. This makes exploring a substantial portion of the parameter space difficult and introduces uncertainty in predicting these coastal state indicators (CSIs). To quantify uncertainty in predicted coastal state indicator values that follow from the uncertainty in the model parameter values, the multi-dimensional parameter space of a Delft3D model is explored. We use the Sand Engine mega nourishment as a test case to investigate how parameter uncertainty develops in time and space and influences the predictions for different CSIs. The free model parameters are reduced to five key parameters using expert judgment and the Elementary-Effect method. The Generalized Likelihood Uncertainty Estimation (GLUE) method is used to arrive at an observation-based likelihood distribution of the key model parameters and the CSIs. Uncertainty in these five key input parameters translates into significant uncertainty in predicted CSI values. Volume changes for sediment budget analyses can vary by

This chapter is in preparation to be submitted to Scientific Reports.

$75 - 85\%$ of predicted changes, predicted coastline position by $\pm$ 100 m, and bed level change confidence up to 5 m (90% confidence values). The suspended sediment transport scaling (f_{sus}), the breaker index (γ), and the grain size (d_{50}) contribute the most to the overall uncertainty in the predictions, but the importance of the five parameters varies per CSI. The parameter uncertainty creates the widest confidence intervals at locations and moments when the changes for the CSIs are most significant. Outcomes can be substantially different across the different parameter sets with high likelihood. Additionally, the model's sensitivity can vary significantly depending on the CSI of interest. Because of these sensitivities, the parameter values that yielded the best results may not be transferable to other projects, and there may be no single 'best' generic value for each parameter. Our results underline the importance of a good model calibration practice. Herein, the calibration area and parameter(s) of choice should be consistent with the CSIs to predict, as they can significantly impact the outcome of the (manual) calibration procedure.

4.1. Introduction

Present coastal management views often favor more soft, nature-inclusive, and adaptive measures over traditional hard protection structures (de Vriend *et al.*, 2015; Sutton-Grier *et al.*, 2015). Coastal engineering projects that follow these management views often serve multiple purposes, including increasing safety against flooding, ecology, commercial activities, and recreation (e.g., Bridges *et al.*, 2018; Palinkas *et al.*, 2022; Stive *et al.*, 2013). Safety against flooding, ecology, and recreation place different and occasionally conflicting demands on a project's initial and future state (de Schipper *et al.*, 2021). As a result, the definition of effectiveness can vary depending on the project's goals (G. Liu *et al.*, 2019; van Koningsveld *et al.*, 2005). For example, metrics based on the volume of sand may be used to assess safety against flooding. Similarly, ecology may require a specific habitat area and recreation a minimum beach width (Sánchez-Arcilla *et al.*, 2011). These various metrics are also referred to as coastal state indicators (CSIs) and defined by Davidson *et al.* (2007) as "A reduced set of issue-related parameters that can simply, adequately and quantitatively describe the dynamic-state and evolutionary trends of a coastal system".

Process-based coastal area models have the potential to provide comprehensive information on various CSIs at multiple spatiotemporal scales (Luijendijk *et al.*, 2019). Process-based coastal area models are capable of reproducing complex coastal morphodynamics (e.g., Lesser, 2009; Roelvink *et al.*, 2009; Warner *et al.*, 2010), yet their predictions may contain considerable uncertainty (Ranasinghe, 2020). Nonetheless, these models are frequently used as engineering tools when decision-making calls for quantitative assessment of coastal interventions (e.g., Kroon *et al.*, 2016; Perk *et al.*, 2019; Strauss *et al.*, 2020; van der Spek *et al.*, 2020; van der Werf *et al.*, 2019).

Uncertainty in process-based models is in part intrinsic, e.g., caused by variations in environmental conditions such as variations in sediment supply by rivers

or wave forcing (Baart, 2013; Baquerizo & Losada, 2008; Callaghan *et al.*, 2013; Ranasinghe *et al.*, 2012; Ruggiero *et al.*, 2010). In part, this uncertainty is epistemic (Kiureghian & Ditlevsen, 2008), caused by uncertainties in the approach or model. Process-based coastal area models approximate natural processes using mathematical equations that include free model parameters. In theory, a greater number of processes will result in a better representation of the system and thus, more accurate predictions and increased model transportability. However, with increasing model complexity, the number of free model parameters increases, as each new process can easily introduce 1-10 additional parameters. As such, parameter uncertainty is an important component of epistemic uncertainty in a process-based model.

Free model parameters may represent either calibration coefficients or physical quantities. Calibration coefficients are used to calibrate and adjust the model for specific applications and often lack a physical basis, making it difficult to estimate their values (Ruessink, 2005). Parameters representing physical quantities (e.g., grain size, bed friction) are often site-specific, space and time-varying and therefore challenging to measure, resulting in uncertain estimations. In engineering practice, these parameter values are usually chosen in a manual calibration process (e.g., Harley *et al.*, 2016; Luijendijk *et al.*, 2017a). In which free model parameters are adjusted by hand, based on the outcome of the previous run, so that the outcomes of the model compare best with observations or expectations. Attention to parameter uncertainty introduced by using models with (many) free parameters has recently increased (Kroon *et al.*, 2020; Montaño *et al.*, 2020; Ruessink, 2005; Simmons *et al.*, 2017; Vitousek *et al.*, 2021; Wilson, 2023). For example, Ruessink (2005) found that the influence of parameter uncertainty is strongest near the sandbar crests of the cross-shore profile but rapidly decreased in other areas. Kroon *et al.* (2020) show that model uncertainty even becomes dominant for multi-year time scales compared to uncertainty caused by variations in wave forcing. Simmons *et al.* (2017) demonstrate that quantifying parameter uncertainty leads to significant performance improvements and allows the modeler to communicate the expected uncertainty.

Model computation times can easily exceed days if not weeks (Luijendijk *et al.*, 2019; Ranasinghe, 2020). A manual calibration process makes exploring a significant portion of the parameter space nearly impossible. This is especially true when the parameters are interdependent or reciprocal (e.g., Ruessink, 2005), resulting in local optima of parameter settings. The consequence is that the estimation of parameter values relies heavily on expert judgment and/or default values provided with the model. This subjective and time-consuming process provides little information on whether *the* optimal parameter set has been found or even exists. Especially for models with many parameters, the latter is highly unlikely (Oreskes *et al.*, 1994; Ruessink, 2005), leaving the predictive value of the model open to question (Oreskes *et al.*, 1994) and potentially introducing significant uncertainty in the prediction of CSIs.

So far, for process-based multi-dimensional models the emphasis has been on determining optimal parameter settings (Bae *et al.*, 2022; Briere *et al.*, 2011),

efficient propagation of (parameter) uncertainty (Berends *et al.*, 2019; Hendrickx *et al.*, 2023) or sensitivity analysis with small ensembles (van der Wegen & Jaffe, 2013). For cross-shore morphodynamic predictions Briere *et al.* (2011) propose an efficient calibration tool to find optimal parameter settings in a cross-shore model with two dimensions (2DV). Their approach formally optimizes parameter settings, as such, not the entire parameter space is inventoried, therefore it does not quantify parameter uncertainty itself. Recently, Bae *et al.* (2022) used a Monte Carlo approach in combination with a coastal area model to select parameter settings that optimally reproduce observed bed levels. Although their data set probably provides information on the uncertainty in the model parameters and bed-level predictions, they do not provide any detail on this aspect. Furthermore, van der Wegen and Jaffe (2013) generate small ensembles around manually found calibration settings. Without indication of the probability of the outcomes of the ensemble runs, this provides only a sensitivity estimate and no uncertainty estimate. These efforts demonstrate that so far, little is known about the uncertainties in coastal area models, particularly how these uncertainties affect various coastal state indicators.

Therefore, we aim to explore the multi-dimensional parameter space to quantify uncertainty of coastal area models in predicting various coastal state indicators. We present the bandwidth around modeled coastal state indicators based on more than 1000 predictions with a process-based model, demonstrating how uncertainty is generated in time and space and how input parameter values affect a variety of coastal state indicators.

4.2. Methods

We use the Sand Engine mega nourishment as a test-case to investigate how parameter uncertainty influences coastal area predictions. The Sand Engine is a well-monitored nourishment (de Schipper *et al.*, 2016; Roest *et al.*, 2021) for which high-resolution spatiotemporal observation data is available (Roest *et al.*, 2017). The data clearly shows a redistribution of sediments in the alongshore direction, which can be reproduced well with both reduced complexity models (Arriaga *et al.*, 2017; Kroon *et al.*, 2020; Tonnon *et al.*, 2018) and process-based models (Luijendijk *et al.*, 2017a; Luijendijk *et al.*, 2019; Tonnon *et al.*, 2018). For this case study, we carry out 14-month morphological prediction using the Delft3D schematization of Luijendijk *et al.* (2017a) and Luijendijk *et al.* (2019). We run the model over 1000 times with varying values of the five most influential free model parameters. These five free model parameters are selected based on literature, expert solicitation, and sensitivity analysis. With the Generalized Uncertainty Estimation (GLUE) method, we make an observation-based estimate of the parameter-induced uncertainty in the predictions.

Figure 4.1.: Aerial photos of the SE, taken from the North, in a) July 2011 (shortly after construction) and b) July 2012 (after the first year). Source: Rijkswaterstaat and van Houdt (2012)

4.2.1. Sand Engine Nourishment

The Sand Engine (SE) is a mega-nourishment constructed in 2011 (Fig. 4.1). The SE intends to feed the adjacent coastline over 20 years, as the sand is gradually redistributed through natural processes (Stive *et al.*, 2013). The nourishment was designed as a large hook-shaped sand peninsula flanked by two shore-face nourishments. The peninsula covered 2.4 km in alongshore and around 1 km in cross-shore direction. The total added nourishment volume was approximately 21.5 million m^3, divided over the peninsula ($\pm$ 17 million m^3) and shore-face nourishments ($\pm$ 4.5 million m^3). During the design phase, many different stakeholders were involved in combining engineering aspects with environmental, ecological, and social considerations. Consequently, the shape of the peninsula was inspired by the potential for natural and recreational development (Stive *et al.*, 2013) and a sheltered tidal lagoon was included to create a new habitat. The resulting design exemplifies the different purposes of the project and the need for predictions of different CSIs to indicate the expected success of the project.

The evolution of the SE has been monitored since the construction was completed in August 2011. During the first 17 months, bathymetry surveys were conducted near-monthly (de Schipper *et al.*, 2016). The bathymetric surveys cover an area of 4.7 by 1.6 km and are presented in this Chapter in a local, shore orthogonal coordinate system (Fig. 4.2). For that, the survey data is rotated by approximately 311 °N, the shore normal of the coastline prior to the SE implementation. As of 2016, the outer perimeter of the peninsula has regressed by up to 300 m, while the adjacent coast has progressed by up to 200 m. The initially asymmetric shape was reworked during the first 18 months to an almost symmetric shape along the coast (Fig. 4.2b). A sand spit developed at the peninsula's northern edge, squeezing the lagoon entrance but maintaining an active tidal channel. Cumulative volume changes for three areas (South section, peninsula, and North section) show that 72% of the sand volume loss around the peninsula accreted

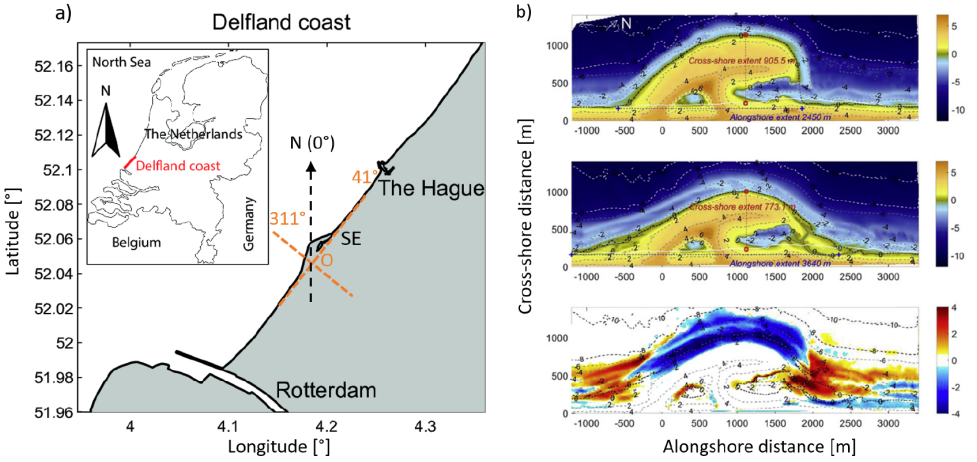

Figure 4.2.: a) Location of project site in the Netherlands and definition of local shore orthogonal coordinate system, and b) bed levels in m+NAP (NAP is the Dutch reference level, roughly equal to mean sea level) and morphological changes in the first 17 months at the Sand Engine (figure from de Schipper *et al.* (2016)).

in adjacent sections (± 1.65 million m^3, over the first 17 months), confirming the natural redistribution of the nourishment (de Schipper *et al.*, 2016). A larger portion of the erosion on the peninsula was compensated for by accretion in the North section (± 60% of the observed accretion). Observed morphological changes in the area were strongest in the first six months (including the storm season of December and January 2011/12), drastically reducing the curvature and cross-shore beach slope (de Schipper *et al.*, 2016). After this initial response phase, the morphological changes became slower and more nuanced. These morphological changes at the SE are strongly correlated to the incoming wave climate, i.e., months with high average wave heights resulted in more significant changes and vice versa (de Schipper *et al.*, 2016). This suggests that the waves, specifically the wave-driven alongshore current, form the dominant natural process governing sediment transport in this area. Most high-energy wave events since construction came from southern to western directions (de Schipper *et al.*, 2016), leading to a net northward directed alongshore current.

4.2.2. Delft3D model

The Delft3D model schematization of Luijendijk *et al.* (2019) computes sediment transport and corresponding bed level changes resulting from tides and waves. This model was first set up in Luijendijk *et al.* (2017a) but later adjusted for model efficiency in Luijendijk *et al.* (2019).

The model is used in 2DH mode and uses a curvilinear grid for the hydro-

dynamic and morphological computations (Fig. 4.3). The grid resolution varies from 35 m to 500 m and is highest in the SE area, decreasing with distance from there. The initial bathymetry in the SE area is based on the first measurements taken after construction on August 2^{nd}, 2011. The bathymetry in the remainder of the domain (beyond the 10 m depth contour) is based on surveys of the Ministry of Public Works Rijkswaterstaat (Rijkswaterstaat, 2020a).

Two additional nested grids are applied to propagate the offshore wave conditions into the hydrodynamic domain (Fig. 4.3). The largest grid is forced by a time series of wave height, period, and direction from two offshore locations (Europlatform and IJmuiden) about 50 km from the site, combined with a uniform wind based on the measured time series at Lichteiland Goeree (4.3).

Tidal boundary conditions originate from nesting in a large-scale model for the Dutch Continental Shelf. Finally, observed surge levels and wind speeds at Hoek van Holland are used to include meteorological influences in the model.

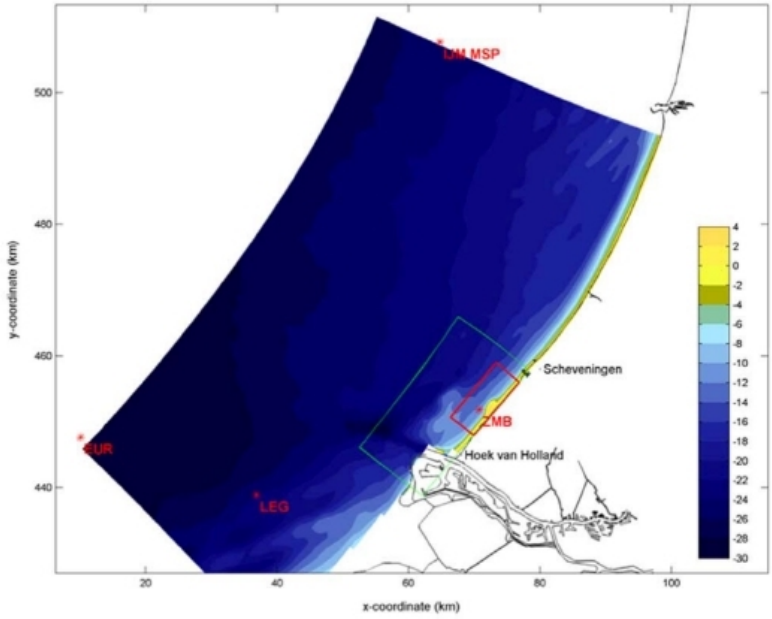

Figure 4.3.: Model domain showing the nested wave grids (entire domain and green box) and the hydrodynamic grid (red box). Measurement stations for boundary conditions are indicated with a red asterisk: Europlatform (EUR, waves), IJmuiden (IJM MSP, waves), and Lichteiland Goeree (LEG, wind). Color scale indicates local water depth in m+NAP. Figure based on Luijendijk *et al.* (2017a)

The model accelerates the morphological change by a morphological factor (Ranasinghe *et al.*, 2011) of three compared to the hydraulic time step. All time steps with waves at Europlatform lower than 1 m or directed away from the coast

are filtered from the series for computational efficiency, as these do not lead to significant morphological changes (Luijendijk *et al.*, 2019). Finally, the filtered wave series are compressed by a factor three to match the morphological acceleration.

4.2.3. Free model parameters

Delft3D contains over 50 model parameters, which, in theory, could all be used for model calibration and contribute to the models' uncertainty. However, this is currently not feasible as one 14-month computation takes five days on a Haswell node (2.6 GHz Intel Xeon E5-2690 v3, 64GB, 1.078 Pflop/s) of the Dutch National Supercomputer. Varying the more than 50 free model parameters of Delft3D with a resolution of four (per free model parameter) would cost $6.34e30$ days of computation time ($5 * 4^{50}$), resulting in an impossible task. The computational budget for this study allows $\pm$1000 model runs for the GLUE analysis. As a balanced choice, we want to focus on the five most influential parameters. With a resolution of four, this results in ($4^5 =$) 1024 simulations.

The first step is to reduce the number of model free parameters. We start from a list of over 30 model tuning parameters often used in literature (e.g., Briere *et al.*, 2011; Grunnet *et al.*, 2004; Hopkins *et al.*, 2018; Lesser, 2009; Luijendijk *et al.*, 2017a; van der Wegen & Jaffe, 2013). Next, in expert solicitation, the 30 parameters are reduced to 16 and physical realistic limits are set for these parameters (Table 4.1). These 16 parameters are categorized into four classes (hydraulic, wave, sediment, and morphology) according to their implementation in the model. For a detailed description of the implementation of each parameter, the reader is referred to the Delft3D-FLOW user manual (Deltares, 2019).

The hydraulic parameters influence hydrodynamic processes, such as flow velocities and shear stresses. Here, three parameters are considered. The bottom roughness is specified through the Chézy coefficient, C. The coefficient can be specified in longitudinal and transverse directions but is assumed to be uniform over the computational domain. The default value is 65 $\sqrt{m}/s$ and the applied range is set to 50–80 $\sqrt{m}/s$, based on expert judgment. Next, the horizontal viscosity and diffusivity are required for the turbulence model, ν_h and D_h. These are sums of a constant part and a user-defined background value (ν_h^{back} and D_h^{back}, respectively). These background values are varied in this study. Their default values are zero, but results of Luijendijk *et al.* (2017a) have shown that non-zero values lead to better results. Therefore, the applied range has been set to 0.1-1 m^2/s for both.

The wave parameters influence the propagation and characteristics of the incoming waves. Several parameters can be specified within the WAVE module (SWAN) and the roller model in the FLOW module. Here, we limit the work to parameters in the FLOW module of Delft3D by examining four parameters of the roller model.

Delft3D applies the breaker index γ to model depth-induced breaking, which sets the critical wave height to water depth ratio H_s/h, above which waves start

to break. As the hydrodynamic time step is smaller than the wave update time step, the water depth may reduce in between wave time steps. Therefore, to ensure that the wave height to depth ratio is not exceeded, a maximum allowed value γ_{max} is applied, which enforces wave breaking on the hydrodynamic time-step level. The default value of γ is 0.55 (Deltares, 2019), but higher values have also been used. The range has been set to 0.55–0.8 based on expert judgment. The same range is applied for γ_{max} due to its physical similarity to γ.

We consider two additional wave parameters that affect the wave breaking: the wave energy dissipation coefficient, α_{rol} and the mean slope under the roller, β_{rol}. α_{rol} is a calibration coefficient of $O(1)$ that directly scales the energy dissipated by a breaking wave (Reniers *et al.*, 2004; Roelvink, 1993). Most studies adhere to the default value of 1, while Briere *et al.* (2011) examined a range from 0 to 2. β_{rol} largely determines the energy transfer to and from the roller (default 0.1). Zero values for α_{rol} and β_{rol} result in no energy dissipation and initial test simulations confirmed that zero values often lead to an unstable model. Therefore, the ranges are set to 0.1–2 for α_{rol} and 0.01–0.2 for β_{rol}.

The sediment parameters directly influence the sediment transport computed by the model. This is the largest group with six evaluated parameters. First, several multiplication factors are considered that scale the suspended and bed load sediment transport separately for currents (f_{sus} and f_{bed}) and wave contributions ($f_{sus,w}$ and $f_{bed,w}$). The computed sediment transports are multiplied with these factors; hence, their default values are equal to 1. Most studies use similar values for bedload and suspended load parameters (i.e., $f_{sus} = f_{bed}$, $f_{bed,w} = f_{sus,w}$) (e.g., Hopkins *et al.*, 2018; Luijendijk *et al.*, 2017a) but occasionally these are varied independently (e.g., Grunnet *et al.*, 2004). Predicted sediment transport is often over-estimated and high parameter values (i.e., factors larger than 1) may result in an unstable model. Therefore, the range for the four scaling factors has been set at 0.1-1 (a value of 0 is not suitable, as it would cancel sediment transport altogether).

The grain size of the bed material is represented by the median grain diameter, d_{50}. The native grain size d_{50} on the Delfland coast is estimated at $\pm$ 250 μm (Wijnberg, 2002). An analysis during construction of the SE showed an average d_{50} of 281 μm de Schipper *et al.* (2016). Huisman *et al.* (2016) report significant spatial variation in d_{50} around the SE, specifically coarsening of the sediment in front of the peninsula with +90 to +150 μm and fining of the sediment in adjacent sections by up to 50 μm. Considering this coarsening and fining with time, the applied range has been set to 200–350 μm. In the model, the d_{50} is assumed uniform over the model domain because the effect of spatial variation of grain size on the morphological development is considered of secondary order (Huisman *et al.*, 2019).

In addition to the grain size of the bed, the representative grain size of suspended sediment is determined by the factor fac_{dss} multiplied by the d_{50} of the bed. The default value is 1 (i.e., the suspended grain size is equal to that of the seabed). It's a reasonable assumption that the suspended grain size is not larger than the bed grain size, as this would imply that the largest grains are mobilized by the

current while smaller grains stay near the bed. According to van Rijn (1993), the grain size of suspended sediment is in the range of 60 to 100 % of the grain size of the bed material. Therefore, the applied range is set to 0.6–1.

Morphology parameters specifically address how sediment fluxes are coupled to the bed elevation changes. Three parameters are considered. The first two scale the effect of stream-wise (α_{bs}, default 1) and transverse (α_{bn}, default 1.5) bed level gradients on the bed load transport. To model bar dynamics, realistic values of α_{bs} range between 1 and 5 (Briere *et al.*, 2011). In river engineering, which often includes steep banks, much higher levels are used (especially for α_{bn}, (e.g., Baar *et al.*, 2019)), but for coastal purposes, the parameters are generally considered less important. The range has been set to 1–25 for both parameters to include the possibility of larger values in the SE model.

The third evaluated morphology parameter is specifically aimed at the land-water interface. The so-called dry cell erosion parameter enables the erosion of dry cells (cells with a water depth below a certain threshold) by distributing (part of) the computed erosion for a wet cell over adjacent dry cells higher up the profile. The dry cell erosion factor θ_{sd} specifies the fraction transferred to adjacent dry cells. According to Luijendijk *et al.* (2017a), this is an important parameter and the best results are found using θ_{sd}= 1 (Luijendijk *et al.*, 2017a). The logical range for this parameter, which is applied here, is between 0 and 1.

The selected parameters (three for hydrodynamics, four for wave breaking, six for sediment transport and three for morphology) are examined using the Elementary Effects method (EE) (Morris, 1991; Saltelli *et al.*, 2008). The EE method is a way to analyze how sensitive a model's outcome is to different parameters. We examined the importance of the 16 parameters of 4.1 in predicting bed level, volume, and beach width change for a 1.2 y period. With the goal of identifying the top five most influential parameters. The EE is an effective screening method for models with many parameters, while requiring a relatively low amount of computations. The EE follows a random trajectory through the parameter space and varying one parameter at a time. The method provides insight into the influence, as well as the dependence and non-linearity of the input parameters. The procedure and results are described in more detail in Appendix A. The bold-faced parameters indicated in Table 4.1 are found to be the five most influential according to this method and are used in the GLUE approach.

4.2.4. GLUE approach

Generalized likelihood uncertainty estimation (GLUE) is a tool for estimating uncertainty in a prediction by deriving likelihood distributions of free model parameters based on a model-observation comparison (Beven & Binley, 1992). Parameters that produce a prediction with higher skill will be assigned a higher likelihood. An important aspect of the GLUE method is the concept of equifinality (Beven, 1993). Equifinality denotes the possibility that multiple set of parameters can produce predictions that are acceptably consistent with available observations (Beven, 2009). A unique optimal parameter set is non-existent because

Class	Parameter	Symbol	Default value	Luijendijk *et al.* (2017a)	Range EE (GLUE)	Unit
Hydraulics	Chezy bed roughness	C	65	65	50-80	$m^{1/2}/s$
	Horizontal eddy diffusivity	D_h^{back}	0	1	0.1-1	m^2/s
	Horizontal eddy viscosity	ν_h^{back}	0	1	0.1-1	m^2/s
Waves	Wave breaking limit on time-step level	γ_{max}	-	0.8	0.55-0.8	-
	Roller dissipation coefficient	α_{rol}	1		0.1-2 (1-3)	-
	Roller slope	β_{rol}	0.1		0.01-0.2	-
	Wave breaking index	γ	0.55	0.73	0.55-0.8 (0.55-0.8)	-
Sediment	Suspended sediment grainsize scaling factor	fac_{dss}	1		0.6-1	-
	Current related bed and **suspended** transport scaling factors	f_{sus}, f_{bed}	1	0.5	0.1-1 (0.2-1)	-
	Wave related bed and suspended transport scaling factors	$f_{sus,w}$, $f_{bed,w}$	1	0.2	0.1-1	-
	Grain size	d_{50}	-	300	250-350 (200-350)	μm
Morphology	Transverse bedslope parameter	α_{bn}	1.5	15	1-25	-
	Longitudinal bedslope parameter	α_{bs}	1	10	1-25	-
	Dry cell erosion factor	θ_{sd}	0	1	0-1 (0-1)	-

Table 4.1.: Selected free parameters evaluated in the EE analysis with their default value and range. Bold faced variables came out as most influential according to the EE analysis and used in the following step with the GLUE approach.

of parameter interdependence and / or model insensitivity (Ruessink, 2005) or limitations of the model structure. The problem of equifinality is that it might be bound to the spatial or temporal calibration domain, as equifinal parameter sets may respond differently outside this domain (van Maren & Cronin, 2016). A way to find a reliable parameter set is to look for the best combined likelihood over several different time periods or locations (Simmons *et al.*, 2017).

Our choice for GLUE is based on it being a global (in terms of parameter space) extension of the manual calibration process in which optimal calibration parameters are sought based on manual local improvement of model skill values. Therefore, the results are easily extended to lessons for practical model applications and engineering modeling practice.

The GLUE method lets the user search the model parameter space for acceptable parameter sets, by assigning a non-zero likelihood to all sets with a prediction skill above a predefined threshold (Beven & Binley, 1992). The fundamental idea is to assign prior distributions to model parameters (step 1, Fig. 4.4) and subsequently draw a large sample of parameter sets, through (Monte Carlo) sampling (step 2, Fig. 4.4). For each set, the resulting model prediction (step 3, Fig. 4.4) is evaluated against observation data using a skill score (step 4, Fig. 4.4). The predefined threshold determines whether a model prediction is deemed non-behavioral, it is not accepted as a valid solution. For the parameter sets that result in behavioral predictions, a likelihood is determined. This likelihood is largest for predictions with highest skill (step 4, Fig. 4.4). Non-behavioral runs receive a zero likelihood score. The result is a likelihood range for each model parameter (step 5, Fig. 4.4) and an observation-based range of model

predictions due to parameter uncertainty (step 6, Fig. 4.4).

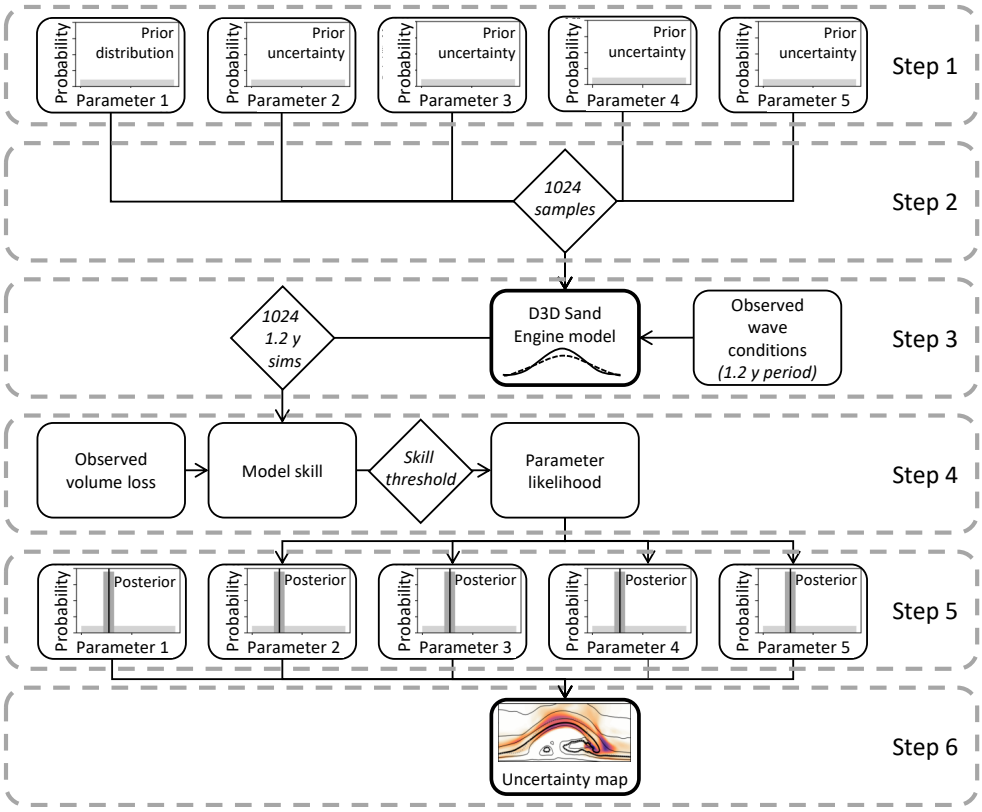

Figure 4.4.: Flow scheme of the GLUE method as applied in this study. Darker colors in the uncertainty map in step 6 indicates areas with more uncertainty.

In the first step, for each of the selected parameters, a uniform prior distribution is assumed to minimize subjectivity of the procedure. The distribution limits are chosen wide enough to sample a sufficient part of the parameter space but within physical limits to prevent non-physical model settings. In the second step, 1024 samples (i.e. a unique combination of five parameter values) are drawn from these uniform distributions. To achieve equal resolution for each parameter and a well-spread sample with a low number of samples, the samples are generated with a quasi-random sampling method: the Sobol' low-discrepancy sequence (Sobol', 1967). The discrepancy is a measure of the deviation of the sampled points from a uniform distribution (Kucherenko *et al.*, 2015). Of the few well-known low discrepancy sampling methods, the Sobol' sequence has been proven to be superior (e.g., Glasserman, 2003; Tuffin, 1996). As samples are gen-

erated evenly over the parameter space, they have a convergence rate of up to $O(N^{-1})$, whereas for Monte Carlo this is $O(N^{-1/2})$. Next, in step three, the Delft3D model is run 1024 times with different sets of parameter values.

In step four, the result of each prediction is compared to observations using a skill metric. In morphological modeling, the Brier skill score (BSS) is an often used way to evaluate model performance (Sutherland *et al.*, 2004; van Rijn *et al.*, 2003). Usually the BSS measures the root-mean-squared error (RMSE) of the predicted bed level in each computational point compared to a baseline prediction of zero change:

$$BSS_z = 1 - \frac{\sum_{x,y} (\bar{z}_{obs}(x,y) - \bar{z}_{mod}(x,y))^2}{\sum_{x,y} (\bar{z}_{obs}(x,y) - \bar{z}_0(x,y))^2} \tag{4.1}$$

in which z_{obs} is the observed bed level, z_{mod} the computed bed level, and z_0 the zero-change baseline. A positive BSS score indicates that the prediction provides more information than having no prediction at all.

Considering known limitations of process-based morphological models, the original BSS metric can be a very strict criterion that penalizes the model twice, e.g., for not reproducing dynamic bar behavior or seasonal effects (Bosboom *et al.*, 2014).To relieve its stringency, the BSS has been tailored to the data and CSIs of interest. We use these adapted BSS metrics to indicate the model's reproductive capacity of observed cumulative volume changes or cross-shore shoreline position. Moreover, this can be done for the total spatial domain or subsets with specific geomorphology (e.g., as done by Armaroli *et al.*, 2013; Bae *et al.*, 2022). All these skill metrics have the same main principles as the original BSS: they are RMSE-based and use zero change as reference, but instead of focussing on bed level they differ in unit (e.g., volume) and can be constrained by location (erosive area, around water line, etc.).

The first adapted version of the BSS focuses on the bed level changes at the head of the Sand Engine only and is hence referred to as $BSS_{z,SE}$. Hereto $x, y \in SE(x,y)$ is used in Eq. 4.1.

The model's ability to predict the shoreline is evaluated using another adaptation of the BSS where deviations between model and observations due to high temporal and spatial variations in the shoreline positions are neutralized by looking at the averaged position over time:

$$BSS_{sl} = 1 - \frac{\sum_{x,t} (\overline{sl}_{obs}(x,t) - \overline{sl}_{mod}(x,t))^2}{\sum_{x,t} (\overline{sl}_{obs}(x,t) - \overline{sl}_0(x,t))^2} \tag{4.2}$$

and a spit focused adaptation $BSS_{sl,spit}$, with $\{x | 1500 < x < 2800\}$.

Finally, to evaluate the model's performance on the prediction of volume changes in different control areas over time, a volume-based BSS metric is used:

$$BSS_{\Delta V} = 1 - \frac{\sum_{A,t}(\Delta\bar{V}_{obs}(A,t) - \Delta\bar{V}_{mod}(A,t))^2}{\sum_{A,t}(\Delta\bar{V}_{obs}(A,t) - \Delta\bar{V}_{0}(A,t))^2} \tag{4.3}$$

Next, the behavioral threshold separates good or acceptable predictions from those deemed unacceptable. The behavioral threshold for each CSI is chosen such that approximately half of the predictions (500-600) are considered behavioral (Table 4.2).

	$BSS_{\Delta V}$	BSS_{sl}	$BSS_{sl,spit}$	BSS_{z}	$BSS_{z,SE}$
Threshold	0.75	0.55	0.52	0.43	0.60
n	587	586	589	574	588
Max	0.95	0.79	0.74	0.64	0.88
Mean	0.74	0.54	0.52	0.44	0.59
Min	0.08	0.10	0.14	0.10	0.02

Table 4.2.: Overview of the applied behavioral threshold for each CSI and the resulting amount of behavioral runs (n). The bottom three rows show the maximum, mean, and minimum BSS for the respective CSIs.

For each behavioral prediction, the likelihood can be computed from the skill value:

$$L_{BSS,i} = \frac{BSS_i}{\sum_{i=1}^{n} BSS_i}. \tag{4.4}$$

In which $i = 1, ..., n$ are the ranked and behavioral predictions.

With the different skill measures, a combined likelihood CL is established and computed as the product of likelihood for several parameters.

$$CL = \left(\prod_{i=1}^{N_L} L_i \right)^{\frac{1}{N_L}} \tag{4.5}$$

In step five, the posterior distribution of each parameter is derived with the combined likelihood. The likelihood scores of the parameter sets are used to transform the prior (uniform) parameter distributions to marginal posterior distributions. This is done by creating a weighted histogram of parameter values based on the likelihood values belonging to each prediction (similar to the computation of the uncertainty bounds, but for the parameter values instead of the CSIs). The result is a likelihood distribution for each parameter. The posterior distributions can then be compared with the prior distributions and the default or reference values for the parameters. In addition, they are used to estimate an optimal parameter set (OPS), which represents the parameter set with the highest likelihood. The OPS is then computed as well to evaluate whether it outperforms other predictions. The influence of each input parameter on the prediction outcomes is quantified using the Kolmogorov-Smirnov (K-S) distance (Spear

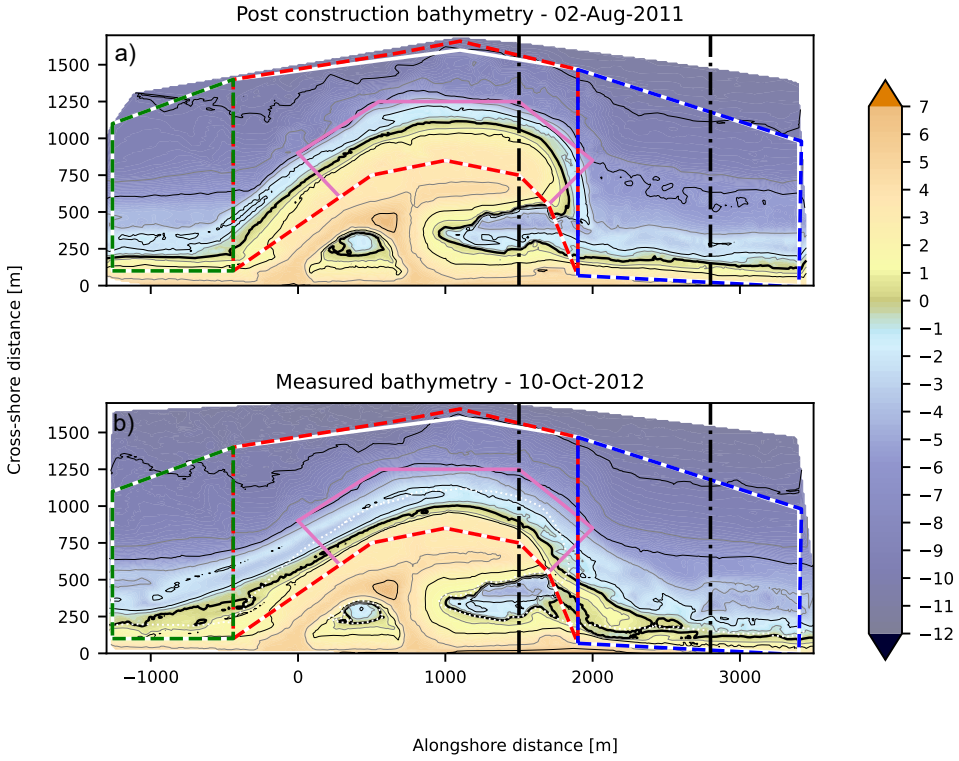

Figure 4.5.: Definition of control areas relative to observed bed level in m+NAP in a) August 2011, and b) October 2012. Bed level control areas are indicated with the solid lines: white denotes the area for BSS_z and pink for $BSS_{z,SE}$. The volume change control areas A_i are indicated with the dashed lines: green denotes area S, red denotes area mid and blue denotes area N. The shoreline is subdivided by the dash-dotted line to indicate the spit area for $BSS_{sl,spit}$. The black lines indicate the -10, -6 -2, 2 and 6 m+NAP isobaths, the bold black line represents the shoreline (0 m + NAP).

& Hornberger, 1980). This K-S metric denotes the largest distance between the prior and the posterior cumulative probability density. A high K-S value is an indication of a highly influential parameter, while a low K-S value indicates a non-influential parameter.

In the final step, uncertainty bounds are analyzed by looking at the results of all behavioral model runs for the different CSIs. Uncertainty bounds are visualized using a confidence interval (W_{CI}). A W_{CI} presents a range of plausible values for a stochastic variable and is accompanied by a confidence level. For example, $W_{CI90\%}$ gives a range of values for a stochastic variable, with a confidence level of 90% that the true value lies within this range. The upper and lower bounds of the $W_{CI90\%}$ are obtained from the 95^{th} and 5^{th} percentiles of the empirical CDF instead of using for example twice the standard deviation to get to the 95% CI because CSIs are non-Gaussian distributed.

4.3. Results

4.3.1. Bandwidth of coastal state indicators in behavioral predictions

After the GLUE procedure we have nearly 600 behavioral runs from the Sand Engine's initial 14-month evolution. This set of runs is used to map the parameter uncertainty in two spatial dimensions and in time. As a first step, the 90% confidence interval ($W_{CI90\%}$) of the behavioral predictions is analyzed to determine where the uncertainty of the model manifests itself in the results. This is done for the bed level data as well as for the volume changes and coastline position.

The Delft3D model results show significant erosion at the head of the peninsula between the -6 and 2 m+NAP isobath, flanked by two deposition areas to the north and south (Fig. 4.6a,b,c,d). These modeling results are similar to those reported in Luijendijk *et al.* (2017a).

The uncertainty in the prediction of the bed level varies greatly over the prediction domain (Fig. 4.6e).The uncertainty is largest around the -2 m+NAP isobath, the waterline of the eroding head section, and at the edges of the spit deposition area, with an area of relatively low uncertainty in the center of the spit deposition area. The high uncertainty around the head section of the peninsula indicates that the predicted erosion varies significantly over the predictions. The increase in uncertainty ($W_{CI90} \approx 1-2$ m) along the -2 m+NAP isobath is an indication of uncertainty in the prediction of the height and/or position of the near-shore sandbar. However, the area with low uncertainty along the edge of the spit shows that all predictions indicate the formation of this sand spit. Whereas, the area of high uncertainty around the tip of the spit indicates that it is mainly the length and position of the spit that differ between the predictions. Finally, beyond the isobath of -6 m+NAP, uncertainty rapidly decreases to low levels (<0.25m).

The peninsula's spit and surf zone display both the highest bed level changes and the widest confidence interval between the behavioral predictions. A local pointwise comparison shows that large bandwidths (W_{CI90}) are correlated with large changes in bed level (r^2 = 0.42). However, uncertainty can also be high in places where predicted bed level changes are small, especially in the peninsula's

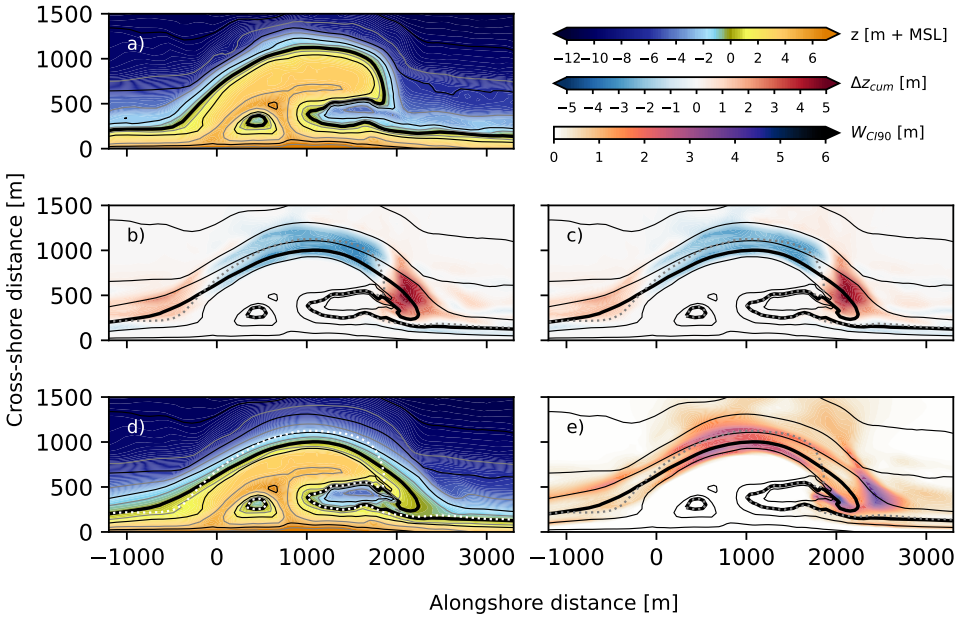

Figure 4.6.: Results of the behavioral Sand Engine predictions. a) Initial bathymetry in August 2011, b) bed level changes for the prediction with the highest likelihood, c) median of predicted bed level changes across all behavioral runs (blue colors indicate erosion and red colors indicate sedimentation), d) predicted bed level from the simulation with the highest likelihood, and e) width of the 90 % confidence interval (W_{CI90}) of the bed level changes (darker colors indicate higher uncertainty). The black contour lines are from the predicted bed level with the highest likelihood (b-e), or the initial bathymetry (a). The predicted 0 m+NAP depth contour is indicated with the thick black line, and the initial depth contour is indicated with the black dotted line. The other contour lines depict the -10, -6, -2, 2 and 6 m+NAP isobaths.

spit area. For example, the area with a large confidence interval near the tip of the spit (x ≈ [2400, 2700]), extends about 200–300 m further north (Fig. 4.6e) than the zone where high accretion is expected (Fig 4.6d, x ≈ [1900, 2400]).

The uncertainty in predicted bed levels translate also into uncertainty in the volume balance, Fig. 4.7a. Erosion in the central section (4.7b) shows a spread of 1.3 million -0.4/ +0.7 million m^3 after the 14 month simulation period. Corresponding accretion volumes in the adjacent South (4.7c) and North (4.7d) sections show spreads of 0.29 -0.10/ +0.12 million m^3 and 0.83 -0.23/+0.40 million m^3, respectively. Hence, uncertainty is largest for the central section (W_{CI90} = 1.12 million i.e. m^3, 85%), followed by the North section (W_{CI90} = 0.63 million i.e. m^3, 76%). Moreover, we can see that the parameter uncertainty results in

non-gaussian distributed predictions of volume change as the predictions are asymmetric towards higher magnitudes of change.

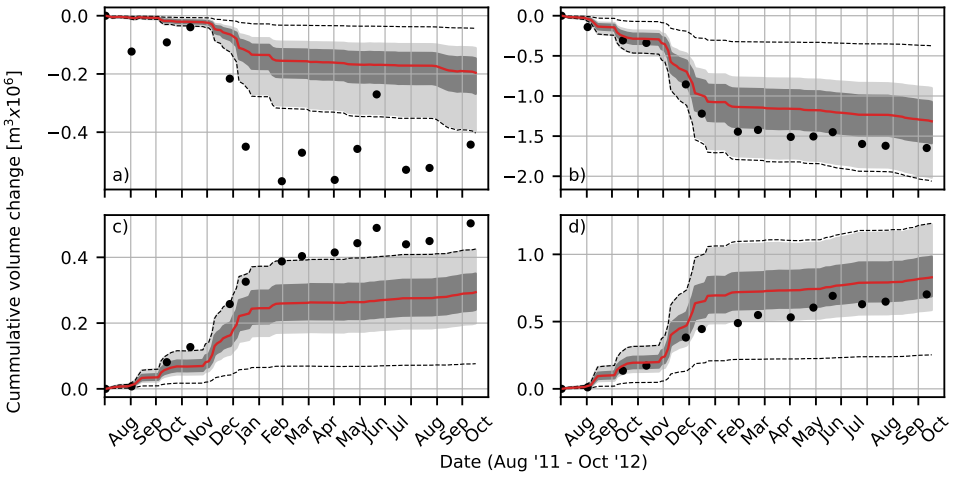

Figure 4.7.: Observed (dots) and predicted volume changes in time for a) entire Sand Engine, b) central section, c) South section, and d) North section. The light and dark grey shaded areas indicate the 90% and 50% confidence intervals of the behavioral predictions, respectively. The solid lines indicate the predicted median values. The dotted lines span the range of all predictions.

Uncertainty in the bed level also results in uncertainty of the predicted shoreline position. In all behavioral predictions, a spit develops at the peninsula's northern edge, but the different predictions reveal considerable uncertainty in spit location (Fig. 4.8a). The spit area contains the most uncertainty, as W_{CI90} of the most seaward position of the shoreline (brown, dashed line in Fig. 4.8b) reaches up to 375 m in cross-shore position (at x ≈ 2100 m). Along the rest of the Sand Engine, the maximum confidence interval width of the shoreline rarely exceeds 100 m.

Uncertainty in bed level elevation, volume, and shoreline is influenced by the wave forcing. Initially, the magnitude of volume change increases with the high-energy events in October, December, and January (Fig. 4.7), showing a strong correlation to the incoming wave energy ($r^2 = 0.88$, first seven months). After the first seven months, the increase/decrease is more moderate and less dependent on the incoming wave energy ($r^2 = 0.62$). A model result that is in accordance with observations (de Schipper *et al.*, 2016). For this period, the correlation between uncertainty growth and observed changes is significantly reduced ($r^2 = 0.26$).

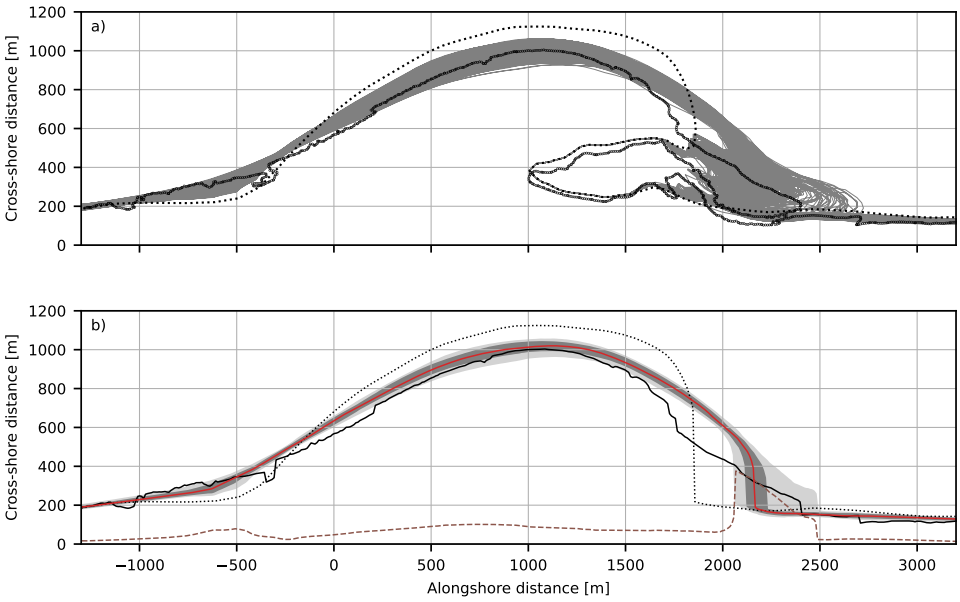

Figure 4.8.: Predicted shoreline positions. a) Shorelines of all behavioral runs (grey lines), initial shoreline (black dashed line), and observed shoreline in October 2012 (thick black line). b) Most seaward position of the shoreline. 50 and 90 % confidence intervals (grey shaded areas), width of the 90% CI (W_{CI90}, brown dashed line), median position (red line), initial position (black dotted line), and observed position in October 2012 (black line).

4.3.2. Parameter sensitivity and optimization

The weighted histogram from the parameter sets gives the posterior parameter distributions, using the combined likelihood (CL) values as weights (Fig. 4.9). The individual likelihood definitions for volume, shoreline, and bed level each contain between 570 and 590 behavioral predictions (see Table 4.2). Based on the combined likelihood 507 parameter sets are behavioral, meaning that parameter sets that are found to result in a behavioral prediction based on one skill metric are often also behavioral for the others, indicating there is general agreement among the different likelihood definitions.

The more the posterior distribution of a parameter differs from the prior distribution, the more it affects the model outcome and skill. For parameters f_{sus}, γ, and d_{50}, the posterior distribution shows a clear variation across the parameter space (Fig 4.9a,c,e). Especially for f_{sus} and γ, this is underlined by a high K-S distance (>0.2). Furthermore, the parameter values with the highest likelihood of f_{sus} and γ (yellow lines in Fig 4.9a,c) coincide with the peak of the distribution, indicating that these parameters are most influential.

Higher values of parameters f_{sus} and γ have a higher likelihood, indicating that the model performs better when sediment transport scaling is high and wave breaking is initiated at smaller water depths (i.e. a more concentrated surfzone). The distribution of d_{50} shows a peak at 240–250 μm. The reference value (Luijendijk *et al.*, 2017a) for γ and θ_{sd} deviated strongly from the Delft3D default parameter settings (Deltares, 2019) which is supported by the posterior distributions found here, which show a higher likelihood around the reference values. This is not the case for f_{sus} which clearly shows a higher likelihood for values higher than the reference value, in combination with a lower d_{50} than the reference value.

The distribution shapes with a peak close to the limits of the investigated ranges might suggest insufficient exploration of the parameter space. Although f_{sus} is in practice never larger than one and θ_{sd} cannot be larger than one for physical reasons. In theory, the range of γ can extend to higher values than 0.8, however, this is a rare choice in literature for Delft3D simulations. Which leaves α_{rol} for which the lower limit was possibly chosen too high.

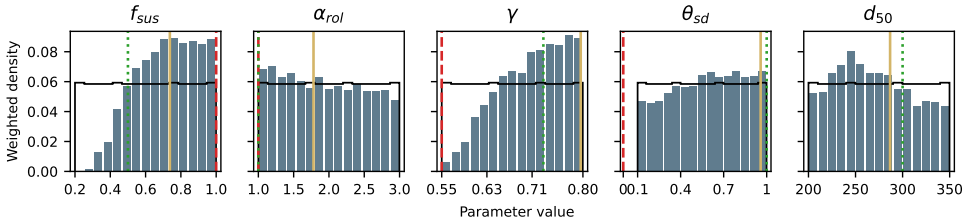

Figure 4.9.: Prior (black line) and posterior distributions (histogram bars) for the five input parameter examined in the GLUE analysis together with the Delft3D default values (red, dashed line), reference values used by Luijendijk *et al.* (2019) (green, dotted line), and values for simulation with the highest combined likelihood (yellow line). The posterior distributions are weighted according to the combined likelihood (Eq. 4.5).

Parameter interdependence can make optimal parameter values difficult to identify (Ruessink, 2005). Between the five parameters evaluated with GLUE, there are two notable correlations, Fig. 4.10. A high f_{sus} value is positively correlated to a higher d_{50} value (r = 0.29) while it has a negative correlation to γ (r = -0.27). Although not strong, the correlations are significant and complicate identification of optimal parameter settings.

Optimal parameter sets in case of parameter dependence can be approximated by conditioning the computations (on the most influential parameter) and create conditional posterior distributions for the other parameters, given the selected value for the first parameter. If the sample size is sufficient, this process can be repeated after each parameter, creating new conditional distributions for the remaining ones. To ensure a reasonable sample size (50–100 samples),

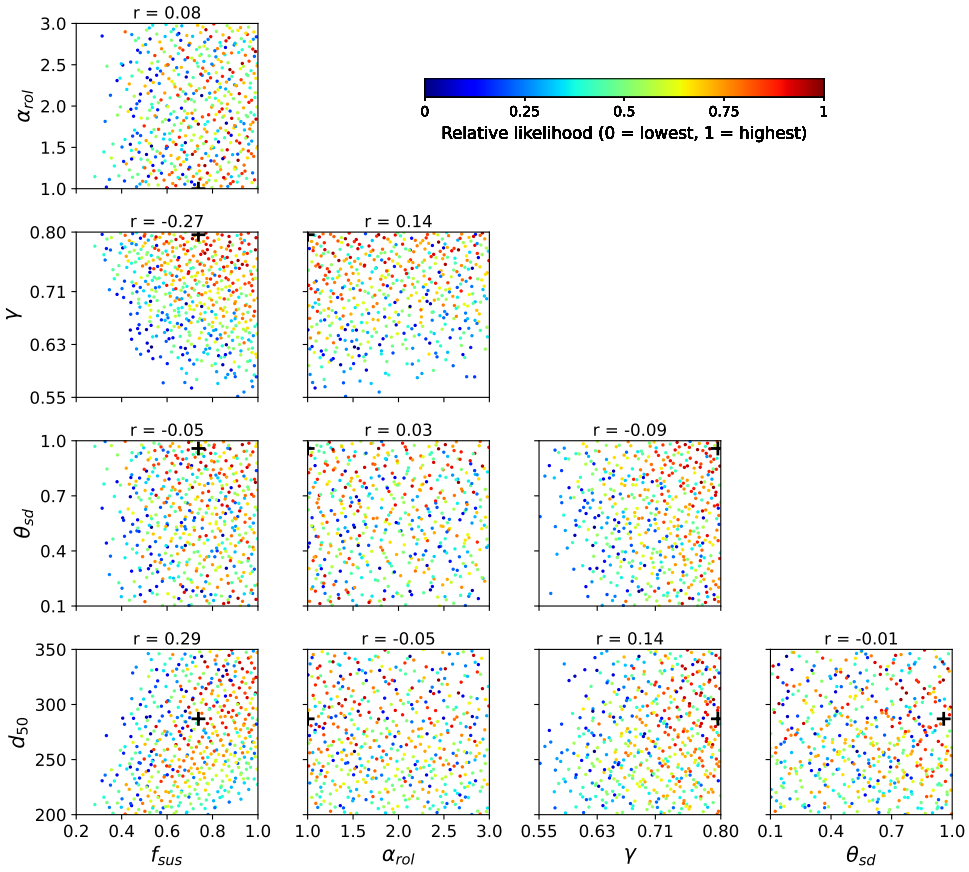

Figure 4.10.: Overview of correlations between each set of two parameters of the GLUE analysis. The correlations are based on the behavioral parameter sets for combined likelihood (507 predictions). The colors of the dots indicates the magnitude of the combined likelihood (red implies a high likelihood prediction, blue a low likelihood). Correlation values (r) are given in the panel titles. OPS_4 was selected based on a visual inspection of the correlation plots and shown by the black cross in each plot.

the conditional distributions are created from all parameter sets, for which the value of the fixed parameter (f_{sus}, γ, or d_{50}) deviates by a maximum of 5% from the selected optimal value.

Considering the sample size (1024), we only condition the distributions once and choose the most likely setting for the remaining four parameters. We do this three times for the three most influential parameters (f_{sus}, γ, or d_{50}), leading to three different approximations of the optimal parameter sets (OPS_1, OPS_2 and

OPS_3). Predictions with these parameter sets show a skill within the highest 95% of all predictions. The next set OPS_4 is obtained by visual inspection of the correlation plots in Fig. 4.10.The parameter values are estimated by manually selecting areas in the correlation plots that visually contain the high-likelihood predictions (red colours). The final set (OPS_5) is simply obtained from the prediction with the highest combined likelihood (rank 1).

Theoretically, finding a higher scoring OPS than OPS_5 should be possible by selecting the most likely values from the conditional distributions. However, OPS_2 ranks highest compared to the other sets but does not exceed the scores of OPS_5, except for $BSS_{z,SE}$, where it ranks 11^{th} while OPS_5 ranks 36^{th}. OPS_2 is based on the conditional distributions for $\gamma \approx 0.78$, further supporting the indication that γ has the most influence on the model skill. Furthermore, all OPS's show an increase in model skill over the reference prediction by Luijendijk *et al.* (2019). Especially for the shoreline position BSS_{sl} and $BSS_{sl,spit}$) the model skill for the OPS prediction is considerably higher (rank 9-60) than for the reference prediction (rank 509/579). Adding more samples around these optimal areas in the parameter space could help to improve the skill of the optimal set further.

		CL	$BSS_{\Delta V}$	BSS_{sl}	$BSS_{sl,spit}$	BSS_z	$BSS_{z,SE}$
OPS_1	Rank	29	106	63	42	16	41
	Percentile	97.2	89.7	93.9	95.9	98.4	96.0
OPS_2	Rank	6	27	25	20	5	11
	Percentile	99.4	97.4	97.6	98.0	99.5	98.9
OPS_3	Rank	63	61	30	55	111	107
	Percentile	93.9	94.0	97.1	94.6	89.2	89.6
OPS_4	Rank	23	154	27	48	16	36
	Percentile	97.8	85.0	97.4	95.3	98.4	96.5
OPS_5	Rank	1	11	9	12	5	36
	Percentile	100	98.9	99.1	98.8	99.5	96.5
Ref	Rank	338	43	509	579	274	179
	Percentile	67.0	95.8	50.3	43.5	73.3	82.5

Table 4.3.: Overview of the rank and corresponding percentile of the five OPS predictions and the reference prediction among the 1024 GLUE predictions.

Although the value for the model skill of the five best OPS predictions is very similar, the results differ significantly for the various CSIs. The predicted volume changes between OPS_1 to OPS_5 predictions span 40-50% of the width of the 90% confidence interval (Fig 4.11). This variation in the predicted volume changes is significant considering that the parameter values of the OPS's are relatively close together (i.e. f_{sus} only varies between 0.72 and 0.85 and γ between 0.76 and 0.80).

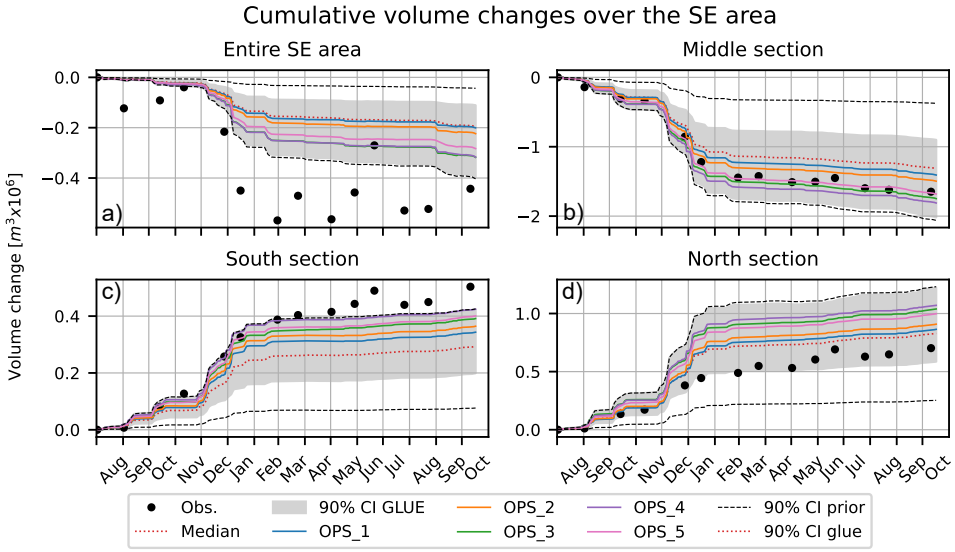

Figure 4.11.: Time series of cumulative volume changes for a) entire Sand Engine, b) central section, c) South section, and d) North section, showing the observations (black dots), 90% CI (grey area) and median (red, dotted line) of the behavioral GLUE predictions (black dashed lines), and the OPS predictions (solid, coloured lines).

4.3.3. Sensitivity of input parameter distributions to CSI of interest

Calibrating of the model on one CSI does not lead to the best results for other CSIs. In the previous paragraph, a combined likelihood was used that weighted skills for different CSIs. However, depending on the purpose of the model and therewith the CSI or area of interest, focus might be on a single definition of the likelihood or on a specific area.

Comparing the likelihood distribution of the different input parameters for different CSIs shows that the results can be quite sensitive (Fig. 4.12). Looking at the input distributions, it is especially the volume based posterior distributions that deviate with the CSI. For instance, the d_{50} is much more important to predict accurate volume change, (K-S=0.13) than shoreline or bed level. As a result, for a volume based likelihood definition (using eq. 4.3 and 4.4) lower values of d_{50} are more likely compared to shoreline and bed level. Despite of these differences in the distributions, the most likely value is similar. On the other hand, when the focus is on the shoreline rather than volume changes, θ_{sd} has six times more influence on the model results. To optimize shoreline position an optimal value would be θ_{sd}=1, while for volume the specific value of θ_{sd} wouldn't matter. A logical result, considering θ_{sd} affects the bed level locally around the wet-dry interface in cross-shore direction. An effect that is neutralized by aggregating

volumes over a larger domain. Similarly, when the focus is on bed level instead of volume, γ is twice as influential in terms of K-S distance. Only the distribution of f_{sus} is virtually insensitive to the CSI of interest.

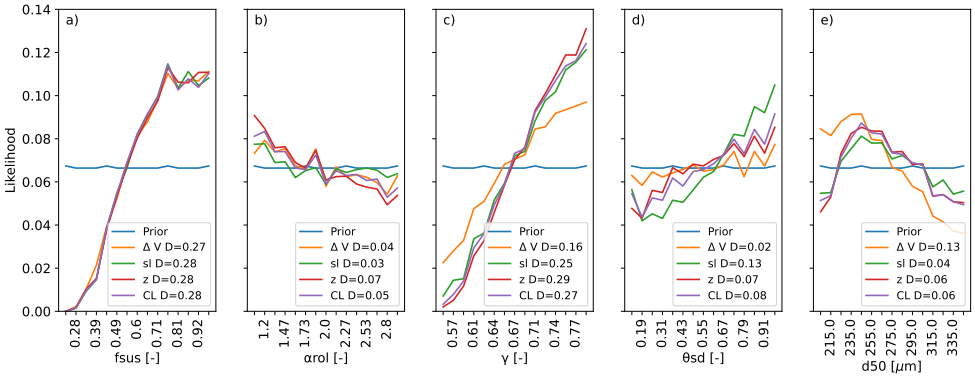

Figure 4.12.: Sensitivity of posterior distribution to Coastal State Indicator used for calibration. Distributions are shown for the CSIs calculated over the entire modeling domain for a) f_{sus}, b) α_{rol}, c) γ, d) θ_{sd}, and d_{50}.

The likelihood distribution of the input parameters can be sensitive to the area of focus. This follows from computing the volume likelihood eq. 4.3 and 4.4 for each control area individually instead of summing over all control areas (Fig. 4.13). This analysis shows that especially the likelihood distributions derived for the northern side of the SE deviates from the other areas. In all cases, the K-S distance for the north area is lowest, which means that there is no apparent difference between the prior and posterior distributions, or the difference is less pronounced than for the other areas.

4.4. Discussion

4.4.1. Parameter optimization and equifinality

One of the aims of the GLUE methodology is to optimize parameter settings. Considering the limited number of samples and the correlations between several parameters, it is challenging to identify optimal parameter values or determine whether a single optimal set exists. Still, several parameter sets (OPS_1-OPS_4) could be identified with high skill by accounting for correlations through conditional posterior distributions. Although similar in magnitude, none of these OPS predictions result in higher skill than the highest skill within the sampled sets (OPS_5).

The skill and combined likelihood scores of the 35 best GLUE predictions are similar to those of the OPS predictions. As there are numerous different parameter sets resulting in a similar model skill, this confirms the model's equifinality. As none of the OPS predictions have a higher skill than the GLUE simulations, it

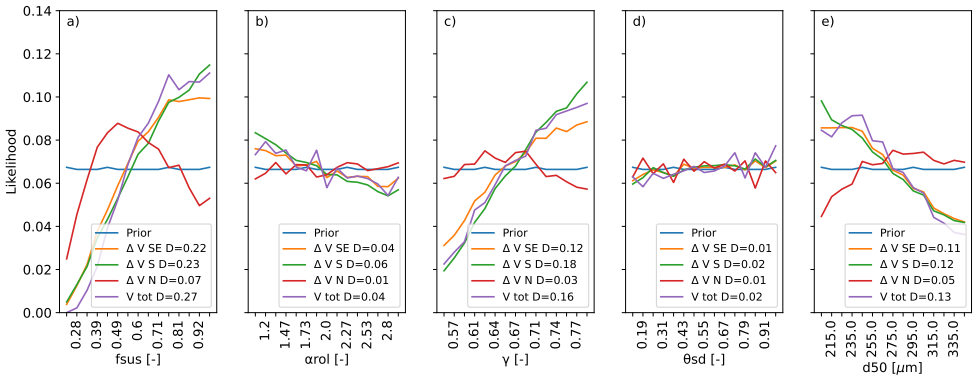

Figure 4.13.: Sensitivity of posterior distribution to the spatial zone used for calibration. Distributions for a) f_{sus}, b) α_{rol}, c) γ, d) θ_{sd}, and d_{50} are shown for the Volume based BSS (i.e. $BSS_{\Delta V,N}$, Eq. 4.3).

implies that the maximum achievable model skill (within the limits of the selected parameter ranges) may be close to that of OPS_5. Moreover, the best predictions show a significant increase in model skill compared to the reference simulation (Luijendijk *et al.*, 2019). Rather than continuing the search for an optimal parameter set for the current conditions, investigating the OPS performance for a validation period will likely prevent overfitting and improve the generic applicability of the found parameter settings.

Our results show a strong sensitivity to the choice of the CSI and the spatial subdomain used in the calibration. Hence, the parameter values that yielded the best predictions may not be transferable, and the existence of a 'best' generic value for the model parameters is unlikely. Moreover, due to computational capacity limitations, not all influential parameters were explored, and for some of the explored parameters, the explored parameter ranges were possibly set too narrow. This means that the found optimal parameter settings are optimal given that other parameters and ranges (e.g., $f_{sus,w}$ and fac_{dss}) are unaltered. Therefore, we do not recommend updating the Delft3D default parameter settings based on the results of this case study alone.

4.4.2. Limitations of GLUE

The GLUE method can be criticized for its subjectivity and non-formality (e.g., Beven & Binley, 2014; Sadegh & Vrugt, 2013; Simmons *et al.*, 2017). Subjectivity originates from several decisions in the setup of the GLUE analysis. Such decisions influence the width of the established uncertainty bounds and include the determination of the behavioral threshold, choice of likelihood definition, and the selection of parameters, ranges, and prior distributions. Regarding the non-formality of the method, as Sadegh and Vrugt (2013) formulate it nicely, "an informal likelihood measure is used to avoid over conditioning and exclude parts

of the model (parameter) space that might provide acceptable fits to the data and be useful in prediction". This means that choosing an informal likelihood measure is a deliberate choice to improve results at the cost of reducing objectivity.

These drawbacks of the GLUE method have consequences for interpreting this work. First, the results of the GLUE analysis should not be seen as an absolute quantification of the parameter uncertainty in the model. Instead, they give estimates of the uncertainty based on the conditions for the particular case study. As long as this is accepted, the subjectivity of the GLUE method does not need to disqualify the results. It can be a strength, allowing the modeler to apply the method heuristically. For example, to identify temporal or spatial uncertainty hotspots or assess the relative importance of parameter contributions to the model's uncertainty.

In this study, for example, the behavioral thresholds are set at different values for the different CSIs. While this might appear statistically informal, it enables the derivation of combined likelihood values to select parameter settings with high performance concerning different CSIs. This would not be possible with a single threshold for all CSIs, as this would lead to significant differences in the number of behavioral predictions. Moreover, due to the difference in complexity and dimensionality of the CSIs (the cumulative volume changes consider an aggregated quantity over a particular area, while the bed levels are considered point-wise in two dimensions) it would not be reasonable to expect similarly high skill values for the different CSIs. Hence, as long as the subjectivity is acknowledged, the GLUE results can give valuable insights into the parameter-induced uncertainty in the model.

4.4.3. Model imperfection

The uncertainty bounds from the GLUE analysis show that some model imperfections remain outside the influence of the examined parameter ranges. For example, all behavioral predictions overestimate the asymmetrical distribution of larger sediment deposition to the north and smaller to the south (Fig. 4.7c,d). Even for the OPS and best-scoring GLUE predictions, accretion is overestimated in the north and underestimated in the south. The parameter optimization reveals that none of the investigated parameters can significantly improve volume predictions in the north area without reducing predictive capacity in other areas or for other CSIs. This is in line with results of Luijendijk *et al.* (2017a), which display relatively high skill on volumes but much lower on shoreline and bed levels. Another example is the spit evolution. Practically all behavioral predictions result in the formation of a sand spit, and some also correctly predict the deposited volume in the north section. However, none accurately indicates the spit's cross-shore location (see Fig. 4.8), with the spit predictions always being further seaward than observed.

These errors may be caused by general model inadequacies, such as omitted processes, which are unrelated to the model parameters (e.g., aeolian transport (Luijendijk *et al.*, 2017b) or sediment sorting and armoring (Huisman *et al.*, 2016)

or 3-dimensionality of processes). Another possibility is that they are caused by processes that remain unresolved in the applied discretization (i.e. course spatial or temporal resolution) or by the used acceleration techniques. For example, the shape of the spit can be sensitive to the tide and the distribution of sediments to the north and south to the reduction of the wave climate. Also, the correct reproduction of waves by the model can be important for the predicted coastline position (Chataigner *et al.*, 2022). On the other hand, not-included parameters or unexamined values of included parameters may positively influence model outcomes. Ultimately, when looking at the uncertainty bounds from the GLUE analysis, it is essential to consider that they do not reflect the entire range of outcomes, but merely the possible outcomes within the bounds of the selected parameters.

4.4.4. Relative importance of parameter uncertainty

Parameter uncertainty is not the only source of uncertainty; intrinsic uncertainty, such as variations in wave forcing, can also be an important source of uncertainty (Chapter 3). This is illustrated by several additional predictions where wave forcing is varied. Hereto, we simulated eight 14-month periods of Sand Engine evolution using historical data of average and extreme years of wave energy while keeping parameter settings constant; see Fig. 4.14. Average and high energy years can result in a 25-30% variation in predictions, but calm years can more than half the predicted volume changes. Although this comparison is not quantitative, it shows that parameter uncertainty and wave climate variability significantly influence the predicted results on this timescale.

In addition, parameter uncertainty can be correlated with wave forcing. Based on our results, it cannot be concluded that parameter settings and forcing are correlated, but we do show that the growth of uncertainty is related to the magnitude of changes, and thus the incoming wave energy. They are indicating that a correlation is likely, which is also found in literature. For example, Wilson (2023) show that the origin of uncertainty differs for erosive and accretive conditions, indicating a correlation between uncertainty and forcing. Ibaceta *et al.* (2022) significantly improve predictions when including forcing dependent (non-stationary) model parameters, demonstrating their interdependence. Such non-linear interactions have the potential to amplify uncertainty bounds. On the contrary, Jamous *et al.* (2023) find that parameter interactions can also decrease as the magnitude of boundary conditions increases, which could potentially reduce uncertainty bounds. Nevertheless, parameter uncertainty cannot grow infinitely. Uncertainty in predictions will be physically bound (Vitousek *et al.*, 2021). In an alongshore-dominated system, e.g., by sediment availability and transport capacity, and in a cross-shore dominated system, e.g., by physical limits on profile slope.

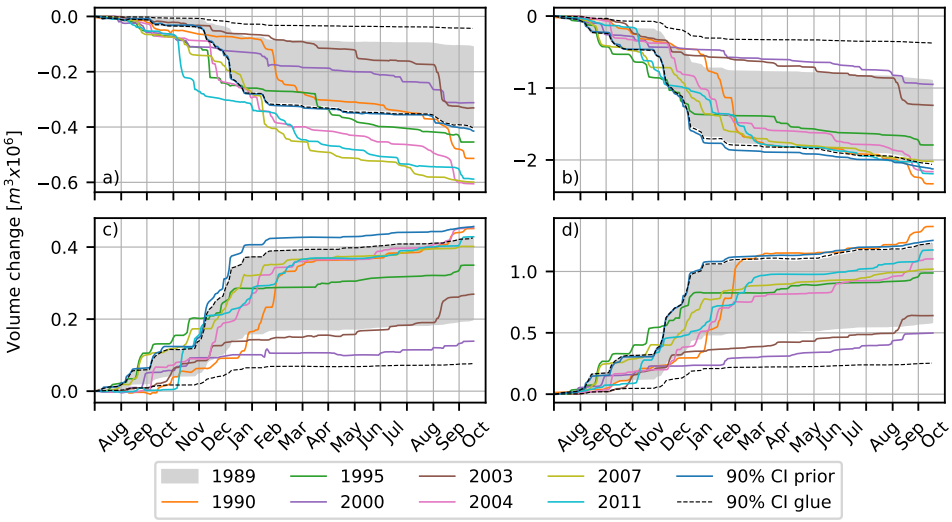

Figure 4.14.: Time series of cumulative volume changes showing the 90% CI of the behavioral GLUE predictions (gray area) and all GLUE predictions (black dashed line) and the volume changes computed for the various wave climate predictions (colored lines).

4.4.5. Implications for practical applications

These findings demonstrate that in using process-based models to forecast various (aggregated) coastal state indicators, model limitations, and structural errors can result in varying model skill for different CSIs. A perfect model would score equally high in bed level, volume change, and beach width predictions because these CSIs only differ in weighting and aggregation. For imperfect models, however, depending on the CSI of interest, the importance of the input parameters can vary. If interested in a local variable (e.g., coastline) or limited area, sensitivities may not be apparent when calibrating on a global variable (e.g., bed level), and valuable model optimization can be missed. This illustrates how difficult it is to generalize parameter settings to other cases when they are so sensitive to model purpose and area of focus.

However, instead of generalizing the parameter settings, generalizing the results leads to several recommendations for good model calibration practice. For instance, it is critical to keep the model's purpose and CSI of interest in mind when calibrating the model. Furthermore, when manually or automatically finding parameter settings with high skill, there is no guarantee of finding the optimal set. The equifinality found in the model means that similarly high-scoring sets can have very different results locally, underlining the importance of model validation and uncertainty propagation.

4.5. Conclusion

The multi-dimensional parameter space of a coastal area model was explored to quantify uncertainty in predicted coastal state indicator values that follow from the uncertainty in the model parameter values. We examined (spatial and temporal variations of) coastal state indicators bed level, sediment volume in budget areas, and shoreline position. Uncertainty was quantified with over 1000 Delft3D computations of the Sand Engine mega-nourishment's first 14-month evolution after construction.

An extensive set of parameters is considered and systematically reduced to five key parameters. Uncertainty in these five input parameters translates into significant uncertainty in predicted CSI values. Volume changes for sediment budget analyzes can vary by $75 - 85\%$ of predicted changes, predicted coastline position by $\pm$ 100 m, and bed level change confidence can range up to 5 m (90% confidence values). The parameter uncertainty creates the widest confidence intervals at locations and moments when the absolute changes are most significant. For the Sand Engine, this translates into wide confidence intervals for bed level and coastline predictions in the spit area and around the -2m+NAP isobath. Wave forcing is important as 90% of this uncertainty is generated in the first seven high-energetic months. The resulting uncertainty distributions are non-Gaussian with an asymmetric shape to larger changes.

The suspended sediment transport scaling (f_{sus}), the breaker index (γ), and the grain size (d_{50}) contribute the most to the overall uncertainty in the Delft3D morphodynamic predictions. Because the investigated parameters are partially correlated, finding true optimal parameter settings or confirming the existence of a single optimal set is challenging. Several near-optimal sets were identified by constraining the other parameters to the most optimal value for the three most influential parameters. Still, none of these optimal predictions result in a skill higher than the highest skill within the sampled sets. All three sets outperform the manually calibrated reference computation of Luijendijk *et al.* (2017a).

Across the different parameter sets with very high and comparable skill outcomes can be substantially different. For example, volume changes in the center of the SE can vary with $\pm 50\%$, and the tip of the spit can vary $\pm$500 m in alongshore position. This highlights the equifinality in the model and the need for validation rather than further optimization to prevent overfitting.

The model's sensitivity can vary significantly depending on the CSI of interest. For combined CSIs, the model is relatively insensitive to the wave energy dissipation coefficient (α_{rol}) and the dry cell erosion factor (θ_{sd}). However, θ_{sd} is a critical parameter in modeling the shoreline position. Furthermore, input likelihoods and optimal parameter settings may differ depending on the area of focus. Because of these sensitivities, the parameter values that yielded the best results may not be transferable, and there may be no single 'best' generic value for each parameter. Our results underline the importance of a good model calibration practice. Herein, the calibration area and parameter(s) of choice should be consistent with the CSIs to predict, as they can significantly impact the outcome of the (manual) calibration procedure.

5

Synthesis

The contents of this dissertation explore uncertainties in predictions of large-scale sandy interventions. From Chapter 3, we can conclude that it is possible to estimate the uncertainty in predicting the volumetric changes of a large-scale nourishment with a relatively simple model. In some instances, these relatively simple models, as used in Chapter 3, do not provide information on all desired coastal state indicators (CSIs). Especially since the CSIs can display contrasting behavior, Chapter 2. It is possible to estimate uncertainty with more complex coastal area models with a higher skill at predicting more complex predictors such as beach width or inter-tidal area (Chapter 4). However, such a 2D coastal area analysis comes at the cost of a high computational effort, a very complex analysis, and low transferability to other sites. This makes a trade-off between effort and predictability of more complex CSIs inevitable. This chapter explores the expected evolution after a large-scale sandy intervention, the benefits of increasing model complexity in predicting it, and how to quantify uncertainty in the predictions for the next intervention.

5.1. Evolution of large-scale sandy interventions in general

This dissertation focuses on two large-scale sandy interventions in the coastal zone, the Hondsbossche Dunes (HD) and the Sand Engine (SE). At both interventions, significant equilibration in cross-shore and alongshore directions is observed. The alongshore equilibration process at the HD had a longer time-scale than the cross-shore adaptation. Considering the examples of large-scale sandy interventions of Fig. 1.1, this does not necessarily have to be a generic observation but will depend on the intervention's geometry and local forcing conditions, such as the wave and wind climate. The SE is a case with a very strong signal because of its protruding geometry (high cross-shore over alongshore width ratio) and very distinct zones in which different processes dominate, such as the tide-dominated lagoon and the wave-dominated head of the SE. The HD protrudes less but still exhibits a strong alongshore equilibration signal. However, the subaerial evolution at the SE and the HD is quite different. At the HD, observed

dune growth is relatively strong compared to the nearby coast. In contrast, at the SE, the dune growth is relatively low because of interception by local geometric features of the design, such as the dune lake and lagoon (Hoonhout & de Vries, 2017). Further generalization remains challenging due to large-scale sandy interventions' wide range of dimensions and designs.

The uncertainty quantification of Chapter 3 and 4 were carried out for the SE. With its lower coastline gradient and more elongated shape, the HD has a weaker signal-to-noise ratio and is, therefore, more difficult to reproduce with a model. This could mean that the relative importance of epistemic uncertainty is higher for the HD than for the SE. The HDs' alongshore geometry is more homogeneous compared to the SE. This possibly reduces the spatial differences in uncertainty. However, significant differences can be observed at the HD on a smaller scale. Locally, beaches may be narrower or wider, and dune volume changes can fluctuate. These local scale variations are especially difficult to capture in a model. The environmental conditions at both study sites are pretty comparable. Yet, variations in grain size and wave climate can be important. These sensitivities to geometry and environmental variables are considerations that need to be accounted for when extending the results of this thesis to future large-scale sandy interventions.

5.2. Increasing model complexity

In this dissertation, both a one-line (Chapter 3) and a coastal area modeling (Chapter 4) approach were used to examine uncertainty. The area modeling approach allowed for a more detailed analysis of how uncertainty was generated, but at such a computational cost that it was not used to investigate the relative importance of model parameter uncertainty compared to epistemic uncertainty sources. Yet, using these different approaches leaves an important question unanswered: "Is model uncertainty an equally important source of uncertainty when a more complex model is used?".

The predictions of Chapters 3 and 4 are not directly comparable. Therefore, the one-line model is rerun for the same period as the coastal area model, and the likelihood definition for the coastal area model is changed to a volume-based one (e.g., using eq. 4.3 only), comparable to what was used with the one-line model. Although it was a deliberate choice not to use the one-line model of Chapter 3 to predict the initial adaptation of the SE, it can be done at the cost of a lower predictive skill (Fig. 5.1a,b). By changing the hindcast period and the likelihood definition, not all differences are cleared because in the comparison with observations, different choices were made to in- (one-line) or exclude (area model) parts of the subaerial zone, and other skill and threshold definitions were used. Despite these differences, there are several noteworthy similarities in results. First, both predictions show increased uncertainty at moments in time with more considerable volume changes. Second, the 90% confidence interval is of the same order of magnitude (Fig. 5.1b,d). Last, both models show a similar temporal variation and are especially good at representing the observed volume

change between consecutive surveys at t= 88, 125, 158, and 373 d (Fig. 5.1a,c). Nevertheless, there are also some noteworthy differences. For instance, the skill of the coastal area predictions is higher than that of the one-line prediction, and the likelihood distribution of the coastal area model is more asymmetrical, with a higher likelihood for lower volume changes. As a result of the higher skill, the 50% confidence interval of the coastal area model is about 1.5 times smaller than that of the one-line model.

This comparison shows that a simpler one-line model approach can be an appropriate tool in uncertainty quantification. Especially considering the enormous difference in computational effort (minutes versus days), which allows for much more one-line predictions, longer time-scales, and a more thorough parameter space investigation. For the one-line model approach, the quantified uncertainty is probably governed by model structural error (W. E. Walker *et al.*, 2003), and model parameter uncertainty dominates when using more complex models with more parameters. This suggests that for the coastal area model approach, uncertainty will remain an important source, albeit that the time scale on which it would be responsible for more than half of the uncertainty is probably a bit longer than 2.5 years when applied in a similar approach to that of Chapter 3. Note that with increasing time-scales, a one-line model approach becomes more and more favorable. However, if looking at decadal time-scales also sea-level rise will become important (Le Cozannet *et al.*, 2019).

5.3. Model selection

To assess uncertainty in the computations and obtain the highest level of information on the CSIs of interest, a trade-off must be made between effort (computation time, prediction horizon) and skill in predicting the particular CSI(s). A simpler model can be run more often, increasing the information obtained. However, if a single prediction has limited skill, the quality is lower, resulting in less information per simulation. This relation indicates an information optimum exists in this quality-quantity space for each CSI. Since performance measures can vary with a project's design and success definition, the model choice becomes a trade-off between optima for each CSI. As a result, a simpler model can lead to a higher level of information depending on the project and desired performance indicators.

A simple one-line model, as used in Chapter 3, has high computational efficiency, e.g., leads to a low computational time or allows evaluation of longer time scales. Model setup requires relatively little and accessible information (e.g., initial and boundary conditions can be derived from freely accessible sources such as satellite data and global wave models). Due to model description and input data, it is only skilled at predicting shoreline response and volume change. Also, the necessary data for uncertainty quantification is easily accessible, as it can be derived from satellite images. A more advanced one-line model (e.g., ShorelineS, Roelvink *et al.*, 2020) that includes dune building and erosive processes improves results at the HD (Roelvink *et al.*, 2024). However, it requires

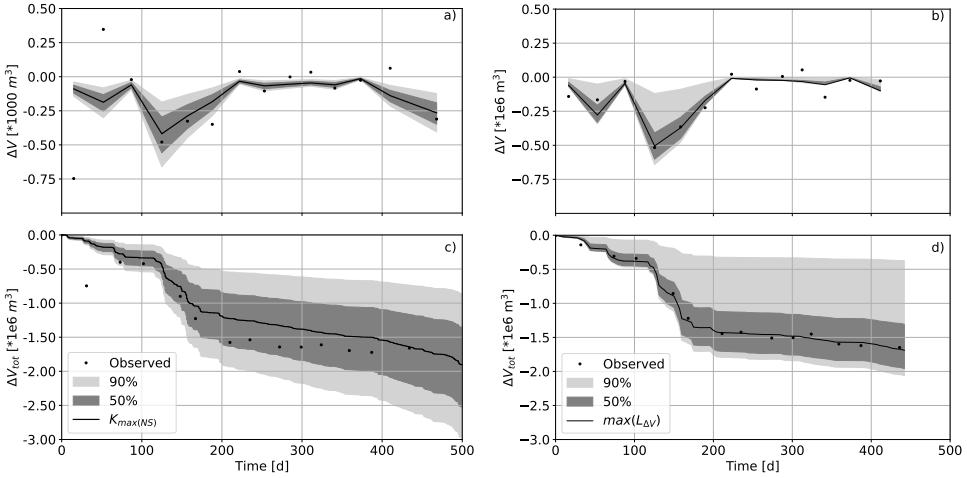

Figure 5.1.: Comparison of uncertainty bounds with the one-line and the coastal area model of respectively Chapter 3 and Chapter 4 for the first 12 months after placement of the SE. Volume change between consecutive surveys is predicted with a) the one-line model and b) the coastal area model. Total volume change since August 2011 predicted with c) the one-line model and d) the coastal area model (d). Grey shades indicate the 50 and 90% confidence interval of the posterior distributions, the black line the simulation with the highest likelihood, and the black dots the observed volume changes.

more input data, such as nearshore waves and cross-shore indicators, such as (initial) dune height or beach width. Also, validation and uncertainty quantification of the model requires more detailed data because the added processes add degrees of freedom to the model. On the performance side, these models probably have a higher skill at predicting beach width and can give more detail in the distribution of volume in the cross-shore. Coastal area models (e.g., Delft3D Lesser, 2009), on the other hand, are computationally less efficient. They require more detailed input data, such as high-resolution bathymetry data, and more effort in model setup, e.g., making multiple computational grids for wave propagation and morphodynamics and possible nested grids. Also, calibration and uncertainty quantification require more effort because of the many free model parameters, related degrees of freedom, and high computational times. On the performance side, these models can produce relatively high skill in each dimension or CSI. Nevertheless, these models are not perfect and miss processes that can be important for reproducing certain CSIs, such as aeolian transport, dune erosion, or 3D processes. At the cost of an even higher effort, at least dune building processes have been included (van Westen *et al.*, 2024). Yet, considering computational efficiency, it remains questionable whether assessing such a complicated series of models within a probabilistic framework is possible at this

point.

The trade-off that is part of this model selection is illustrated with a radar chart for uncertainty quantification in predictions of large-scale sandy interventions, Fig. 5.2. A chart with quality of prediction (performance) indicators on one side and effort indicators on the other. A skilled prediction will result in a high score for each performance indicator. In contrast, on the effort side, a high score indicates low computational costs, model preparation, and requirements for data availability to quantify uncertainty (with GLUE). A larger area covered by a model type means more information. More advanced models cover a larger area on the performance side. On the effort side of the graph, less complex models cover more area. But filling this out for the previously mentioned models shows that a different choice of model can result in a larger area, thus more information. It's worth noting that the model with the largest area may not always be the most informative for each CSI. For example, a simple one-line model may provide enough information when predicting volume. However, if both area and volume need to be predicted, a coastal area model may provide the highest level of information for these two CSIs combined. Generally, the type of model required in a probabilistic analysis will depend on the design of the large-scale sandy intervention and the related evolution of the CSI(s) of interest.

5.4. How to quantify uncertainty in future predictions?

To assess uncertainty in the predictions of the next large-scale sandy intervention, six steps are advised:

1. Define CSIs for the success of the project and the timescales of interest
2. Select appropriate model(s)
3. Define relevant sources of intrinsic and epistemic uncertainty
4. Define prior distributions of model parameters and variations in boundary conditions
5. Propagate priors through the model to arrive at apriori likelihoods of the CSIs
6. Update the likelihood when observations become available

The first step is considering the CSIs defining the project's success and the time scales of interest. It is important to do so before working out a model strategy and before model calibration because it can affect the strategy of choice and the importance of sources of uncertainty. Second, an appropriate model or model strategy that optimizes the information level for these CSIs should be chosen. This step is followed by an analysis of the intrinsic sources of uncertainty that might play a role for the large-scale intervention in question. For example, a nearby river may have varying sediment loads, fluctuations in wave forcing at the open coast, or varying wind-driven currents in a more enclosed location. In case of using data with lower accuracy (e.g., shoreline derived from satellite imagery) for uncertainty quantification, it is more elegant to assume observations

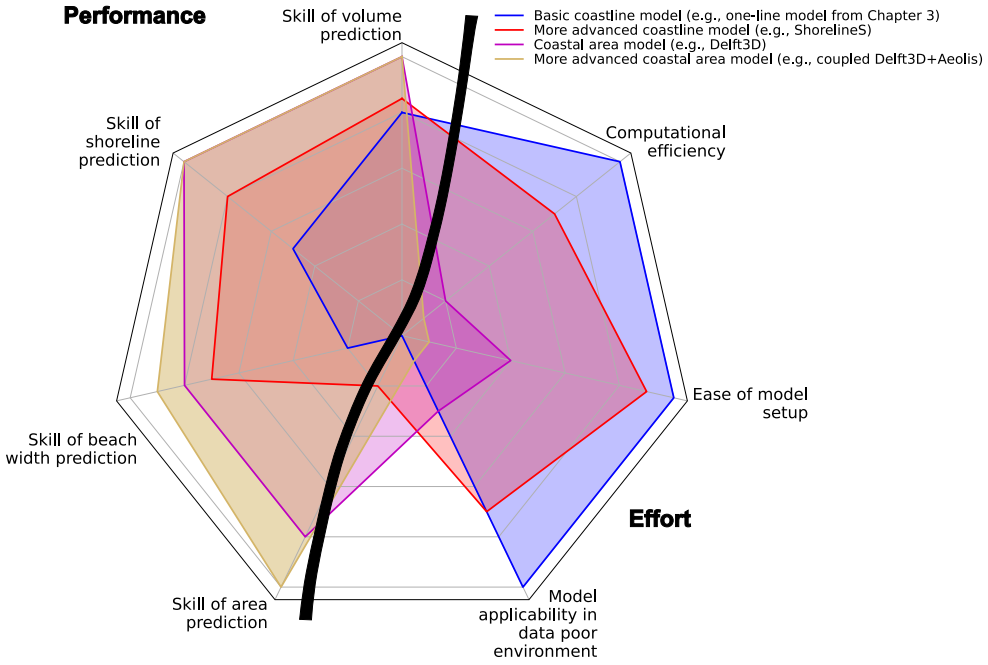

Figure 5.2.: Level of information trade-off between effort and quality for uncertainty quantification with different morphological models for assessment of large-scale sandy interventions.

as stochastic to account for observation errors. This requires an adjustment of the likelihood definition, but the methodology can remain basically the same. Next, prior distributions of model parameters and intrinsic sources of uncertainty should be defined. When there is (sufficiently long) observation data of environmental conditions available, this can be used to quantify the variations to be expected. Model parameters can be based on measurements of previous large-scale interventions with the GLUE method in case observations are available. When no data is available to use in the GLUE procedure, (global) sensitivity analysis (Saltelli *et al.*, 2008) is a valuable tool to find the critical variables that can lead to a variation in predictions. Note that a one-at-a-time sensitivity analysis will not suffice because of correlations between different sources of uncertainty. When no observations of environmental conditions are available, variability in forcing can be derived from global models (and nearshore translation). Priors of model parameters can be chosen based on past experience. Afterward, in step four, uncertainty can be quantified by utilizing these prior distributions to propagate them through the model and arrive at an apriori distribution of its output. Finally, in step five, Bayes theorem allows for updating these prior predictions with observations that come available after construction (e.g., Kroon *et*

al., 2017). This can lead to either an increase or decrease of uncertainty (W. E. Walker *et al.*, 2003), depending on how well observations match the apriori estimated likelihood.

5.5. How to manage uncertainty for large-scale sandy interventions?

The adaptability of sandy interventions is the reason to change coastal management strategies in light of uncertain expectations of sea level rise. An apparent downside is the increased uncertainty of using loose-placed sand as a building material in the coastal zone.

To overcome this disadvantage, it is advisable to use the results of a probabilistic volume change prediction of a large-scale nourishment, as described in paragraph 5.4, to feed a (semi-)probabilistic dune safety assessment to gather insight on the failure probability. In such an analysis, there will not be a minimum volume or profile to guarantee, only a minimum failure probability.

Furthermore, this thesis shows that uncertainties are most significant in the initial years after placement of large-scale sandy interventions. Yet, this model uncertainty can be reduced by updating the apriori likelihood with the observed changes in the first two or three years. In the case of a design, build, and maintenance contract, as was the case for the HD, it could be favorable to all parties to spread the initial maintenance risk over both the contractor and the contracting party and then reevaluate the expected maintenance after two or three years. In this way, the contractor is not responsible for disproportionate risks but is still motivated to design a solution that minimizes lifetime costs.

6

Conclusion

6.1. Conclusion

The objective of this thesis was to identify uncertainty in predictions of large-scale sandy interventions in the coastal zone and its effect on different coastal state indicators. Therefore we applied and validated a stochastic method for evaluating large-scale sandy interventions in the coastal zone. We did this by looking at two large Dutch interventions; the Sand Engine and the Hondsbossche Dunes mega-nourishments and we have used different types of morphological models in the stochastic framework. To achieve this goal, we have identified several research questions and provided their answers below.

How do various coastal state indicators evolve in the first years after the implementation of a large-scale sandy intervention?

The Hondsbossche Dunes project is a combined shoreface, beach, and dune nourishment of 35 million m^3 sand. The nourishment was built to replace the flood protection function of an old sea-dike while creating additional space for nature and recreation. To assess how coastal state indicators such as beach width and subaerial sediment volume evolve after placement of a large-scale nourishment we analyzed the evolution of this newly created sandy beach system in the first 5 years after placement. Nearly twenty topographic surveys are used to examine the redistribution of sediment volume in both the along and cross-shore directions and the adaptation of the post-nourishment profiles with initially wide beaches.

In the first years after implementation, large local volume changes up to 1000 m^3 per meter alongshore were observed. Yet, net volume losses in the 9 km coastal section were less than 5%, indicating that reworking was mostly local. The central part of the nourished site stands out as an erosive zone, with large (60 to 140 $m^3/m/y$) erosion. This erosion is predominantly in the subaqueous part of the profile and coincides with a shoreline retreat of about 80 m. Lateral coastal sections on the other hand show large accretion and a waterline migration of

around 30 m-seaward. The man-made cross-shore beach profile rapidly mimics the adjacent beaches, as the surfzone slope is adjusted within two winters to a similar slope.

The seaward sandy extension of the sea dike creates a significant coastline curvature. The observed net profile volume change is, at several sections of the nourishment, strongly correlated ($r^2 > 0.6$) with this planform curvature. In our observations, the local change in waterline position, ΔX_s, correlates well with the volume change in the full profile ΔV_p ($r^2 = 0.84$). Finding this strong correlation suggests that the use of one-line models is appropriate when predicting the volume and coastline change of mega-nourishments.

An important observation is that the subaerial and subaqueous parts of profiles display contrasting behavior in the first years after placement. The dune volume increases in the first years after implementation with 30 m^3/m/y; for many profiles, this net gain in volume is found regardless of the erosive trend in the lower part of the profile. The magnitude of the dune volume increase at the nourished site is three times higher than at the adjacent coast. This implies that the nourishment is bringing additional sediment volume above surge level, which is key to coastal safety.

As the dune foot migrates in the seaward direction and the shoreline moves landward, the beach width is reduced from two sides. The initially wide beaches (i.e., up to 225 m) are transformed in five years to about 100 m-wide, similar to adjacent beaches. The similarity in beach widths near the end of the five years investigated suggests that upcoming storm events may be able to erode sediment from the dunes, potentially reducing the excessive net growth of dune volume in the near future.

What is the relative importance of epistemic uncertainty versus intrinsic uncertainty?

We have included both intrinsic and epistemic uncertainty in a probabilistic framework, to investigate the relative importance of these uncertainties in the evolution of a sandy solution. To this end, we assessed a large-scale nourishment case with a one-line model in a probabilistic framework. In this framework, transport and volume loss are considered to be a function of random wave forcing (intrinsic uncertainty) and calibration settings (epistemic uncertainty). The variance of both stochastic variables are based on observations using the Sand Engine nourishment.

We show that confidence interval width and variance of predicted volume loss increase when allowing for model uncertainty. The confidence interval width and variance increase further (40%) if we not only recognize uncertainty in our model but also include a correlation (of $\rho = 0.5$) between model parameter settings and wave forcing. For the Sand Engine nourishment examined here, the contribution of model uncertainty to the variance of total volume loss is of the same order of magnitude as the contribution of wave climate variability after a 2.5-year simulation period, indicating that accounting for wave climate variability only, will

produce significant overconfidence in the results. Nevertheless, on a monthly time scale the fraction of variance attributed to wave climate variability is three times larger than that of model uncertainty, thus reducing the importance of model uncertainty in predicting initial nourishment development.

For multi-year time scales, model uncertainty will become the dominant contribution: more wave energy in one year is compensated by less wave energy in another, whereas model uncertainty is a cumulative effect that grows with each time step. Naturally, the relative importance of model uncertainty over wave climate variability depends on the complexity and skill of the model. In general, probabilistic frameworks favor less complex models to reduce computation time at the cost of a lower model skill. Consequently, increasing the relevance of model uncertainty assessment within the framework.

These findings imply that for coastal modelling purposes a dual approach should be considered, evaluating both epistemic and intrinsic uncertainties. Especially when forecasting large scale projects, with simplified models on a multi-year time scale, the uncertainty in model settings may be the principal source of uncertainty.

How is the uncertainty in predicting coastal state indicators developing over time and space?

The multi-dimensional parameter space of a coastal area model was explored to quantify model parameter uncertainty in predicted coastal state indicator values to assess how the uncertainty develops over time and space. We examined (spatial and temporal variations of) coastal state indicators bed level, sediment volume in budget areas, and shoreline position. Uncertainty was quantified with over 1000 Delft3D computations of the Sand Engine mega-nourishment's first 14-month evolution after construction.

An extensive set of model parameters is considered and systematically reduced to five key parameters. Uncertainty in these five model parameters translates into significant uncertainty in predicted coastal state indicator (CSI) values. Volume changes for sediment budget analyzes can vary by $75-85\%$ of predicted changes, predicted coastline position by $\pm$ 100 m, and bed level change confidence by up to 5 m (90% confidence values). The parameter uncertainty creates the widest confidence intervals at locations and moments when the changes in CSIs are most significant. For the Sand Engine, this translates into wide confidence intervals for bed level and coastline predictions in the spit area and around the -2m+NAP isobath. Wave forcing is important as 90% of this uncertainty is generated in the first seven high-energetic months. The resulting uncertainty distributions are non-Gaussian with an asymmetric shape to larger changes.

The suspended sediment transport scaling (f_{sus}), the breaker index (γ), and the grain size (d_{50}) contribute the most to the overall uncertainty in the Delft3D morphodynamic predictions. Because the investigated parameters are partially correlated, finding true optimal parameter settings or confirming the existence of a single optimal set is challenging.

Across the different parameter sets with very high and comparable skill, outcomes can be substantially different. For example, volume changes in the center of the SE can vary with $\pm 50\%$, and the tip of the spit can vary ± 500 m in alongshore position. This highlights the equifinality in the model: different results that are equally consistent with observations. Therefore, it is more valuable to focus on validation to reduce the number of highly skilled parameter sets rather than further optimization by increasing resolution around highly skilled parts of the parameter space, which could potentially lead to overfitting.

The model's sensitivity can vary significantly depending on the CSI of interest. For combined CSIs, the model is relatively insensitive to the wave energy dissipation coefficient (α_{rol}) and the dry cell erosion factor (θ_{sd}). However, θ_{sd} is a critical parameter in modeling the shoreline position. Furthermore, input likelihoods and optimal parameter settings may differ depending on the area of focus. Because of these sensitivities, the parameter values that yielded the best results may not be transportable, and there may be no single 'best' generic value for each parameter. Our results underline the importance of a good model calibration practice. Herein, the calibration area and parameter(s) of choice should be consistent with the CSIs to predict, as they can significantly impact the outcome of the (manual) calibration procedure.

6.2. Outlook

Several ongoing developments can stimulate uncertainty quantification in coastal morphology prediction practice. To increase the level of information, on the one hand, acceleration techniques, reduction of computation times and improved computation power can further improve the effort side of more complex models (e.g., Luijendijk *et al.*, 2018). In addition, surrogate models can come of use to combine the efficiency of simpler models with the detail of more complex models for the CSIs that don't follow from the simpler approach. However, this adds a step to the procedure of finding an appropriate surrogate (e.g., Berends *et al.*, 2019; Le Cozannet *et al.*, 2019). On the other hand, adding more descriptions of non-equilibrium processes to coastline models (e.g., Larson *et al.*, 2016; Marinho *et al.*, 2017) could improve the description of other CSIs than volume for such models, thereby improving the performance side, especially for the models that score high on the effort side. Appropriately resolving these processes empirically instead of process-based requires a lot of experience with the adaptation of large-scale sandy interventions and the specifics of the system they are placed in. This means that monitoring and evaluation are key to both advancing the available models and having data available for uncertainty quantification and updating.

Remote sensing (e.g., satellite imagery and unmanned aerial vehicles) can be a tool for monitoring. There is a lot of development in this field (e.g., Gawehn *et al.*, 2021; Vitousek *et al.*, 2023) that has the potential to provide high spatial and temporal resolution information at a lower cost than in-situ measurements. With more data available, tools based on patterns rather than physical processes

emerge, such as machine learning or artificial intelligence in general. Montaño *et al.* (2020) show that both traditional shoreline models and machine learning techniques could reproduce shoreline changes at an (undisturbed) New Zealand beach. However, a machine-learning approach requires a lot of data. Something that is not often available in coastal morphology in general, but especially not in the case of large-scale sandy interventions. This means that using artificial intelligence to predict system behavior after significant disturbances, such as large-scale sandy interventions, will be challenging for now.

The radar chart (Fig. 5.2) is only a qualitative tool to select a model for uncertainty quantification. In statistical modeling, criteria that maximize the simulation likelihood but penalize the number of parameters are used. Examples of such criteria include the Akaike information criterion (AIC) (Akaike, 1974) and the Bayesian Information Criterion (BIC) (Schwarz, 1978). Such criteria are formulated to prevent overfitting because allowing for more degrees of freedom inherently comes with a higher likelihood. However, in case of overfitting, extra parameters can reduce the model's predictive capacity. In the case of process-based models, it could be argued that the penalty for adding additional parameters should be lower because there is a physical reason for allowing more degrees of freedom. However, in many cases, added coefficients have little physical meaning left to them as they are used as aggregated adjustment buttons. Therefore, developing a similar criterion to make the selection procedure more quantitative could be an interesting path for future research.

Bibliography

Akaike, H. (1974). A new look at the statistical model identification. *IEEE Transactions on Automatic Control*, *19*(6), 716–723. https://doi.org/10.1109/TAC.1974.1100705

Antolínez, J. A. A., Méndez, F. J., Camus, P., Vitousek, S., González, E. M., Ruggiero, P., & Barnard, P. (2016). A multiscale climate emulator for longterm morphodynamics (MUSCLE-morpho). *Journal of Geophysical Research: Oceans*, *121*, 775–791. https://doi.org/10.1002/2015JC011107

Armaroli, C., Grottoli, E., Harley, M. D., & Ciavola, P. (2013). Beach morphodynamics and types of foredune erosion generated by storms along the emilia-romagna coastline, italy. https://doi.org/10.1016/j.geomorph.2013.04.034

Arriaga, J., Rutten, J., Ribas, F., Falqués, A., & Ruessink, G. (2017). Modeling the long-term diffusion and feeding capability of a mega-nourishment. *Coastal Engineering*, *121*(December 2016), 1–13. https://doi.org/10.1016/j.coastaleng.2016.11.011

Ashton, A. D., & Murray, A. B. (2006). High-angle wave instability and emergent shoreline shapes : 1 . Modeling of sand waves , flying spits , and capes. *Journal of Geophysical Research*, *111*(October 2005), 1–19. https://doi.org/10.1029/2005JF000422

Athanasiou, P., van Dongeren, A., Giardino, A., Vousdoukas, M., Antolinez, J. A., & Ranasinghe, R. (2021). A clustering approach for predicting dune morphodynamic response to storms using typological coastal profiles: A case study at the dutch coast. *Frontiers in Marine Science*, *8*. https://doi.org/10.3389/fmars.2021.747754

Baar, A. W., Boechat Albernaz, M., van Dijk, W. M., & Kleinhans, M. G. (2019). Critical dependence of morphodynamic models of fluvial and tidal systems on empirical downslope sediment transport. *Nature Communications*, *10*(1). https://doi.org/10.1038/s41467-019-12753-x

Baart, F. (2013). *Confidence in coastal forecasts* (Doctoral dissertation). Delft University of Technology. https://doi.org/10.1017/CBO9781107415324.004

Bae, H., Do, K., Kim, I., & Chang, S. (2022). Proposal of parameter range that offered optimal performance in the coastal morphodynamic model (xbeach) through glue. *Journal of Ocean Engineering and Technology*, *36*, 251–269. https://doi.org/10.26748/ksoe.2022.013

Baquerizo, A., & Losada, M. A. (2008). Human interaction with large scale coastal morphological evolution. an assessment of the uncertainty. *Coastal Engineering*, *55*(7-8), 569–580. https://doi.org/10.1016/j.coastaleng.2007.10.004

Bauer, B. O., Davidson-Arnott, R. G. D., Hesp, P. A., Namikas, S. L., Ollerhead, J., & Walker, I. J. (2009). Aeolian sediment transport on a beach: Surface moisture, wind fetch, and mean transport. *Geomorphology*, *105*(1-2), 106–116.

Benedet, L., Dobrochinski, J. P., Walstra, D. J., Klein, A. H., & Ranasinghe, R. (2016). A morphological modeling study to compare different methods of wave climate schematization and evaluate strategies to reduce erosion losses from a beach nourishment project. *Coastal Engineering*, *112*, 69–86. https://doi.org/10.1016/j.coastaleng.2016.02.005

Berends, K. D., Scheel, F., Warmink, J. J., de Boer, W. P., Ranasinghe, R., & Hulscher, S. J. (2019). Towards efficient uncertainty quantification with high-resolution morphodynamic models: A multifidelity approach applied to channel sedimentation. *Coastal Engineering*, *152*. https://doi.org/10.1016/j.coastaleng.2019.103520

Beven, K., & Binley, A. (1992). The future of distributed models: Model calibration and uncertainty prediction. *Hydrological Processes*, *6*(3), 279–298. https://doi.org/10.1002/hyp.3360060305

Beven, K., & Binley, A. (2014). GLUE: 20 years on. *Hydrological Processes*, *28*(24), 5897–5918. https://doi.org/10.1002/hyp.10082

Beven, K. (1993). Prophecy, reality and uncertainty in distributed hydrological modelling. *Advances in Water Resources*, *16*, 41–51. https://doi.org/10.1016/0309-1708(93)90028-E

Beven, K. (2009). *Environmental Modelling: An Uncertain Future?* CRC Press.

Bezzi, A., Fontolan, G., Nordstrom, K. F., Carrer, D., & Jackson, N. L. (2009). Beach nourishment and foredune restoration: Practices and constraints along the venetian shoreline, italy. *Journal of Coastal Research*, 287–291.

Bodde, W., McCall, R., Jansen, M., van den Berg, A., & Roelvink, J. (2017). Long-term morphological modelling: combining storm impact and daily conditions in an integrated modeling framework. *Coastal Dynamics 2017*, (5), 1809–1820.

Bosboom, J., Reniers, A. J., & Luijendijk, A. P. (2014). On the perception of morphodynamic model skill. *Coastal Engineering*, *94*, 112–125. https://doi.org/10.1016/j.coastaleng.2014.08.008

Brand, E., Ramaekers, G., & Lodder, Q. (2022). Dutch experience with sand nourishments for dynamic coastline conservation – an operational overview. *Ocean and Coastal Management*, *217*. https://doi.org/10.1016/j.ocecoaman.2021.106008

Bridges, T. S., Bourne, E. M., King, J. K., Kuzmitski, H. K., Moynihan, E. B., & Suedel, B. C. (2018). *Engineering with Nature: an atlas*. U.S. Army Engineer Research; Development Center. https://doi.org/10.21079/11681/27929

Briere, C., Giardino, A., & van der Werf, J. (2011). Morphological modeling of bar dynamics with delft3d: The quest for optimal free parameter settings using an automatic calibration technique. *Coastal Engineering Proceedings: sediment*, *1*(32), 1–12.

Browder, A. E., & Dean, R. G. (2000). Monitoring and comparison to predictive models of the perdido key beach nourishment project, florida, usa. *Coastal*

Engineering, *39*, 173–191. https://doi.org/10.1016/S0378-3839(99)00057-5

Bruun, P. (1954). *Coast Erosion and the Development of Beach Profiles*. Beach Erosion Board.

Callaghan, D. P., Nielsen, P., Short, A., & Ranasinghe, R. (2008). Statistical simulation of wave climate and extreme beach erosion. *Coastal Engineering*, *55*(5), 375–390. https://doi.org/10.1016/j.coastaleng.2007.12.003

Callaghan, D. P., Ranasinghe, R., & Roelvink, D. (2013). Probabilistic estimation of storm erosion using analytical, semi-empirical, and process based storm erosion models. *Coastal Engineering*, *82*, 64–75. https://doi.org/10.1016/j.coastaleng.2013.08.007

Campolongo, F., Cariboni, J., & Saltelli, A. (2007). An effective screening design for sensitivity analysis of large models. *Environmental Modelling and Software*, *22*, 1509–1518. https://doi.org/10.1016/j.envsoft.2006.10.004

Chang, J. I., & Yoon, S. (2016). The economic benefit of coastal erosion control in korea. *Journal of Coastal Research*, *1*, 1317–1321. https://doi.org/10.2112/SI75-264.1

Chataigner, T., Yates, M. L., Dantec, N. L., Harley, M. D., Splinter, K. D., & Goutal, N. (2022). Sensitivity of a one-line longshore shoreline change model to the mean wave direction. *Coastal Engineering*, *172*. https://doi.org/10.1016/j.coastaleng.2021.104025

Cohn, N., Ruggiero, P., de Vries, S., & Kaminsky, G. M. (2018). New insights on coastal foredune growth: The relative contributions of marine and aeolian processes. *Geophysical Research Letters*, *45*(10), 4965–4973. https://doi.org/10.1029/2018GL077836

Cohn, N., Ruggiero, P., García-Medina, G., Anderson, D., Serafin, K. A., & Biel, R. (2019). Environmental and morphologic controls on wave-induced dune response. *Geomorphology*, *329*, 108–128. https://doi.org/10.1016/j.geomorph.2018.12.023

Cooley, S., Schoeman, D., Bopp, L., Boyd, P., Donner, S., Ghebrehiwet, D., Ito, S.-I., Kiessling, W., Martinetto, P., Ojea, E., Racault, M.-F., Rost, B., & Skern-Mauritzen, M. (2022). Oceans and coastal ecosystems and their services. In H.-O. Pörtner, D. Roberts, M. Tignor, E. Poloczanska, K. Mintenbeck, A. Alegría, M. Craig, S. Langsdorf, S. Löschke, V. Möller, A. Okem & B. Rama (Eds.), *Climate change 2022 – impacts, adaptation and vulnerability* (pp. 379–550). Cambridge University Press, Cambridge, UK; New York, NY, USA. https://doi.org/10.1017/9781009325844.005

Cotton, I., Forster, J., Lorenzoni, I., & Tolhurst, T. J. (2022). Understanding perceived effectiveness of a novel coastal management project: The case of the bacton-walcott sandscaping scheme, uk. *Frontiers in Marine Science*, *9*. https://doi.org/10.3389/fmars.2022.1028819

Dabees, M., & Kamphuis, J. W. (1999). Oneline, a numerical model for shoreline change. *Coastal Engineering 1998*, 2668–2681.

D'Anna, M., Idier, D., Castelle, B., Vitousek, S., & Cozannet, G. L. (2021). Reinterpreting the Bruun Rule in the Context of Equilibrium Shoreline Models.

Journal of Marine Science and Eng., *9*(974). https://doi.org/10.3390/jmse9090974

Davidson, M. A., Turner, I. L., Splinter, K. D., & Harley, M. D. (2017). Annual prediction of shoreline erosion and subsequent recovery. *Coastal Engineering*, *130*, 14–25. https://doi.org/10.1016/j.coastaleng.2017.09.008

Davidson, M. A., Koningsveld, M. V., de Kruif, A., Rawson, J., Holman, R., Lamberti, A., Medina, R., Kroon, A., & Aarninkhof, S. (2007). The coastview project: Developing video-derived coastal state indicators in support of coastal zone management. *Coastal Engineering*, *54*, 463–475. https://doi.org/10.1016/j.coastaleng.2007.01.007

Dean, R. G. (1991). Equilibrium beach profiles: characteristics and applications. *Journal of Coastal Research*, *7*(1), 53–84.

Dean, R. G., & Yoo, C.-H. (1992). Beach-Nourishment Performance Predictions. *Journal of Waterway, Port, Coastal, and Ocean Engineering*, *118*(6), 567–586.

Dean, R. G. (2002). *Beach nourishment: Theory and practice*. World Scientific.

Deltares. (2011). *Wave look-up table: Building with Nature* (tech. rep.). Deltares.

Deltares. (2019, May 5). *Delft3d flow user manual (3.15)*. Deltares.

den Heijer, C. (2013). *The role of bathymetry, wave obliquity and coastal curvature in dune erosion prediction* (Doctoral dissertation). Delft University of Technology.

den Heijer, C., Baart, F., & van Koningsveld, M. (2012). Assessment of dune failure along the Dutch coast using a fully probabilistic approach. *Geomorphology*, *143-144*(March), 95–103. https://doi.org/10.1016/j.geomorph.2011.09.010

de Schipper, M. A., de Vries, S., Ruessink, G., de Zeeuw, R. C., Rutten, J., van Gelder-Maas, C., & Stive, M. J. F. (2016). Initial spreading of a mega feeder nourishment: Observations of the Sand Engine pilot project. *Coastal Engineering*, *111*, 23–38. https://doi.org/10.1016/j.coastaleng.2015.10.011

de Schipper, M. A., Ludka, B. C., Raubenheimer, B., Luijendijk, A. P., & Schlacher, T. A. (2021). Beach nourishment has complex implications for the future of sandy shores. *Nature Reviews Earth & Environment*, *2*, 70–84. https://doi.org/10.1038/s43017-020-00109-9

Dessai, S., Hulme, M., Lempert, R., & Pielke Jr, R. (2009). Climate prediction: A limit to adaptation. In W. N. Adger, I. Lorenzoni & K. L. O'Brien (Eds.), *Adapting to climate change: Thresholds, values, governance* (pp. 64–78). Cambridge University Press Cambridge.

de Vriend, H. J., van Koningsveld, M., Aarninkhof, S. G. J., de Vries, M. B., & Baptist, M. J. (2015). Sustainable hydraulic engineering through building with nature. *Journal of Hydro-Environment Research*, *9*(2), 159–171. https://doi.org/10.1016/j.jher.2014.06.004

de Vriend, H. (1987). 2DH Mathematical Modelling of Morphological Evolutions in Shallow Water. *Coastal Engineering*, *11*, 1–27.

de Vries, S., Southgate, H. N., Kanning, W., & Ranasinghe, R. (2012). Dune behavior and aeolian transport on decadal timescales. *Coastal Engineering*, *67*, 41–53. https://doi.org/10.1016/j.coastaleng.2012.04.002

de Vries, S., van Thiel de Vries, J. S., van Rijn, L. C., Arens, S. M., & Ranasinghe, R. (2014a). Aeolian sediment transport in supply limited situations. *Aeolian Research*, *12*, 75–85. https://doi.org/10.1016/j.aeolia.2013.11.005

de Vries, S., Arens, S., De Schipper, M., & Ranasinghe, R. (2014b). Aeolian sediment transport on a beach with a varying sediment supply. *Aeolian Research*, *15*, 235–244.

Efron, B. (1979). Bootstrap methods: Another look at the jackknife. *The annals of statistics*, *7*(1), 1–26. https://doi.org/10.1214/aos/1176344552

Elko, N. A., & Wang, P. (2007). Immediate profile and planform evolution of a beach nourishment project with hurricane influences. *Coastal Engineering*, *54*(1), 49–66. https://doi.org/10.1016/j.coastaleng.2006.08.001

Galiforni Silva, F., Wijnberg, K. M., de Groot, A. V., & Hulscher, S. J. (2019). The effects of beach width variability on coastal dune development at decadal scales. *Geomorphology*, *329*, 58–69. https://doi.org/10.1016/j.geomorph.2018.12.012

Gawehn, M., Vries, S. D., & Aarninkhof, S. (2021). A self-adaptive method for mapping coastal bathymetry on-the-fly from wave field video. *Remote Sensing*, *13*. https://doi.org/10.3390/rs13234742

Glasserman, P. (2003). *Monte carlo methods in financial engineering* (Vol. 53). Springer. https://doi.org/10.1007/978-0-387-21617-1

Gopalakrishnan, S., Smith, M. D., Slott, J. M., & Murray, A. B. (2011). The value of disappearing beaches: A hedonic pricing model with endogenous beach width. *Journal of Environmental Economics and Management*, *61*, 297–310. https://doi.org/10.1016/j.jeem.2010.09.003

Griggs, G. B., & Patsch, K. (2018). Natural changes and human impacts on the sand budgets and beach widths of the zuma and santa monica littoral cells, southern california. *Shore and Beach*, *86*, 1–14.

Grunnet, N. M., Walstra, D. J. R., & Ruessink, B. G. (2004). Process-based modelling of a shoreface nourishment. *Coastal Engineering*, *51*, 581–607. https://doi.org/10.1016/j.coastaleng.2004.07.016

Hallermeier, R. J. (1981). A profile zonation for seasonal sand beaches from wave climate. *Coastal Engineering*, *4*, 253–277.

Hallermeier, R. J. (1983). Sand transport limits in coastal structure design. *Proceedings of Coastal Sturctures '83*, 703–716.

Hanson, H. (1988). Genesis-A Generalized Shoreline Change Numerical Model. *Journal of Coastal Research*, *5*(1), 1–27.

Harley, M. D., Valentini, A., Armaroli, C., Perini, L., Calabrese, L., & Ciavola, P. (2016). Can an early-warning system help minimize the impacts of coastal storms? a case study of the 2012 halloween storm, northern italy. *Natural Hazards and Earth System Sciences*, *16*, 209–222. https://doi.org/10.5194/nhess-16-209-2016

Hawkins, E., & Sutton, R. (2009). The potential to narrow uncertainty in regional climate predictions. *Bulletin of the American Meteorological Society*, *19*(8), 1095–1107. https://doi.org/10.1175/2009BAMS2607.1

Hawkins, E., & Sutton, R. (2011). The potential to narrow uncertainty in projections of regional precipitation change. *Climate Dynamics*, *37*(1-2), 407–418. https://doi.org/10.1007/s00382-010-0810-6

Hendrickx, G. G., Antolínez, J. A., & Herman, P. M. (2023). Predicting the response of complex systems for coastal management. *Coastal Engineering*, 104289. https://doi.org/10.1016/j.coastaleng.2023.104289

Hinkel, J., Aerts, J. C., Brown, S., Jiménez, J. A., Lincke, D., Nicholls, R. J., Scussolini, P., Sanchez-Arcilla, A., Vafeidis, A., & Addo, K. A. (2018). The ability of societies to adapt to twenty-first-century sea-level rise. *Nature Climate Change*, *8*, 570–578. https://doi.org/10.1038/s41558-018-0176-z

Hoonhout, B., & de Vries, S. (2017). Aeolian sediment supply at a mega nourishment. *Coastal Engineering*, *123*(March), 11–20. https://doi.org/10.1016/j.coastaleng.2017.03.001

Hopkins, J., Elgar, S., & Raubenheimer, B. (2018). Storm impact on morphological evolution of a sandy inlet. *Journal of Geophysical Research: Oceans*, *123*, 5751–5762. https://doi.org/10.1029/2017JC013708

Huisman, B. J. A., de Schipper, M. A., & Ruessink, B. G. (2016). Sediment sorting at the Sand Motor at storm and annual time scales. *Marine Geology*, *381*, 209–226. https://doi.org/10.1016/j.margeo.2016.09.005

Huisman, B. J. A., Walstra, D.-J. R., Radermacher, M., Schipper, D. M. A., & Ruessink, G. B. (2019). Observations and Modelling of Shoreface Nourishment Behaviour. *Journal of Marine Science and Eng.*, *7*(59). https://doi.org/10.3390/jmse7030059

Hurst, M. D., Barkwith, A., Ellis, M. A., Thomas, C. W., & Murray, A. B. (2015). Exploring the sensitivities of crenulate bay shorelines to wave climates using a new vector-based one-line model. *Journal of Geophysical Research F: Earth Surface*, *120*(12), 2586–2608. https://doi.org/10.1002/2015JF003704

Ibaceta, R., Splinter, K. D., Harley, M. D., & Turner, I. L. (2022). Improving multidecadal coastal shoreline change predictions by including model parameter non-stationarity. *Frontiers in Marine Science*, *9*. https://doi.org/10.3389/fmars.2022.1012041

IPCC Working Group I. (2013). *Working group i contribution to the ipcc fifth assessment report (ar5), climate change 2013: The physical science basis. chapter 11: Near-term climate change: Projections and predictability*.

Itzkin, M., Moore, L. J., Ruggiero, P., Hacker, S. D., & Biel, R. G. (2021). The relative influence of dune aspect ratio and beach width on dune erosion as a function of storm duration and surge level. *Earth Surface Dynamics*, *9*, 1223–1237. https://doi.org/10.5194/esurf-9-1223-2021

Itzkin, M., Moore, L. J., Ruggiero, P., Hovenga, P. A., & Hacker, S. D. (2022). Combining process-based and data-driven approaches to forecast beach and dune change. *Environmental Modelling & Software*, *153*, 105404. https://doi.org/10.1016/j.envsoft.2022.105404

Iwanaga, T., Usher, W., & Herman, J. (2022). Toward SALib 2.0: Advancing the accessibility and interpretability of global sensitivity analyses. *Socio-*

Environmental Systems Modelling, *4*(1), 1–15. https://doi.org/10.18174/sesmo.18155

Jacques, J., Lavergne, C., & Devictor, N. (2006). Sensitivity analysis in presence of model uncertainty and correlated inputs. *Reliability Engineering and System Safety*, *91*(10-11), 1126–1134. https://doi.org/10.1016/j.ress.2005.11.047

Jäger, W. S., & Nápoles, O. M. (2017). A vine-copula model for time series of significant wave heights and mean zero-crossing periods in the North Sea. *Journal of Risk and Uncertainty in Engineering Systems, Part A: Civil Engineering*, *3*(4), 1–25. https://doi.org/10.1061/AJRUA6.0000917

Jamous, M., Marsooli, R., & Ayyad, M. (2023). Global sensitivity and uncertainty analysis of a coastal morphodynamic model using polynomial chaos expansions. *Environmental Modelling and Software*, *160*. https://doi.org/10.1016/j.envsoft.2022.105611

Kamphuis, J. W. (1991). Alongshore Sediment Transport Rate. *Journal of Waterway, Port, Coastal, and Ocean Engineering*, *117*(6), 624–640. https://doi.org/10.1061/(ASCE)0733-950X(1991)117:6(624)

Kasprak, A., Bransky, N. D., Sankey, J. B., Caster, J., & Sankey, T. T. (2019). The effects of topographic surveying technique and data resolution on the detection and interpretation of geomorphic change. *Geomorphology*, *333*, 1–15. https://doi.org/10.1016/j.geomorph.2019.02.020

Khare, Y., Martinez, C. J., Muñoz-Carpena, R., Bottcher, A., & James, A. (2019). Effective global sensitivity analysis for high-dimensional hydrologic and water quality models. *Journal of Hydrologic Engineering*, *24*, 04018057. https://doi.org/10.1061/(asce)he.1943-5584.0001726

Kiureghian, A. D., & Ditlevsen, O. (2008). Aleatory or epistemic? does it matter? *Structural Safety*, *31*, 105–112. https://doi.org/10.1016/j.strusafe.2008.06.020

Kroon, A., de Schipper, M. A., den Heijer, C., Aarninkhof, S. G. J., & van Gelder, P. H. A. J. M. (2017). Uncertainty assessment in coastal morphology prediction with a bayesian network. *Coastal Dynamics Proceedings*, (254), 1909–1920.

Kroon, A., van Leeuwen, B., Walstra, D., & Loman, G. (2016). Dealing with uncertainties in long-term predictions of a coastal nourishment. *Coastal Management: Changing Coast, Changing Climate, Changing Minds - Proceedings of the International Conference*, 9–18. https://doi.org/10.1680/cm.61149.009

Kroon, A., de Schipper, M. A., van Gelder, P. H. A. J. M., & Aarninkhof, S. G. J. (2019). Quantification of model uncertainty in lifetime predictions of nourishments. *Coastal Sediments 2019*, 338–346. https://doi.org/10.1142/9789811204487_0032

Kroon, A., de Schipper, M. A., van Gelder, P. H., & Aarninkhof, S. G. (2020). Ranking uncertainty: Wave climate variability versus model uncertainty in probabilistic assessment of coastline change. *Coastal Engineering*, *158*, 103673. https://doi.org/10.1016/j.coastaleng.2020.103673

Kucherenko, S., Albrecht, D., & Saltelli, A. (2015). *Exploring multi-dimensional spaces: A comparison of latin hypercube and quasi monte carlo sampling techniques*. arXiv. https://doi.org/10.48550/ARXIV.1505.02350

Larson, M., Hanson, H., Kraus, N. C., & Newe, J. (1999). Short- and long- term responses of beach fills determined by eof analysis. *J. Waterway, Port, Coastal, Ocean Eng.*, *125*, 285–293.

Larson, M., Palalane, J., Fredriksson, C., & Hanson, H. (2016). Simulating cross-shore material exchange at decadal scale. theory and model component validation. *Coastal Engineering*, *116*, 57–66. https://doi.org/10.1016/j.coastaleng.2016.05.009

Le Cozannet, G., Bulteau, T., Castelle, B., Ranasinghe, R., Wöppelmann, G., Rohmer, J., Bernon, N., Idier, D., Louisor, J., & Salas-y-Mélia, D. (2019). Quantifying uncertainties of sandy shoreline change projections as sea level rises. *Scientific Reports*, *9*(42), 1–11. https://doi.org/10.1038/s41598-018-37017-4

Lesser, G. (2009). *An Approach to Medium-term Coastal Morphological Modelling* (Doctoral dissertation). Delft University of Technology. http://www.narcis.nl/publication/RecordID/oai:tudelft.nl:uuid:62caa573-4fc0-428e-8768-0aa47ab612a9

Liu, G., Cai, F., Qi, H., Zhu, J., Lei, G., Cao, H., & Zheng, J. (2019). A method to nourished beach stability assessment: The case of China. *Ocean and Coastal Management*, *177*(178), 166–178. https://doi.org/10.1016/j.ocecoaman.2019.05.015

Liu, Z., Cui, B., & He, Q. (2016). Shifting paradigms in coastal restoration: Six decades' lessons from china. *Science of the Total Environment*, *566-567*, 205–214. https://doi.org/10.1016/j.scitotenv.2016.05.049

Ludka, B. C., Gallien, T. W., Crosby, S. C., & Guza, R. T. (2016). Mid-el niño erosion at nourished and unnourished southern california beaches. *Geophysical Research Letters*, *43*, 4510–4516. https://doi.org/10.1002/2016GL068612

Ludka, B. C., Guza, R. T., & O'Reilly, W. C. (2018). Nourishment evolution and impacts at four southern California beaches: A sand volume analysis. *Coastal Engineering*, *136*(February), 96–105. https://doi.org/10.1016/j.coastaleng.2018.02.003

Luijendijk, A. P., Ranasinghe, R., de Schipper, M. A., Huisman, B. A., Swinkels, C. M., Walstra, D. J. R., & Stive, M. J. F. (2017a). The initial morphological response of the Sand Engine: A process-based modelling study. *Coastal Engineering*, *119*, 1–14. https://doi.org/10.1016/j.coastaleng.2016.09.005

Luijendijk, A. P., de Schipper, M. A., & Ranasinghe, R. (2019). Morphodynamic Acceleration Techniques for Multi-Timescale Predictions of Complex Sandy Interventions. *Journal of Marine Science and Engineering*, *7*(3), 78. https://doi.org/10.3390/jmse7030078

Luijendijk, A. P., Hagenaars, G., Ranasinghe, R., Baart, F., Donchyts, G., & Aarninkhof, S. (2018). The State of the World's Beaches. *Scientific Reports*, *8*(1), 1–11. https://doi.org/10.1038/s41598-018-24630-6

Luijendijk, A. P., Velhorst, R., Hoonhout, B., de Vries, S., & Ranasinghe, R. (2017b). Integrated Modelling of the Morphological Evolution of the Sand Engine

Mega-Nourishment. *Proceedings of Coastal Dynamics 2017*, (June), 1874–1885. https://doi.org/10.1089/end.2017.0062

Ly, N. T. H., & Hoan, N. T. (2018). Determination of Nearshore Wave Climate using a Transformation Matrix from Offshore Wave Data. *Journal of Coastal Research*, *81*(sp1), 14. https://doi.org/10.2112/si81-003.1

Mankin, J. S., Lehner, F., Coats, S., & McKinnon, K. A. (2020). The value of initial condition large ensembles to robust adaptation decision-making. *Earth's Future*, *8*, e2012EF001610. https://doi.org/10.1029/2020EF001610

Marinho, B., Coelho, C., Larson, M., & Hanson, H. (2017). Simulating Cross-Shore Evolution Towards Equilibrium of Different Beach Nourishment Schemes. *Coastal Dynamics*, (121), 1732–1746.

Marinho, B., Coelho, C., Larson, M., & Hanson, H. (2018). Short- and long-term responses of nourishments: Barra-vagueira coastal stretch, portugal. *Journal of Coastal Conservation*, *22*, 475–489. https://doi.org/10.1007/s11852-017-0533-5

Martínez, M. L., Intralawan, A., Vázquez, G., Pérez-Maqueo, O., Sutton, P., & Landgrave, R. (2007). The coasts of our world: Ecological, economic and social importance. *Ecological Economics*, *63*, 254–272. https://doi.org/10.1016/J.ECOLECON.2006.10.022

Mil-Homens, J. (2016). *Longshore sediment transport bulk formulas and process based models* (Doctoral dissertation). Delft University of Technology.

Montaño, J., Coco, G., Antolínez, J. A., Beuzen, T., Bryan, K. R., Cagigal, L., Castelle, B., Davidson, M. A., Goldstein, E. B., Ibaceta, R., Idier, D., Ludka, B. C., Masoud-Ansari, S., Méndez, F. J., Murray, A. B., Plant, N. G., Ratliff, K. M., Robinet, A., Rueda, A., … Vos, K. (2020). Blind testing of shoreline evolution models. *Scientific Reports*, *10*, 1–10. https://doi.org/10.1038/s41598-020-59018-y

Morgan, M. G., Henrion, M., & Small, M. J. (1990). *Uncertainty : a guide to dealing with uncertainty in quantitative risk and policy analysis*. Cambridge University Press.

Morris, M. D. (1991). Factorial plans for preliminary computational experiments. *Technometrics*, *33*(2), 161–174.

Moulton, M. A., Hesp, P. A., Miot da Silva, G., Keane, R., & Fernandez, G. B. (2021). Surfzone-beach-dune interactions along a variable low wave energy dissipative beach. *Marine Geology*, *435*(January), 106438. https://doi.org/10.1016/j.margeo.2021.106438

Mulder, J. P., & Tonnon, P. K. (2011). " Sand Engine " : Background and Design of a Mega-Nourishment Pilot in the Netherlands. *Coastal Engineering Proceedings*, *1*(32), 35. https://doi.org/10.9753/icce.v32.management.35

Nash, J. E., & Sutcliffe, J. V. (1970). River Flow Forecasting Through Conceptual Models Part I-a Discussion of Principles*. *Journal of Hydrology*, *10*, 282–290. https://doi.org/10.1016/0022-1694(70)90255-6

Nicholls, R. J., & Cazenave, A. (2010). Sea-level rise and its impact on coastal zones. *Science*, *328*(5985), 1517–1520. https://doi.org/10.1126/science.1185782

Oppenheimer, M., Glavovic, B., Hinkel, J., van de Wal, R., Magnan, A., Abd-Elgawad, A., Cai, R., Cifuentes-Jara, M., DeConto, R., Ghosh, T., Hay, J., Isla, F., Marzeion, B., Meyssignac, B., & Sebesvari, Z. (2019). Sea level rise and implications for low-lying islands, coasts and communities. In H.-O. Pörtner, D. Roberts, V. Masson-Delmotte, P. Zhai, M. Tignor, E. Poloczanska, K. Mintenbeck, A. Alegría, M. Nicolai, A. Okem, J. Petzold, B. Rama & N. Weyer (Eds.), *IPCC special report on the ocean and cryosphere in a changing climate* (pp. 321–445). Cambridge University Press, Cambridge, UK; New York, NY, USA. https://doi.org/10.1017/9781009157964.006

Oreskes, N., Shrader-Frechette, K., & Belitz, K. (1994). Verification, validation, and confirmation of numerical models in the earth sciences. *Science*, *263*, 641–646. https://doi.org/10.1126/science.263.5147.641

Palinkas, C. M., Orton, P., Hummel, M. A., Nardin, W., Sutton-Grier, A. E., Harris, L., Gray, M., Li, M., Ball, D., Burks-Copes, K., Davlasheridze, M., Schipper, M. D., George, D. A., Halsing, D., Maglio, C., Marrone, J., McKay, S. K., Nutters, H., Orff, K., … Williams, T. (2022). Innovations in coastline management with natural and nature-based features (NNBF): Lessons learned from three case studies. *Frontiers in Built Environment*, *8*. https://doi.org/10.3389/fbuil.2022.814180

Park, J.-Y., Gayes, P. T., & Wells, J. T. (2009). Monitoring beach renourishment along the sediment-starved shoreline of grand strand, south carolina. *Source: Journal of Coastal Research*, *25*, 336–349. https://about.jstor.org/terms

Payo, A., Baquerizo, A., & Losada, M. (2002). One-line model with time dependent boundary conditions. *ICCE 2002*, 3046–3052. https://doi.org/10.1142/9789812791306

Payo, A., Baquerizo, A., & Losada, M. A. (2008). Uncertainty assessment: Application to the shoreline. *Journal of Hydraulic Research*, *46*(sup1), 96–104. https://doi.org/10.1080/00221686.2008.9521944

Pelnard-Considère, R. (1957). Essai de théorie de l'évolution des formes de rivage en plages de sable et de galets. *Journées de l'hydraulique*, *4*(1), 289–298.

Perk, L., van Rijn, L., Koudstaal, K., & Fordeyn, J. (2019). A rational method for the design of sand dike/dune systems at sheltered sites; wadden sea coast of texel, the netherlands. *Journal of Marine Science and Engineering*, *7*. https://doi.org/10.3390/jmse7090324

Plant, N. G., Holland, K. T., & Puleo, J. A. (2002). Analysis of the scale of errors in nearshore bathymetric data. *Marine Geology*, *191*, 71–86.

Quartel, S., Kroon, A., & Ruessink, B. G. (2008). Seasonal accretion and erosion patterns of a microtidal sandy beach. *Marine Geology*, *250*(1-2), 19–33. https://doi.org/10.1016/j.margeo.2007.11.003

Radermacher, M., de Schipper, M. A., Swinkels, C., MacMahan, J. H., & Reniers, A. J. H. M. (2017). Journal of Geophysical Research : Oceans Tidal flow separation at protruding beach nourishments. *Journal of Geophysical Research: Oceans*, *122*, 63–79. https://doi.org/10.1002/2016JC011942

Ranasinghe, R. (2020). On the need for a new generation of coastal change models for the 21st century. *Scientific Reports*, *10*, 1–6. https://doi.org/10.1038/s41598-020-58376-x

Ranasinghe, R., Callaghan, D., & Stive, M. J. F. (2012). Estimating coastal recession due to sea level rise: Beyond the Bruun rule. *Climatic Change*, *110*(3-4), 561–574. https://doi.org/10.1007/s10584-011-0107-8

Ranasinghe, R., Swinkels, C., Luijendijk, A., Roelvink, D., Bosboom, J., Stive, M., & Walstra, D. J. (2011). Morphodynamic upscaling with the morfac approach: Dependencies and sensitivities. *Coastal Engineering*, *58*, 806–811. https://doi.org/10.1016/j.coastaleng.2011.03.010

Reimann, L., Vafeidis, A. T., & Honsel, L. E. (2023). Population development as a driver of coastal risk: Current trends and future pathways. *Cambridge Prisms: Coastal Futures*, *1*, 1–12. https://doi.org/10.1017/cft.2023.3

Reniers, A. J., Roelvink, J. A., & Thornton, E. B. (2004). Morphodynamic modeling of an embayed beach under wave group forcing. *Journal of Geophysical Research: Oceans*, *109*. https://doi.org/10.1029/2002jc001586

Rijkswaterstaat. (2013, July 22). *Kenmerkende waarden, getijgebied 2011.0*. RWS Centrale Informatievoorziening. Delft, The Netherlands.

Rijkswaterstaat. (2018, December 1). *Kustlijnkaartenboek 2019*.

Rijkswaterstaat. (2020a). *Annual cross-shore transect bathymetry measurements along the dutch coast since 1965*. Retrieved February 9, 2021, from https://opendap.deltares.nl/thredds/catalog/opendap/rijkswaterstaat/jarkus/profiles/catalog.html

Rijkswaterstaat. (2020b, December 1). *Kustlijnkaartenboek 2021*.

Rijkswaterstaat. (2020c). *Nourishments along the dutch coast since 1952*. Retrieved April 12, 2021, from https://opendap.deltares.nl/thredds/catalog/opendap/rijkswaterstaat/suppleties/catalog.html

Roelvink, J. A. (1993). Dissipation in random wave groups incident on a beach. *Coastal Engineering*, *19*, 127–150. https://doi.org/10.1016/0378-3839(93)90021-Y

Roelvink, J. A., Huisman, B., Elghandour, A., Ghonim, M., & Reyns, J. (2020). Efficient Modeling of Complex Sandy Coastal Evolution at Monthly to Century Time Scales. *Frontiers in Marine Science*, *7*(July), 1–20. https://doi.org/10.3389/fmars.2020.00535

Roelvink, J. A., Kroon, A., Attema, Y., de Bakker, A., & Huisman, B. (2024). Simulating beach and dune evolution due to longshore transport, aeolian transport and dune erosion. *Coastal Engineering Proceedings*.

Roelvink, J. A., Reniers, A., van Dongeren, A., van Thiel de Vries, J., McCall, R., & Lescinski, J. (2009). Modelling storm impacts on beaches, dunes and barrier islands. *Coastal Engineering*, *56*, 1133–1152. https://doi.org/10.1016/j.coastaleng.2009.08.006

Roest, B., De Schipper, M. A., De Vries, S., & De Zeeuw, R. (2017). *Combined morphology surveys delfland [data set]*. https://doi.org/10.4121/uuid:d469c50b-edb6-4aa7-811d-f19b389ed344

Roest, B., de Vries, S., de Schipper, M., & Aarninkhof, S. (2021). Observed changes of a mega feeder nourishment in a coastal cell: Five years of sand engine morphodynamics. *Journal of Marine Science and Engineering*, *9*, 1–24. https://doi.org/10.3390/jmse9010037

Ruessink, B. G. (2005). Predictive uncertainty of a nearshore bed evolution model. *Continental Shelf Research*, *25*(9), 1053–1069. https://doi.org/10.1016/j.csr.2004.12.007

Ruessink, B. G., & Kuriyama, Y. (2008). Numerical predictability experiments of cross-shore sandbar migration. *Geophysical Research Letters*, *35*(1), 1–5. https://doi.org/10.1029/2007GL032530

Ruggiero, P., Buijsman, M., Kaminsky, G. M., & Gelfenbaum, G. (2010). Modeling the effects of wave climate and sediment supply variability on large-scale shoreline change. *Marine Geology*, *273*(1-4), 127–140. https://doi.org/10.1016/j.margeo.2010.02.008

Sadegh, M., & Vrugt, J. A. (2013). Bridging the gap between glue and formal statistical approaches: Approximate bayesian computation. *Hydrology and Earth System Sciences*, *17*, 4831–4850. https://doi.org/10.5194/hess-17-4831-2013

Saltelli, A., Ratto, M., Andres, T., Campolongo, F., Cariboni, J., Gatelli, D., Saisana, M., & Tarantola, S. (2008). *Global sensitivity analysis: The primer*. Chichester, UK: John Wiley & Sons.

Sánchez-Arcilla, A., Jiménez, J. A., & Marchand, M. (2011). Managing coastal evolution in a more sustainable manner. The Conscience approach. *Ocean & Coastal Management*, *54*(12), 951–955. https://doi.org/10.1016/j.ocecoaman.2011.05.002

Schoonees, J. S., & Theron, A. K. (1996). Improvement of the most accurate longshore transport formula. *Coastal Engineering 1996*, 3652–3665.

Schwarz, G. (1978). Estimating the Dimension of a Model. *The Annals of Statistics*, *6*(2), 461–464. https://doi.org/10.1214/aos/1176344136

Silva, F. G., Wijnberg, K. M., de Groot, A. V., & Hulscher, S. J. M. H. (2017). On the importance of tidal inlet processes for coastal dune development. *Coastal Dynamics Proceedings*, *104*(252), 106–110. https://doi.org/10.16192/j.cnki.1003-2053.2015.02.013

Simmons, J. A., Harley, M. D., Marshall, L. A., Turner, I. L., Splinter, K. D., & Cox, R. J. (2017). Calibrating and assessing uncertainty in coastal numerical models. *Coastal Engineering*, *125*(October), 28–41. https://doi.org/10.1016/j.coastaleng.2017.04.005

Smith, A., Houser, C., Lehner, J., George, E., & Lunardi, B. (2020). Crowd-sourced identification of the beach-dune interface. *Geomorphology*, *367*, 107321. https://doi.org/10.1016/j.geomorph.2020.107321

Smyth, T. A., & Hesp, P. A. (2015). Aeolian dynamics of beach scraped ridge and dyke structures. *Coastal Engineering*, *99*, 38–45. https://doi.org/https://doi.org/10.1016/j.coastaleng.2015.02.011

Sobol', I. M. (1967). On the distribution of points in a cube and the approximate evaluation of integrals. *USSR Computational Mathematics and Mathematical Physics*, *7*(4), 86–112. https://doi.org/10.1016/0041-5553(67)90144-9

Southgate, H. N. (1995). The effects of wave chronology on medium and long term coastal morphology. *Coastal Engineering*, *26*(95), 251–270.

Spear, R. C., & Hornberger, G. M. (1980). Eutrophication in peel inlet-ii. identification of critical uncertainties via generalized sensitivity analysis. *Water Research*. https://doi.org/10.1016/0043-1354(80)90040-8

Stive, M. J., De Schipper, M. A., Luijendijk, A. P., Aarninkhof, S. G., Van Gelder-Maas, C., Van Thiel De Vries, J. S., De Vries, S., Henriquez, M., Marx, S., & Ranasinghe, R. (2013). A new alternative to saving our beaches from sea-level rise: The sand engine. *Journal of Coastal Research*, *29*(5), 1001–1008. https://doi.org/10.2112/JCOASTRES-D-13-00070.1

Strauss, D., Silva, G. V. D., Silva, A. P. D., Murray, T., Faivre, G., & Wharton, C. (2020). Process-based modelling of a nearshore nourishment. *Journal of Coastal Research*, *95*, 1297–1302. https://doi.org/10.2112/SI95-250.1

Sutherland, J., Peet, A. H., & Soulsby, R. L. (2004). Evaluating the performance of morphological models. *Coastal Engineering*, *51*, 917–939. https://doi.org/10.1016/j.coastaleng.2004.07.015

Sutton-Grier, A. E., Wowk, K., Bamford, H., Sutton-Grier, A. E., Gov, (H., & Bamford,) (2015). Future of our coasts: The potential for natural and hybrid infrastructure to enhance the resilience of our coastal communities, economies and ecosystems. *Environmental Science & Policy*, *51*, 137–148. https://doi.org/10.1016/j.envsci.2015.04.006

Technische Adviescommissie voor de Waterkeringen. (1984). *Leidraad voor de beoordeling van duinen als waterkering*. Staatsuitgeverij. The Hague, The Netherlands.

Thieler, E. R., Pilkey, O. H., Young, R. S., Bush, D. M., & Chai, F. (2000). The use of mathematical models to predict beach behavior for u.s. coastal engineering: A critical review. *Journal of Coastal Research*, *16*, 48–70.

Thornton, E. B., MacMahan, J., & Sallenger, A. H. (2007). Rip currents, mega-cusps, and eroding dunes. *Marine Geology*, *240*, 151–167. https://doi.org/10.1016/j.margeo.2007.02.018

Ton, A. M., Vuik, V., & Aarninkhof, S. G. (2023). Longshore sediment transport by large-scale lake circulations at low-energy, non-tidal beaches: A field and model study. *Coastal Engineering*, *180*, 104268. https://doi.org/10.1016/j.coastaleng.2022.104268

Tonnon, P. K., Huisman, B. J. A., Stam, G. N., & Van Rijn, L. C. (2018). Numerical modelling of erosion rates , life span and maintenance volumes of mega nourishments. *Coastal Engineering*, *131*(March 2017), 51–69. https://doi.org/10.1016/j.coastaleng.2017.10.001

Tuffin, B. (1996). On the use of low discrepancy sequences in monte carlo methods. *Monte Carlo Methods and Appl.*, *2*(4), 295–320. https://doi.org/doi:10.1515/mcma.1996.2.4.295

van der Spek, B. J., Bijl, E., van de Sande, B., Poortman, S., Heijboer, D., & Bliek, B. (2020). Sandbar breakwater: An innovative nature-based port solution. *Water (Switzerland)*, *12*. https://doi.org/10.3390/w12051446

van der Wal, D. (2004). Beach-dune interactions in nourishment areas along the dutch coast. *Journal of Coastal Research*, *20*(1), 317–325.

van der Wegen, M., & Jaffe, B. E. (2013). Towards a probabilistic assessment of process-based, morphodynamic models. *Coastal Engineering*, *75*, 52–63. https://doi.org/10.1016/j.coastaleng.2013.01.009

van der Werf, J. J., de Vet, P. L., Boersema, M. P., Bouma, T. J., Nolte, A. J., Schrijvershof, R. A., Soissons, L. M., Stronkhorst, J., van Zanten, E., & Ysebaert, T. (2019). An integral approach to design the roggenplaat intertidal shoal nourishment. *Ocean and Coastal Management*, *172*, 30–40. https://doi.org/10.1016/j.ocecoaman.2019.01.023

van Rijn, L. C., Walstra, D. J. R., Grasmeijer, B., Sutherland, J., Pan, S., & Sierra, J. P. (2003). The predictability of cross-shore bed evolution of sandy beaches at the time scale of storms and seasons using process-based profile models. *Coastal Engineering*, *47*(3), 295–327. https://doi.org/10.1016/S0378-3839(02)00120-5

van Alphen, J. (1987). *De morfologie en lithologie van de brandingszone tussen terheijde en egmond aan zee* (NZ-N-87.28). Rijkswaterstaat. Utrecht, The Netherlands.

van Gelder, P. H. A. J. M. (2000). *Statistical methods for the risk-based design of civil structures* (Doctoral dissertation). Delft University of Technology.

van Gent, M. R., van Thiel de Vries, J. S., Coeveld, E. M., de Vroeg, J. H., & van de Graaff, J. (2008). Large-scale dune erosion tests to study the influence of wave periods. *Coastal Engineering*, *55*, 1041–1051. https://doi.org/10.1016/j.coastaleng.2008.04.003

van Koningsveld, M. (2003). *Matching specialist knowledge with end user needs* (Doctoral dissertation). University of Twente, Enschede. Universal Press.

van Koningsveld, M., Davidson, M. A., & Huntley, D. A. (2005). Matching science with coastal management needs: The search for appropriate coastal state indicators. *Journal of Coastal Research*, *21*, 399–411. https://doi.org/10.2112/03-0076.1

van Maren, D. S., & Cronin, K. (2016). Uncertainty in complex three-dimensional sediment transport models: Equifinality in a model application of the ems estuary, the netherlands. *Ocean Dynamics*, *66*, 1665–1679. https://doi.org/10.1007/s10236-016-1000-9

van Puijenbroek, M. E., Limpens, J., de Groot, A. V., Riksen, M. J., Gleichman, M., Slim, P. A., van Dobben, H. F., & Berendse, F. (2017). Embryo dune development drivers: beach morphology, growing season precipitation, and storms. *Earth Surface Processes and Landforms*, *42*(11), 1733–1744. https://doi.org/10.1002/esp.4144

van Rijn, L. C. (1993). *Principles of sediment transport in rivers, estuaries and coastal seas*. Aqua Publications.

van Rijn, L. C. (1997). Sediment transport and budget along the dutch coastal zone. *Coastal Engineering*, *32*, 61–90.

van Vuren, B. G. (2005). *Stochastic modelling of river morphodynamics Stochastisch modelleren van riviermorfodynamica* (Doctoral dissertation). Delft University of Technology.

van Westen, B., Luijendijk, A. P., de Vries, S., Cohn, N., Leijnse, T. W. B., & de Schipper, M. A. (2024). Predicting marine and aeolian contributions to the sand engine's evolution using coupled modelling. *Coastal Engineering*. https://doi.org/10.1016/j.coastaleng.2023.104444

Verhagen, H. J. (1996). Analysis of beach nourishment schemes. *Journal of Coastal Research*, *12*, 179–185.

Villaret, C., Kopmann, R., Wyncoll, D., Riehme, J., Merkel, U., & Naumann, U. (2016). First-order uncertainty analysis using Algorithmic Differentiation of morphodynamic models. *Computers and Geosciences*, *90*, 144–151. https://doi.org/10.1016/j.cageo.2015.10.012

Vitousek, S., Barnard, P. L., Limber, P., Erikson, L., & Cole, B. (2017). A model integrating longshore and cross-shore processes for predicting long-term shoreline response to climate change. *Journal of Geophysical Research: Earth Surface*, *122*, 782–806. https://doi.org/10.1002/2016JF004065

Vitousek, S., Cagigal, L., Montaño, J., Rueda, A., Mendez, F., Coco, G., & Barnard, P. L. (2021). The application of ensemble wave forcing to quantify uncertainty of shoreline change predictions. *Journal of Geophysical Research: Earth Surface*, *126*. https://doi.org/10.1029/2019JF005506

Vitousek, S., Vos, K., Splinter, K. D., Erikson, L., & Barnard, P. L. (2023). A model integrating satellite-derived shoreline observations for predicting fine-scale shoreline response to waves and sea-level rise across large coastal regions. *Journal of Geophysical Research: Earth Surface*, *128*. https://doi.org/10.1029/2022JF006936

Vrijling, J. K., & Meijer, G. J. (1992). Probabilistic coastline position computations. *Coastal Engineering*, *17*, 1–23. https://doi.org/10.1016/0378-3839(92)90011-I

Vuik, V., Jonkman, S. N., Borsje, B. W., & Suzuki, T. (2016). Nature-based flood protection: The efficiency of vegetated foreshores for reducing wave loads on coastal dikes. *Coastal Engineering*, *116*, 42–56. https://doi.org/10.1016/j.coastaleng.2016.06.001

Walker, I. J., Davidson-Arnott, R. G. D., Bauer, B. O., Hesp, P. A., Delgado-Fernandez, I., Ollerhead, J., & Smyth, T. A. G. (2017). Scale-dependent perspectives on the geomorphology and evolution of beach-dune systems. *Earth-Science Reviews*, *171*, 220–253. https://doi.org/https://doi.org/10.1016/j.earscirev.2017.04.011

Walker, W. E., Harremoës, P., Rotmans, J., van der Sluijs, J. P., van Asselt, M. B. A., Janssen, P., & von Krauss, M. P. K. (2003). Defining uncertainty: A conceptual basis for uncertainty management in model-based decision support. *Integrated Assessment*, *4*, 5–17. https://doi.org/10.1076/iaij.4.1.5.16466

Warner, J. C., Armstrong, B., He, R., & Zambon, J. B. (2010). Development of a Coupled Ocean – Atmosphere – Wave – Sediment Transport (COAWST) Modeling System. *Ocean Modelling*, *35*, 230–244. https://doi.org/10.1016/j.ocemod.2010.07.010

Weathers, H., & Voulgaris, G. (2013). Evaluation of beach nourishment evolution models using data from two south carolina, usa beaches: Folly beach and hunting island. *Journal of Coastal Research*, *69*, 84–98. https://doi.org/10.2112/SI_69_7

Wijnberg, K. M. (2002). Environmental controls on decadal morphologic behaviour of the Holland coast. *Marine Geology*, *189*(3-4), 227–247. https://doi.org/10.1016/S0025-3227(02)00480-2

Wijnberg, K. M., Poppema, D., Mulder, J., van Bergen, J., Campmans, G., Galiforni-Silva, F., Hulscher, S., & Pourteimouri, P. (2021). Beach-dune modelling in support of building with nature for an integrated spatial design of urbanized sandy shores. *Research in Urbanism Series*, *7*, 241–259. https://doi.org/10.47982/rius.7.136

Wijnberg, K. M., & Terwindt, J. H. J. (1995). Extracting decadal morphological behaviour from high-resolution, long-term bathymetric surveys along the holland coast using eigenfunction analysis. *Marine Geology*, *126*, 301–330.

Wilson, G. (2023). Uncertainty in nearshore sand bar migration. *Journal of Geophysical Research: Earth Surface*, *128*. https://doi.org/10.1029/2022JF006928

WL|Delft Hydraulics. (1994). *Unibest, a software suite for the simulation of sediment transport processes and related morphodynamics of beach profiles and coastline evolution, programme manual* (tech. rep.). WL|Delft Hydraulics.

Yates, M. L., Guza, R. T., & O'Reilly, W. C. (2009). Equilibrium shoreline response: Observations and modeling. *Journal of Geophysical Research: Oceans*, *114*. https://doi.org/10.1029/2009JC005359

A

Elementary Effects

The Elementary Effects method can analyze the sensitivity of the model outcome to several parameters. This method is used to further reduce the 16 Delft3D parameters that remain after expert judgement and further reduce the parameter set to the five most influential parameters to be used in the GLUE analysis.

A.1. Methods

The elementary effects (EE) method is a one-at-a-time sensitivity analysis method (Saltelli *et al.*, 2008). It is an effective screening method for models with many parameters, requiring a relatively low number of computations. The concept of elementary effects was first proposed by Morris (1991) as a tool to find the input parameters of a model whose effects could be considered (a) negligible, (b) linear and additive, or (c) non-linear or involved in interactions with other parameters. An elementary effect represents the difference between the model evaluations of two simulations, which differ in only one input parameter. The elementary effect EE_i of input parameter X_i is given by:

$$EE_i = \frac{Y(X_1, ..., X_i + \Delta, ..., X_k) - Y(X_1, ..., X_i, ..., X_k)}{\Delta}, \tag{A.1}$$

where vector $\mathbf{X} = (X_1, ..., X_k)$ represents the input parameters, k represents the number of varied parameters, and Δ is a normalized increment value by which one of the input parameters is changed (i.e. Δ is a value in the interval [0, 1] that is transformed to the ranges of the parameter: 0 and 1 correspond to the lower and upper limits, respectively). $Y(\mathbf{X})$ is the model evaluated at point $\mathbf{X}$, that is, the output variable considered.

The parameter space is discretized into a p-level grid (every parameter can vary across p levels). Starting from a random base vector $\mathbf{X}$ of length k (containing one value for each parameter), every input parameter is changed by Δ one after another, with the condition that every parameter is changed exactly once and the order is randomized (Δ must be chosen so that it fits the p-level grid). This results in a random trajectory through the k-dimensional parameter space.

A

Since every input parameter is changed exactly once during the trajectory, one EE per parameter can be computed. This process is repeated r times ($r = O(10)$), resulting in r trajectories and r EE's per parameter (Fig. A.1). The model sensitivity to a certain input parameter can then be examined by computing the mean, μ, and standard deviation, σ, of the EE of that parameter. Thus, μ_i represents the overall influence of parameter X_i on model output Y, while σ_i indicates the ensemble of the effects of the parameter. A high value of σ_i would imply that the EE's of X_i vary strongly among the trajectories, i.e., the model's response to the parameter is non-linear and/or the parameter interacts with other input parameters (see also Fig. A.2). Therefore, the method provides information on the input parameters' influence, dependence, and non-linearity.

When the model is non-monotonic, the EEs for a specific parameter can be positive and negative, resulting in a low average value. Therefore, an additional value, μ^*, is computed as the mean of the absolute values of a parameter's EE (Campolongo *et al.*, 2007). Furthermore, μ^* provides a good proxy of the total variance-based sensitivity index, making it a suitable measure for a parameter's absolute influence. The corresponding loss of information on the EE's sign can be prevented by simply computing all three sensitivity measures (μ, μ^*, and σ).

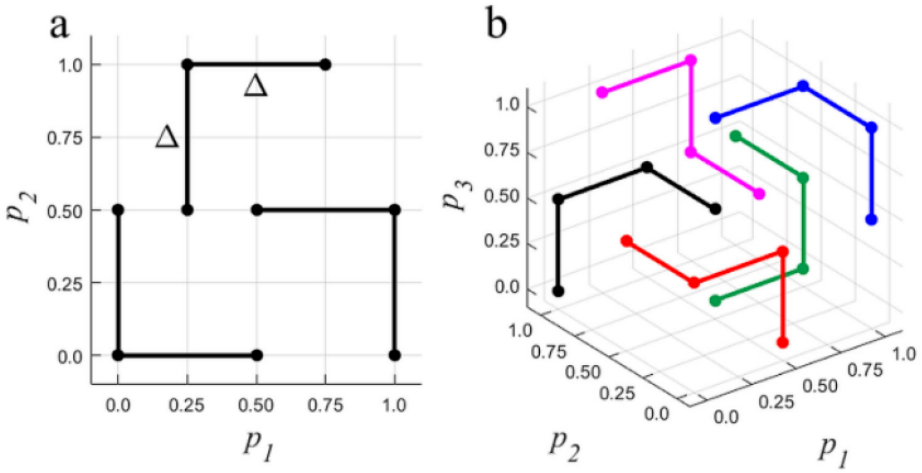

Figure A.1.: Example of r EE-trajectories through the k-dimensional parameter space of a model for a) k = 2 and r = 3 and b) k = 3 and r = 5. Source: Likhachev (2019)

The chosen parameters and their respective ranges and levels are summarized in Table A.1. p and Δ are directly related, as Δ needs to fit the applied levels. A convenient way to ensure that the sampling process guarantees equal probability for each level is to assign an even value to p combined with $\Delta = p/(2(p-1))$ (Saltelli *et al.*, 2008). The choice of r depends on several factors and usually lies between 10 and 50 (Campolongo *et al.*, 2007). On the one hand, a larger r is de-

sirable as it increases the sampling resolution of the parameter space. On the other hand, each additional trajectory increases the number of simulations by $k+1$ (the total number of simulations is given by $r(k+1)$). Moreover, the choice of r is strongly related to p. A larger value of p divides the parameter space into more levels, inherently increasing the resolution. However, the effective sampling resolution only improves if the increase in p is combined with a higher value of r, as a small number of trajectories would leave a large part of the parameter space unexplored. In short, the choice of r and p depends on the desired sampling resolution and the available computational budget. Previous studies have indicated that values of p = 4 and r = 10 can already lead to reliable results (Campolongo *et al.*, 2007; Saltelli *et al.*, 2008, and references therein). This study examines the sensitivity to k = 16 parameters; to achieve a sufficient sampling resolution, r is chosen well above this threshold, at r = 20 and p = 4. This gives a step value of $\Delta = p/(2(p-1)) = 2/3$. Whenever a parameter is increased or decreased by Δ, it effectively skips one level. The 20 trajectories consist of k + 1 = 17 simulations each, resulting in 340 simulations. The applied parameter settings are summarized in Table A.2.

The python package SALib (Iwanaga *et al.*, 2022) is used to draw 20 random sampling points in the 16-dimensional unit hypercube, their coordinates all equal to one of the four levels ([0, 0.33, 0.67, 1]). These form the base vectors of the 20 trajectories. The components of each base vector are then one-by-one in- / decreased by Δ, in random order, resulting in 16 additional vectors per trajectory. Any two consecutive vectors differ in exactly one component. Once all the trajectories are created, the vector components (representing coordinates in the 16-dimensional unit hypercube) are transformed to the respective parameter ranges to give the parameter sets for the simulations (Table A.1).

The elementary effects are calculated for bed level, shoreline position, and volume changes. The calculation of the EE's for the shoreline position and bed level change are computed as the average difference in bed level or shoreline position.

Once the EE's have been computed, the sensitivity measures can be derived, and the parameters can be compared. The examined parameters are plotted in $\mu^* - \sigma$ space, showing the parameters' influence on the x-axis and non-linearity / interdependence on the y-axis (Fig. A.2). All parameters above the line $\mu^* = \sigma$ can be considered to be involved in significant interactions or non-linearities, while the ones below the line are not (Khare *et al.*, 2019).

A.2. Results

The EEs are computed over four control areas for the cumulative volume changes (Fig. 4.5). f_{sus} is the most influential parameter, as it has the highest influence (μ^*) for all four areas. It is followed by d_{50} and the fac_{DSS}, which are close to each other in all four areas. The suspended sediment transport significantly influences the predicted volume changes as all these parameters are included in the sediment concentration term. After this 'top three,' a second group of para-

A

Cat.	Parameter	Symbol	Def.	Ref.	Range			
H	Bed roughness (Chézy) $[m^{1/2}/s]$	C	65	65	50	60	70	80
	Horizontal eddy viscosity $[m^2/s]$	ν_h^{back}	0	1	0.1	0.73	1.37	2
	Horizontal eddy diffusivity $[m^2/s]$	D_h^{back}	0	1	0.1	0.73	1.37	2
W	Breaker index	γ	0.55	0.73	0.55	0.63	0.72	0.8
	Breaker index limiter	γ_{max}	0.8	0.55	0.63	0.72	0.8	
	Wave dissipation coefficient	α_{rol}	1	1	0.1	0.73	1.37	2
	Mean roller slope	β_{rol}	0.1	0.1	0.01	0.07	0.137	0.2
S	Suspended transport scaling (current)	f_{sus}	1	0.5	0.1	0.4	0.7	1
	Suspended transport scaling (waves)	$f_{sus,w}$	1	0.2	0.1	0.4	0.7	1
	Bed-load transport scaling (current)	f_{bed}	1	0.5	0.1	0.4	0.7	1
	Bed-load transport scaling (waves)	$f_{bed,w}$	1	0.2	0.1	0.4	0.7	1
	Median grain diameter $[\mu m]$	d_{50}	300	200	250	300	350	
	Suspended grain size factor	Fac_{DSS}	1	1	0.6	0.73	0.87	1
M	Streamwise bed slope coefficient	α_{bs}	1	10	1	9	17	25
	Transverse bed slope coefficient	α_{bn}	1.5	15	1	9	17	25
	Dry cell erosion	θ_{sd}	0	1	0	0.33	0.67	1

Table A.1.: Overview of the initial parameter shortlist, showing the 16 selected parameters, default values (if available), applied values in the reference simulation (Luijendijk *et al.*, 2019), and the ranges for the SA, divided into four levels.

Parameter	Symbol	Value
Number of parameters	k	16
Number of trajectories	r	20
Number of levels	p	4
Normalised step value	Δ	2/3
Normalised levels		[0, 0.33, 0.67, 1]
Total amount of simulations	$r(k+1)$	340

Table A.2.: Summary of parameter settings for the EE method.

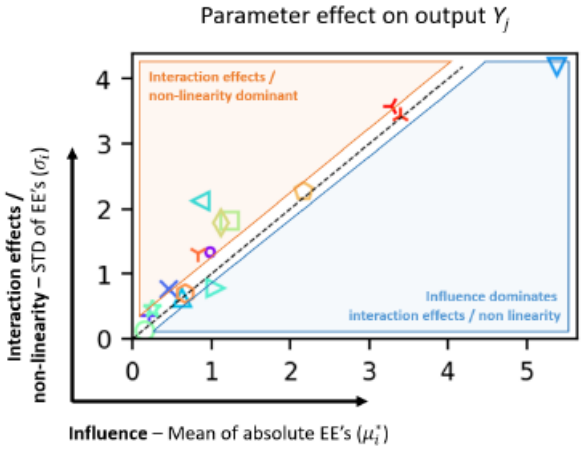

Figure A.2.: Example plot of a parameter comparison by the EE method, plotting the mean (μ^*) and standard deviation (σ) of the EE's for every input parameter, measured to output variable Y_j. The dashed line represents the $\mu^* = \sigma$ line.

.

meters shows similar degrees of influence across the four areas (see red circles in Figure 4.3). This group consistently includes C, $f_{sus,w}$, α_{rol}, β_{rol}, γ, γ_{max}, and θ_{sd}. Their relative influence shows variations among the four areas but is generally close. α_{rol}, γ, and θ_{sd} lead this group. In the South section, d_{50} and fac_{DSS} also belong in this second group. The remaining parameters are consistently at the low end of the μ^*-axis, implying low influence on volume changes. Except for f_{sus}, all parameters are relatively close to the $\mu^* = \sigma$ line. Specifically, no other parameter is consistently located far off the line. This suggests that interaction effects are not extreme, yet exist for most parameters. Note that the relatively low value of σ for f_{sus} does not mean that it does not interact with other parameters or that the model response to this parameter is linear. It still has the largest absolute σ of all parameters. Rather, its position below the dashed line suggests that the overall influence of the parameter overshadows the interaction/ non-linear effects. The simulations of one of the EE trajectories showed unrealistically strong erosion patterns for a particular combination of $f_{sus,w}$ and α_{rol}. This trajectory is treated as an outlier for the EE analysis (i.e., the results are based on 323 of the 340 simulations) because it results in unrealistically high σ values.

Also, for the coastal state indicator shoreline position, f_{sus} is the most influential parameter (Figure 4.4, upper panels). The d_{50} and Fac_{DSS} are less influential than compared to CSI volume changes. The 'second group' now clearly consists of seven parameters (red dashed circles): d_{50}, Fac_{DSS}, $f_{sus,w}$, α_{rol}, β_{rol}, γ, θ_{sd}. But in this case, C falls out of this group. The differences between the entire

shoreline and the spit area are limited. Only $f_{sus,w}$ is more influential for the entire shoreline, but the second group is clustered relatively close in both cases.

The results of the EE analysis for the bed levels are comparable to those of the shoreline. f_{sus} remains dominant over the other parameters, indicating that it is by far the most influential parameter for the applied model. After that, the order of the remaining seven parameters is similar to that of the shoreline. This group is a bit more spread out and, like the volume changes, is led by d_{50} and Fac_{Dss}.

Based on the results of the previous sections, a final ranking of the parameters is created. The parameters are ranked for each of the three output categories (Volume changes, shoreline position, and bed levels) based on their corresponding μ^* value. For each output category, the components are given equal weight (e.g., for the volume changes, the parameters are ranked by their average rank for the four control areas). Note that this is a simple ranking, meaning it does not represent the absolute difference in influence between parameters. Hence, some parameters are tied for the same rank. The ranking (Table A.3) shows the dominance of f_{sus}, which ranks first for each category. The parameters d_{50} and Fac_{DSS} rank second and third for the volume changes and bed levels but only tied sixth for the shoreline. Note, however, that for the shoreline, ranks two to seven have similar μ^* values and mainly differ in σ. γ, α_{rol}, β_{rol}, θ_{sd} and $f_{sus,w}$ all consistently feature in the top seven as well. In fact, the top eight of each category consist of the same eight parameters (except for C, which takes the place of $f_{sus,w}$ for the volume changes). These eight parameters form a more influential group, whereas the remaining eight parameters hardly feature in the top ten for any output category.

The final selection for the GLUE method consists of the following five parameters: f_{sus}, d_{50}, γ, α_{rol}, and θ_{sd} (Table 4.1). The selection of each parameter is briefly discussed below.

- Suspended sediment transport scaling factor, f_{sus}

  This parameter is the most obvious choice as it is by far the most influential parameter on every CSI, according to the EE results.

- Median grain diameter, d_{50}

  The d_{50} is generally the second most influential parameter, although its influentiallity is closer to the rest of the parameters than to f_{sus}.

- Wave breaker index, γ

  According to the EE results, the breaker index γ is the most influential wave parameter (slightly ahead of α_{rol}, based on μ^*). It effectively determines at which water depth waves start to break, directly influencing the amount of energy transferred by breaking waves, which was also found to be an essential aspect of the SE model by Luijendijk *et al.* (2017a).

- Wave energy dissipation coefficient, α_{rol}

  α_{rol} is another influential wave parameter. It also shows interesting results in the performance analysis, as the best value appears to be its upper limit

(2). This could indicate that the full range of suitable values has not yet been applied for this parameter and that it might be even more influential. Finally, it has relatively low σ values compared to other parameters, making it less likely to interact with other selected parameters.

- Dry cell erosion factor, θ_{sd}

  Luijendijk *et al.* (2017a) identified dry cell erosion as an important feature in the SE model. θ_{sd} is less influential than some of the remaining parameters (i.e., Fac_{DSS}). However, the above four parameters include two sediment and wave parameters. θ_{sd} adds a morphology parameter to this group (while the remaining three options would add another wave or sediment parameter). Although θ_{sd} does show high σ values, because of its implementation (affecting the bed update near the wet-dry interface) in the model, it is not likely to interact strongly with other parameters.

Next, a short explanation of why the remaining three parameters of the influential group have not been selected.

- Wave-affected sediment transport scaling, $f_{sus,w}$

  This parameter is highly influential for the shoreline position (ranks second) but less so for the other outputs (e.g., ninth for the volume changes). Additionally, the performance analysis suggests that the lowest value is by far the best (30 of the 35 best-scoring simulations), making it easier to find a fixed value for the parameter. One might argue that this parameter should be included since the waves form the dominant forcing mechanism. However, the main wave-affected sediment transport (caused by the wave-induced alongshore current) falls under the suspended transport, which is scaled by f_{sus} not $f_{sus,w}$.

- Mean roller slope, β_{rol}

  β_{rol} ranks lowest in absolute influence of the three wave parameters considered. Only for the volume changes in the South section it is more influential than γ and α_{rol}. Furthermore, the implementation of α_{rol} and β_{rol} as scaling coefficient of two dissipation components in the roller energy balance suggests that they can function as reciprocals of each other. Hence, adding β_{rol} instead of θ_{sd} would significantly increase the chance of strong interaction effects.

- Factor for suspended sediment size, Fac_{DSS}

  Overall, Fac_{DSS} is the third or fourth most influential parameter. However, its direct connection to d_{50} suggests interaction effects between the two will be strong (similar to α_{rol} and β_{rol}). Based on these observations and expert consultation, the assumption is made that part of the uncertainty in Fac_{DSS} can be captured by varying d_{50}.

The range has been adjusted for the GLUE analysis for some of the selected parameters. In case higher or lower values of a parameter show a particularly high or low skill, ranges are shifted, extended or narrowed (Table 4.1).

A

Rank	Volume changes	Shoreline position	Bed levels
1	f_{sus}	f_{sus}	f_{sus}
2	d_{50}	$f_{sus,w}$	d_{50}
3	Fac_{DSS}	α_{rol},γ,θ_{sd}	Fac_{DSS}
4	γ	-	θ_{sd}
5	α_{rol}	-	$f_{sus,w}$
6	β_{rol}	d_{50}, Fac_{DSS}	α_{rol}, γ
7	C, θ_{sd}	-	-
8	-	β_{rol}	β_{rol}
9	$f_{sus,w}$	D_h	C
10	γ_{max}	$f_{bed,w}$	D_h

Table A.3.: Top 10 influential parameters, ranked by the μ^* values obtained from the EE method. The ranking is given for each CSI (volume changes, shoreline position, and bed levels).

Acknowledgements

I have completed a journey that was harder on me than I expected. There were times when I regretted leaving the familiar offices of Svašek Hydraulics. Yet, I am happy with the person I have become, both professionally and personally, thanks to the challenges and successes of this journey. There are so many people to be thankful to.

First, this journey would not have begun without Bram Bliek, who helped convince the right people that this research would be worth their time and resources. I want to express my gratitude towards Stefan, Matthieu, and Kees den Heijer for their contribution in writing the proposal for the research project that was funded by TKI, Hoogheemraadschap Hollands Noorderkwartier, Rijkswaterstaat, Svašek Hydraulics, Van Oord, and Boskalis. I am grateful to all these entities for their support.

Matthieu, you have taught me so many things, I could not have wished for a better supervisor. Your critical questions concerning results, structured thoughts on outlines of the papers we were writing, and never-ending patience with improving paragraphs and sentences have helped me greatly. I appreciate that you were always concerned about my well-being before my research progress. I enjoyed working with you very much, and I hope we will continue to work together while supervising students and operating on the interface of research and engineering. Stefan, I am grateful to you for making this research happen, for all the times you have challenged me to see the implications of my research from a broader perspective, and for your never-ending optimism and pragmatism. Without you, this research probably wouldn't have started but definitely would not have ended yet. Pieter, thank you for sharing your extended knowledge of probabilistic methods.

My dear office roomies Anne, Matthijs, and Christa: we have shared many serious, scientific, crazy, funny, sad, happy, and exhausted moments. I am glad that you were on this journey with me for the most part. Florida was the best conference I have been to, and that was because you were part of it.

My other fellow PhDs Ana, Anna, Bas, Bart, Gijs, Jakob, Jill, Ligaya, Marlies, Mario, Max, Paul, Silke, Stuart, Su, Tosca, Romy, and Roy, and postdocs and staff Caroline, Jose, Natasha, Sander and Vincent, thank you for sharing part of this journey with me. Arjen, thank you for working together and for supervising Jakob when I could not. Sierd, I have enjoyed having you as a colleague. I love to talk about van life, sailing, or biking with you, and your spicy opinions always provide food for thought, whether over lunch or beers.

MSc. Students Linde, Inge, Vassia, Maurits, Tom, Jakob, and Petya, thank you for your work. I enjoyed supervising you, and I hope you have learned as much

from me as I have from you. Jakob, thank you in particular for your great contribution to chapter 4 of this dissertation.

My dear Svašek colleagues, you are the best! You have always made working at Svašek feel like home. You made me appreciate the dynamics of a small team compared to the scientific machine of the university. Bas v L. thank you for the freedom and trust you gave me these last years, without them I could not have finished this project. Floris, thanks for the (sarcastic) PhD pep-talks and for sharing our love for (biking in) Spain. Sanne, thank you for all the talks we have had at or around tea island. Barbara, Bas L., Bernard, Harmen, Lennard, Marloes, Phillip, Sam, Tom, Yannick, and Ype, thank you for being such kind and warm colleagues.

I'm so happy to have many loving, intelligent, and interested friends who have always made me feel welcome to discuss my research, who were there to go for a walk or a drink when I felt like I would never finish this project, but most of all, who were there for fun and distraction. I want to thank all of you: Anne, Carien, Carina, Claartje, Eva, Fieke, Janneke, Koosje, Leonie, Leta, Manon, Meike, Regien, Sanne, Saskia, Stefanie, and Suze Ann. Fieke and Janneke, I want to thank you in particular, for wanting to sit by my side during my defense as my paranimphs. I hope that finishing this chapter of my life means that I have more time to do some crazy stuff with all of you because sometimes I feel like I have grown to be a bit too serious.

My dear family, thank you for being there for me and for having such great confidence in me. Our quality time together has suffered under the pressure of my busy schedule, but I appreciate the space you gave me. Mama, thank you for raising me to be strong and perseverant. I really needed those virtues to be able to finish this project. Ellen, thank you for providing me with a workspace in Spain. This sunny office and my office mate, cat Minous, made the final sprint of thesis writing bearable. Zaza, thank you for the cover design.

Matthijs, thank you for traveling along this road with me and for the life we have built over the past 8 years. It has not been easy, but we made it this far because we were a good team. Thank you for listening to my presentations and for helping me think even more critically. Thank you for being in my life. You are my best friend, and I hope we have so much more time for adventures now that this chapter is closed!

About the Author

Anna Kroon was born and raised in Utrecht, where she attended the Bonifatiuscollege, and developed a strong liking for mathematics and physics. Subsequently, she pursued her Bachelor's degree in Civil Engineering at Delft University of Technology, marking the start of her education in engineering.

Driven by a passion for the dynamics of water and coastal environments, Anna continued her academic journey at Delft University of Technology, where she achieved her Master's degree in Hydraulic Engineering with honors (cum laude). Her specialization in coastal engineering and environmental fluid mechanics laid the groundwork for her expertise in addressing complex challenges related to water systems. She finished her Master's degree with a thesis on the "Implementation of a Wetting and Drying Algorithm in a Finite Element Model".

Post-graduation, Anna began her professional journey at Svašek Hydraulics in Rotterdam, where she actively contributed to the design of the Hondsbossche Dunes nourishment project. During this period, the challenges she faced professionally sparked the idea for further research for her doctoral degree.

Anna worked with her academic mentors and supervisors to develop a detailed research proposal. After receiving funding for the proposal, she started her research in 2017 while continuing her professional engagement at Svašek Hydraulics. This dual commitment to academia and industry reflects Anna's dedication to bridging the gap between theoretical knowledge and practical hydraulic engineering applications.

Anna lives in Den Haag with her partner. She enjoys spending her leisure time outdoors, whether on the beach, in the water, or in the mountains, where she loves to go sailing, kite surfing, hiking, biking, or traveling in her van.

List of Publications

Peer-reviewed journal papers

2. **Kroon, A.**, de Schipper, M.A., de Vries, S. and Aarninkhof, S.G.J., (2022) *Subaqueous and Subaerial Beach Changes after Implementation of a Mega Nourishment in Front of a Sea Dike*, Journal of Marine Science and Engineering **10**, 8 (1152).

1. **Kroon, A.**, de Schipper, M.A., van Gelder, P.H.A.J.M. and Aarninkhof, S.G.J., (2020) *Ranking uncertainty: Wave climate variability versus model uncertainty in probabilistic assessment of coastline change*, Coastal Engineering **158**, 6 (103673).

Conference papers

4. **Kroon, A.**, de Schipper, M.A., van Gelder, P.H.A.J.M. and Aarninkhof, S.G.J., (2019) *Quantification of model uncertainty in lifetime predictions of nourishments*, Coastal Sediments 2019: Proceedings of the 9th International Conference, (338–346).

3. **Kroon, A.**, de Schipper, M.A., and den Heijer, C., van Gelder, P.H.A.J.M. and Aarninkhof, S.G.J., (2017) *Uncertainty assessment in coastal morphology prediction with a bayesian network*, Proceedings of Coastal Dynamics 2017: Helsingør, Denmark **254**, (1909–1920).

2. **Kroon, A.**, van Leeuwen, B., Walstra, D.J. and Loman, G., (2016), *Dealing with uncertainties in long-term predictions of a coastal nourishment*, Coastal Management: Changing Coast, Changing Climate, Changing Minds - Proceedings of the International Conference, (9-18).

1. **Kroon, A.** and Loman, G., (2015), *Application of FINEL2D model in hydro-morphological support of design & build of "Maasvlakte 2"*, E-proceedings of the 36th IAHR World Congress, (2205-2216).

Conference abstracts, presentations and posters

10. **Kroon, A.**, Spaans, L., van Leeuwen, B., Attema, Y. and van der Giessen, K., (2024) *Morphological boundary conditions for increasing barrier island dynamics: the case of Schiermonnikoog*, NCK 2023.

9. **Kroon, A.**, Petrova, P., Attema, Y., Ruessink, B.G., Huisman, B.J.A. and de Schipper, M.A, (2023) *Parameter uncertainty in ShorelineS predictions of the Hondsbossche Dunes*, NCK 2023.

8. de Wit, F.P., **Kroon, A.** and Spaans, L., (2023) *Stochastic results from deterministic wave-resolving models*, NCK 2023.

7. Attema, Y., van Leeuwen, B. and **Kroon, A.**, (2023) *The importance of 2D effects on dune erosion during the 2022 winter storms at Maasvlakte II*, NCK 2023.

6. **Kroon, A.**, de Schipper, M.A., Pak, T., Spaans, L.S., de Vries, S. and S.G.J. Aarninkhof, (2021), *Beach width change and volume loss observations at a large nourished beach*, Coastal Dynamics 2021 Conference: 8th edition of the Coastal Dynamics Conference (Online Conference).

5. Christiaanse, J.C., **Kroon, A.**, Luijendijk, A.P. and de Schipper, M.A., (2021) *Quantifying parameter uncertainty in coastal area predictions*, Coastal Dynamics 2021 Conference: 8th edition of the Coastal Dynamics Conference (Online Conference).

4. **Kroon, A.**, de Schipper, M.A., van Gelder, P.H.A.J.M. and Aarninkhof, S.G.J., (2019) *Model uncertainty in predicting coastline response of building with nature designs*, NCK 2019.

3. **Kroon, A.**, de Schipper, M.A. and Aarninkhof, S.G.J., (2019) *Quantification of parameter and calibration uncertainty in morphological modelling*, International Conference on Coastal Engineering 2018.

2. **Kroon, A.**, de Schipper, M.A. and Aarninkhof, S.G.J., (2018) *The importance of uncertainty assessment in morphology predictions*, NCK 2018.

1. **Kroon, A.**, de Jongh, L., de Schipper, M.A. and Aarninkhof, S.G.J., (2017) *Initial evolution of a large-scale sandy intervention*, NCK 2017.

List of Acronyms

2DH	2 Dimensional Horizontal
BSS	Brier Skill Score
CDF	Cumulative Distribution Function
CI	Confidence Interval
CSI	Coastal State Indicator
EE	Elementary Effects
GLUE	Generalized Likelihood Uncertainty Estimation
HD	Hondsbossche Dunes
MSL	Mean Sea Level
NAP	Normaal Amsterdams Peil
OPS	Optimal Parameter Set
PDF	Probability Density Function
RMSE	Root Mean Squared Error
SE	Sand Engine